Translation of Intravascular Optical Ultrasound Imaging

Callum D. Little

A dissertation submitted in partial fulfillment

of the requirements for the degree of

Doctor of Philosophy

of

University College London.

Department of Medical Physics and Bioengineering

University College London

July 20, 2023

I, Callum D. Little, confirm that the work presented in this thesis is my own. Where information has been derived from other sources, I confirm that this has been indicated in the work.

Abstract

Advances in the field of intravascular imaging have provided clinicians with powerful tools to aid in the assessment and treatment of vascular pathology. Optical Ultrasound (OpUS) is an emerging modality with the potential to offer significant benefits over existing commercial technologies such as intravascular ultrasound (IVUS) or optical coherence tomography (OCT). With this paradigm ultrasound (US) is generated using pulsed or modulated light and received by a miniaturised fibre-optic hydrophone (FOH). The US generation is facilitated through the use of engineered optically-absorbing nanocomposite materials. To date pre-clinical benchtop studies of OpUS have shown significant promise however further study is needed to facilitate clinical translation.

The overall aim of this PhD was to develop a pathway to clinical translation of OpUS, enabled by the development of a catheter-based device capable of high resolution vascular tissue imaging during an in-vivo setting.

A forward-viewing OpUS imaging probe was developed using a 400 μm multimode optical fibre, dip-coated in a multi-walled carbon nanotube-PDMS composite, paired with a FOH comprising a 125 μm single mode fibre tipped with a Fabry-Perot cavity. With this high US pressures were generated (21.5 MPa at the transducer surface) and broad corresponding bandwidths were achieved (-6 dB of 39.8MHz). Using this probe, OpUS imaging was performed of an ex-vivo human coronary artery. The results demonstrated excellent correspondence, in the detection of calcification and lipid infiltration, with IVUS, OCT and histological analysis. A side-viewing OpUS imaging probe, employing a reflective 45 °angle at the distal fibre surface, was used to demonstrate rotational B-mode imaging of a vascular

structure for the first time. This provided high-resolution imaging (54 μm axial resolution) with deep depth penetration ($>$10.5 mm). Finally the clinical utility of this technology was demonstrated during an in-vivo endovascular procedure. An OpUS imaging probe, incorporated into an interventional device, allowed guidance of in-situ fenestration of an endograft during a complex abdominal aortic aneurysm repair.

Through this work the potential clinical utility of OpUS, to assess pathology and guide vascular intervention, has been demonstrated. These results pave the way for translation of this technology and a first in man study.

Impact Statement

This body of work outlines multiple advances that will benefit both biomedical researchers and clinicians. Chapter 2 presents a novel fabrication method for mesoscale phantoms which are important for the benchtop development and characterisation of emerging intravascular imaging technologies. Chapter 3 describes a new method for the fabrication of vascular phantoms that are complex, patient-specific and compatible with multiple imaging modalities. These are useful as training tools and for the validation of new surgical techniques. In Chapter 4 the development of Optical Ultrasound, a new intravascular imaging modality, is outlined. This will allow the development of devices capable of high resolution imaging, deep tissue penetration and compatibility with complementary imaging modalities such as photoacoustics (PA) or near infrared spectroscopy (NIRS). Chapter 5 details the clinical translation of OpUS and the development of an interventional device capable of assisting in complex endovascular surgery. The use of this technology has the potential to provide significant cost savings and may influence future decision making as to the optimum method for repairing complex vascular aneurysms.

Acknowledgements

Supervisors:

Prof. Adrien Desjardins & Prof. Roby Rakhit

I have been extremely fortunate to have both the support and guidance of these two inspirational academics. I will be eternally grateful for the faith that they showed in me to take on this project.

Medical Physics and Engineering, University College London:

Dr Richard Colchester, Dr Sacha Noimark, Dr Erwin Alles, Dr Sunish Mathews, Dr Jo Coote, Dr Sandy Mosse, Dr Radhika Poduval, Shaoyan Zhang & Prof Ioannis Papakonstantinou

WELLCOME/EPSRC centre for Interventional and Surgical Sciences:

Richard Caulfield, Eleanor Mackle, Elizabeth Carr, Dr Efthymios Maneas, Dr George Dwyer, Dr Daniil Nikitchev & Dr Malcolm Finlay

Royal Free Hospital, London

Ms Debra Chong, Dr Gavin Manamathan, Chris Loder, Prof Janice Tsui, Dr Jason Constantinou, Prof George Hamilton & Ms Tara Mastracci

I would like to acknowledge funding from both the WELLCOME/EPSRC Centre for Interventional and Surgical Sciences (WEISS) (203145Z/16/Z) and the University College London Biomedical Research Centre.

Contents

List of Figures

List of Tables

Chapter 1

General Introduction

1.1 Outline of the Thesis

This thesis details a path to clinical translation for a Optical Ultrasound (OpUS), a novel intravascular imaging modality. This journey starts at the benchtop and ends with the demonstration of the technology to guide complex endovascular therapeutics in an in-vivo model. The thesis is split into two sections; section 1 pertains to the development of imaging phantoms, whilst section 2 addresses the clinical translation of OpUS. Section 1 details the development and validation of novel high fidelity mesoscale (Chapter 2) and macroscale (Chapter 3) phantom models that enabled benchtop characterisation of intravascular imaging devices. The work detailed in this section represents a significant advancement in complexity and scale of imaging phantoms through novel advanced fabrication techniques and highly realistic tissue-mimicking materials. These phantoms are validated using contemporary imaging technology. Section 2 begins with the benchtop development of forward and side-viewing OpUS imaging probes (Chapter 4). For the first time OpUS is validated against existing intravascular imaging modalities on diseased coronary tissue. The fabricated side-viewing probe enables a first demonstration of OpUS rotational imaging. Additionally, the effects of frequency filtering for image optimisation are explored. Chapter 5 details a novel clinical application for OpUS technology in the endovascular treatment of complex abdominal aortic aneurysms. For this a custom-built dual imaging and therapeutic device is designed and charac-

terised on the benchtop. The purpose of this device is to achieve both detection of aortic side-branches beneath endovascular stent material and fenestration through this material to secure side-branch patency. The technology is then validated in two in-vivo experiments with subsequent stent analysis and tissue histology. Each chapter will have a separate background section, with literature review, in order to maintain clarity for the reader.

1.2 Intravascular Imaging

The term intravascular imaging refers to the process by which structural or compositional information regarding a vascular structure is obtained, usually through insertion of a catheter based device, to provide a reconstructed image that can be viewed and interpreted by the operator. Within the field of cardiovascular interventions two intravascular imaging modalities are widely used; Intravascular Ultrasound (IVUS) and Optical Coherence tomography (OCT). Over the last decade there have been tremendous advancements in intravascular imaging technology. There is an increasing role for these imaging tools in the characterization and severity assessment of atherosclerotic disease. Recently Optical Ultrasound (OpUS) has emerged as an alternative method for providing intravascular imaging. The path to clinical translation of this new imaging modality is the subject of this thesis. For the purposes of this thesis axial resolution is defined as the minimum distance that can be differentiated between two reflectors located parallel to the direction of imaging [3].

1.2.1 Intravascular Ultrasound (IVUS)

First developed in the late 1980's/early 1990's by Paul Yock [4], conventional IVUS devices employ piezoelectric transducers to electrically generate and receive ultrasound (US) in order to build up an image. Typical commercial IVUS imaging catheters operate with a transducer frequency of 40 MHz providing an axial resolution of 100-150 μm, lateral resolution of 200 μm and a tissue penetration of 4-8 mm [5]. Newer generation devices operating at a frequency of 60 Mhz are now available with resultant improved axial resolution in the order of 40 μm [6], at a cost of diminished tissue penetration. The diameter of these catheters is in the region

of 1.03-1.66 mm. IVUS has established roles in vessel sizing, detection of calcium and guidance of optimal stent expansion. A recently published meta-analysis of nine randomised controlled trials, including 4724 patients, demonstrated that IVUS guided percutaneous coronary intervention (PCI) using drug eluting stents (DES) reported a lower risk of major adverse cardiovascular outcomes (MACE) compared to angiography guidance alone (5.4% v 9.0%; RR: 0.61, 95% CI 0.49-0.74, $p<0.001$) at a mean follow-up of 16.7 months [7]. These findings were predominantly driven by lower rates of target vessel revascularisation (3.5% v 6.1%; RR: 0.58, 95% CI 0.42-0.8, p=0.001), stent thrombosis (0.5% vs 1.1%; RR: 0.45, 95% CI 0.23-0.87, p=0.02) and cardiac death (0.6% v 1.2%; RR: 0.49, 95% CI 0.26-0.92, p=0.03). IVUS may be particularly useful for assessing large calibre vessels such as the left main coronary artery [8] or aneurysmal vessels [9], however data from appropriately large randomised control trials in this area is lacking. In addition to intracoronary imaging IVUS has roles in the assessment of peripheral vascular disease (PVD) and its use is gaining popularity within the field of Aortic intervention for guiding endovascular Aortic repair (EVAR). For arterial PVD interventions routine IVUS has been shown to yield a 15 year primary patency rate of up to 75% [10]. In a large meta-analysis including 93,551 patients IVUS use compared to angiography guided intervention alone was associated with a lower risk of peri-procedural events (RR: 0.81, 95% CI 0.70-0.94,p=0.006) and vascular complications (RR: 0.81, 95% CI 0.68-0.96,p=0.013) [11]. For venous PVD interventions IVUS can identify residual thrombus burden post mechanical thrombectomy in patients with deep vein thrombosis (DVT) in up to 91% of cases that had been deemed successful based on venography [12]. IVUS use in EVAR can allow accurate sizing of stents to reduce the risk of a residual endoleak, where blood continues to leak into an aneurysm post intervention. It can also reduce the fluoroscopy time and intra-procedural contrast volume [13]. The aforementioned applications of IVUS technology employ a side-looking transducer. Additionally, forward-looking IVUS probes are in development, based on dual ring capacitive micromachined ultrasonic transducer (CMUT) arrays, and may provide future utility in the treatment of coro-

nary/PVD chronic total occlusions (CTO) [14][15].

With the electronic paradigm of generating IVUS there are significant challenges that restrict further enhancements in image quality. Firstly, with increasing miniaturization of the transducers necessary to decrease device size and improve deliverability, it can be difficult to achieve the high sensitivities and broad bandwidths desirable for high spatial resolutions whilst maintaining large penetration depths through vascular tissues. Secondly, there are significant complexities associated with the fabrication of miniaturized piezoelectric transducers resulting in relatively high manufacturing costs.

1.2.2 Optical Coherence Tomography (OCT)

Initially developed for characterisation of the retina by Fujimoto et al. [16] and subsequently translated to intravascular imaging, OCT images are obtained using near-infrared light (centred on 1310nm wavelength) emitted from a laser source and interrogated using interferometry. This offers superior axial (10 μm) and lateral (20 μm) resolutions but at the cost of limited tissue penetration ($<$2 mm). This high resolution allows assessment of both vascular endothelium and plaque structural components. Light is backscattered by blood and therefore to facilitate the light reaching the vessel walls a blood-free environment needs to be created, which poses a challenge in-vivo where near-continuous coronary perfusion is required. Initial time-domain based OCT systems were hampered by slow acquisition speeds and balloon occlusion of vessels to allow imaging was cumbersome. Subsequent advancements including the introduction of frequency-domain systems have allowed rapid pullback speeds of over 15 mm/s and accelerated clinical utility. With these contrast is used to clear the blood using a pressurised hand or pump delivered injection. The use of contrast for these image acquisitions ($\sim$15 mls/run) has implications for patients at risk of contrast-induced nephropathy (CIN). Furthermore the pressurised injection may introduce or propagate a coronary intimal dissection [17]. Saline has shown promise as an alternative flushing medium in patients at risk of CIN [18], but precludes angiographic co-registration of acquisitions. Recently developed Heartbeat OCT systems can allow full acquisitions within a single heart-

beat, minimising contrast required and reducing distortions generated by cardiac motion [19]. A randomized control trial comparing OCT guided to IVUS or angiographic only guided PCI showed non-inferiority of OCT to IVUS/angiography with respect to the primary endpoint of final median stent area [20]. A large cohort study of 123,764 patients undergoing PCI suggested a mortality reduction for OCT-guided PCI (7.7%) versus angiography-guided PCI (15.7%; $p<0.0001$) [21]. A large multi-centre randomized control trial (ILLUMIEN IV) powered to demonstrate superiority of OCT-guided PCI to angiography-guided PCI, with regards to clinical cardiovascular outcomes, is currently recruiting and due for completion in 2022.

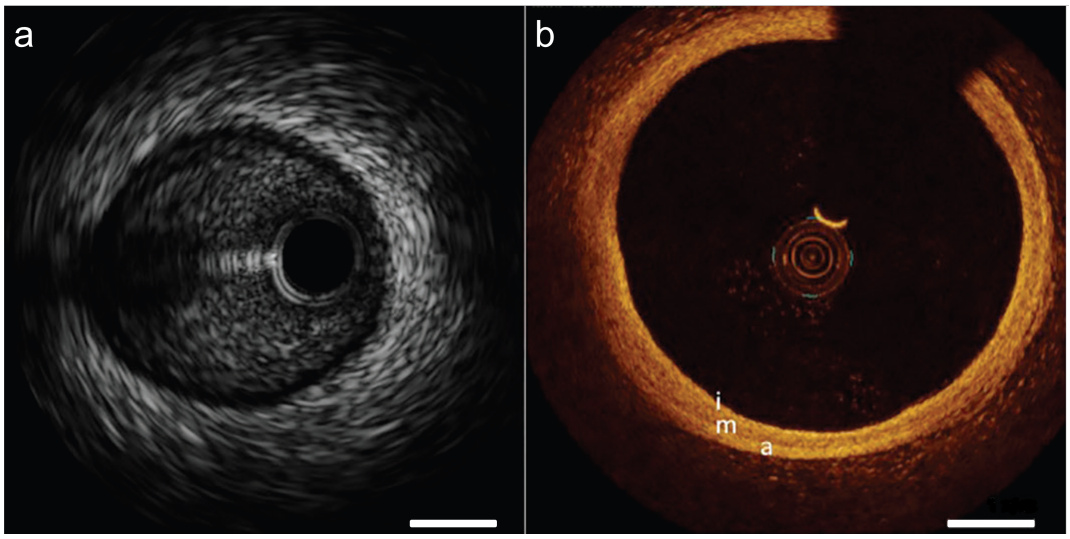

Figure 1.1: Normal Coronary artery as imaged by IVUS and OCT

a) IVUS imaging demonstrating lumen and surrounding vascular structures. b) OCT imaging demonstrating vessel lumen surrounded by a trilaminar structure. i = intima, m - media, a - adventitia. Scale bars represent 1 mm [5].

1.2.3 Molecular Characterisation

The PROSPECT trial, published in 2011, provided key insight into the natural history of coronary atherosclerosis. Patients presenting with an acute coronary syndrome underwent 3-vessel IVUS imaging following culprit lesion PCI. Over a 3 year follow-up period, the cumulative rate of major adverse cardiovascular events

(MACE) was 20.4%, with almost half of these events occurring in lesions not related to the original culprit. Of these non-culprit lesions the majority were deemed angiographically mild during the index procedure, suggesting that angiographic assessment alone of coronary anatomy is a poor discriminator for identification of high risk disease. Multivariate analysis highlighted a specific plaque morphology, thin-capped fibroatheroma (TCFA), to be at a particularly increased risk of causing future MACE (HR, 3.35; 95% CI, 1.77 to 6.36; P<0.001). Additionally a plaque burden, defined as a plaque-and-media cross-sectional area divided by external-elastic-membrane cross-sectional area, of $\geq$ 70% was associated with increased incidence of MACE (hazard ratio, 5.03; 95% CI, 2.51 to 10.11; P<0.001) [22]. Identification of these high-risk features during angiography may allow a targeted treatment approach to reduce the risk of future events [23], and is therefore of increasing clinical interest. Multiple techniques, hybridised with OCT/IVUS imaging, have shown promise at characterising atherosclerotic disease including Photoacoustics (PA) [24][25]. The paradigm of PA is that light from a laser source is delivered to vascular tissue. Then, depending on the absorption spectra of the constituents of that tissue, the light is absorbed, inducing a thermal change and resulting in US generation. Reflections of US are detected by a receiver which analyses the signal for image reconstruction. Other examples of hybridized techniques include Near-Infrared Spectrosocpy (NIRS) [26], Near-Infrared Fluoroscopy (NIRF) [27], Radiofrequency (also known as Virtual-Histology IVUS) [28] and Polarimetry [29]. The PROSPECT 2 trial [26] utilised one of these hybrid imaging platforms, a commercially available IVUS/NIRS system (InfraredX, Bedford, MA,US), to show that lesions with both a large plaque burden (>70%) on IVUS and large lipid-rich core ((Lipid Core Burden Index (LCBI) >324.7)) on NIRS had a 4-year MACE rate of 7·0% (95% CI 4·0–10·0) in comparison to a 4-year MACE rate of 0.2% for lesions with no high risk features. For the patients in whom one or more such of these lesions were identified there was a 4-year MACE rate of 13·2% (95% CI 9·4–17·6) in comparison to 5.2% for patients who had no such lesions identified ((OR 2·62 (95% CI 1·57–4·38) p=0·0002). These results complement those from

the ATHEROREMO-NIRS investigators who demonstrated that the presence of a lesion with a LCBI ≥ 43 conferred a four-fold increase in the occurrence of MACE over a 1 year follow-up [30]. Whilst the need for hybrid structural/compositional imaging appears clear, it has been challenging to incorporate elements for multi-modality imaging into hybrid catheters whilst maintaining the lateral dimensions (i.e $<$1mm) necessary for intravascular deliverability. Furthermore these elements do not necessarily work synergistically and add both complexity and cost into the fabrication process.

1.2.4 Guidelines

Guidelines are documents that guide decision making regarding the management of certain medical conditions. They are based on expert consensus opinion and a rigorous evidence base derived from clinical trials. For the management of coronary artery disease there are two main bodies that provide guidelines. These are the European Society of Cardiology (ESC) and the American Heart Association (AHA). The use of intravascular imaging features prominently in both. Currently there is a Class IIa (Evidence level B) recommendation, in the ESC [31] and AHA [32] guidelines, for the use of IVUS to assess the severity of unprotected left main lesions and optimise treatment. There is a class IIa (Evidence level B) ESC recommendation for OCT/IVUS assessment of angiographically intermediate non-left main coronary arteries stenosis [31]. Both modalities are recommended in selected patients to optimise stent implantation and have a class IIa (Evidence level B) ESC recommendation as well as for consideration to detect stent-related mechanical problems implicated in early failure or restenosis [31].

a

Classes of recommendations	Definition	Suggested wording to use
Class I	Evidence and/or general agreement that a given treatment or procedure is beneficial, useful, effective.	Is recommended/is indicated
Class II	Conflicting evidence and/or a divergence of opinion about the usefulness/efficacy of the given treatment or procedure.	
Class IIa	*Weight of evidence/opinion is in favour of usefulness/efficacy.*	Should be considered
Class IIb	*Usefulness/efficacy is less well established by evidence/opinion.*	May be considered
Class III	Evidence or general agreement that the given treatment or procedure is not useful/effective, and in some cases may be harmful.	Is not recommended

b

Level of evidence A	Data derived from multiple randomized clinical trials or meta-analyses.
Level of evidence B	Data derived from a single randomized clinical trial or large non-randomized studies.
Level of evidence C	Consensus of opinion of the experts and/or small studies, retrospective studies, registries.

Figure 1.2: Level of recommendation within guidelines

a) Class of recommendation within the guideline. b) Level of evidence provided to justify the class of recommendation [31].

1.3 Optical Ultrasound (OpUS)

1.3.1 Paradigm

Also known as optoacoustics or laser-generated US, the paradigm of OpUS is that US is generated and received using light rather than piezo-electric based components. With this, pulsed or modulated light is used to generate US via the photoa-

coustic effect at the surface of a fibre optic transducer [33]. This is made possible through the use of optically absorbing nanoengineered composite materials. These materials comprise two elements; the first being an optical absorbing agent that converts excitation light into thermal energy; the second is an elastomeric host which expands in response to the thermal energy. The resultant pressure rise propagates as an US wave. The generated US reflects off imaged structures and is detected using a fibre-optic ultrasound receiver (also known as a hydrophone).

1.3.2 Previous Work

As part of the department of Medical Physics and Biomedical Engineering at University College London UK, the Interventional Devices Lab (IDL) group have been pioneering OpUS development over the last 8 years.

1.3.2.1 Materials

Significant work has been undertaken evaluating the optimal material characteristics for OpUS transduction. As part of this several optical absorbing agents have been explored, including metallic nanoparticles [34], organic pigments [34] and carbonaenous materials [35]. Metallic nanoparticles have a relatively narrow window of optical absorption compared to alternative materials. Organic pigments, such as crystal violet, tend to exhibit photobleaching with resultant decreased acoustic conversion over time, due to poor photostability [34]. Carbonaceous materials are highly suited for OpUS generation as they are photostable and have high absorption across a broad optical spectrum. Examples of substances in this category include graphene [36], candle soot [37], carbon black [38], carbon nanofibers [39] and carbon nanotubes [40]. A significant breakthrough came when a team from University College London demonstrated for the first time that utilizing functionalized multi-walled carbon nanotube-polydimethylsiloxane (PDMS) composites for the OpUS paradigm, ultrasound pressures of 21.5 MPa at the coating surface and bandwidths of 39.8 MHz [40] can be generated. These high pressures have the potential to allow deep tissue penetration, whilst the broad bandwidths may allow for high axial resolution imaging. Through the use of alternative nanocomposite transducer coat-

ings, selective absorption of specific light wavelengths is possible, introducing the possibility of dual-modality photoacoustic (PA) imaging for tissue characterization or therapeutic optical ablation [34]. In addition to evaluating these materials, multiple differing fabrication techniques have been investigated for depositing these nanocomposite onto the distal surface of the fiber. This is of importance as it is desirable to ensure as small a coating thickness as possible on the fibre-optic surface, to minimize the affects of acoustic attenuation [41]. These include dip-coating [40], electrospinning [42] and spin-coating [43]. Out of these dip coating using a "bottom up" approach has shown the most promise. This method involves an initial stage of coating the fibre surface with an optical absorber and then subsequently applying a PDMS overcoat. The thickness of the nanocomposite with this method is determined by the viscosity of the material and can be controlled either through the addition of solvents or by altering the dipping speed of the optical fibre.

1.3.2.2 Hydrophone

A hydrophone is a sensor designed to detect sound waves transmitted through water. Traditionally these are based on a piezoelectric transducers that generate electric potential in response to the changes in pressure resulted by sound waves. In order to fit the paradigm of an all-optical method of generating and receiving ultrasound, an optical based hydrophone is desirable. Known as fibre optic hydrophones (FOH), these have gained popularity in a wide range of commercial applications due to their large dynamic range, high sensitivity, relatively small size and immunity to electromagnetic interference. As opposed to piezoelectric receivers, whose sensitivities reduce with decreasing element size, FOHs can maintain high sensitivities despite receiver sizes in the range of tens to hundreds of microns. One such method of detecting ultrasound is based on a Fabry-P*é*rot cavity, which comprises an optical cavity made from two parallel reflecting surfaces and interrogated using interferometry techniques. Recently Guggenheim et al., proposed a miniaturized high sensitivity receiver based on this concept, comprising an optical fibre tipped with a plano-concave polymer microresonator (known as a Fabry-P*é*rot cavity) [44]. An epoxy based dome with high-reflectivity coatings (mirrors) on both the domed

and planar surfaces is affixed to the distal end of an optical fibre. When US arrives at the dome it causes deformations in the dome surfaces, altering the distance between these points. These deformations can then be assessed using laser interferometry. The size of this receiver (<250 μm) makes it ideal for pairing with the aforementioned fibre optic transducer to allow for real-time pulse-echo US imaging using a miniaturized all-optical imaging device.

1.3.2.3 Imaging

The topic of previous OpUS imaging studies will be discussed extensively in the background section of Chapter 4 (Optical Ultrasound; Ex-Vivo Vascular Imaging). In brief it has been demonstrated, that using the OpUS paradigm, US pressures of 1.57±0.41 MPa at 1.5 mm from the US transmitter can be achieved with a -6db US bandwidth of 30.1±3.5 MHz. Through the use of high-pass frequency filtering, axial resolutions of <50 μm have been achieved at less than 5 mm depth and 59 μm at a depth of 10.5 mm. This represents a significant upgrade to conventional 40 MHz piezoelectric IVUS technology capabilities [36]. This technique has been successfully used to image vascular and cardiac tissue in an in-vivo swine model [45]. In addition, these imaging fibres have been integrated into a first of its kind interventional device, designed to facilitate trans-septal puncture for left atrial electrophysiology studies [45].

1.3.3 Benefits

Optical generation of ultrasound in this manner offers significant advantages over electronically generated ultrasound. Broad bandwidths allow for higher spatial resolution, equivalent to 60 Mhz high definition IVUS, whilst maintaining tissue penetration >10 mm [36]. Optical fibres are low in profile and highly flexible, therefore suitable for incorporation into miniaturized interventional devices. The absence of electronics allows for MRI compatibility and minimizes the effects of electromagnetic interference. Furthermore through the use of nanocomposite materials that are selectively absorbing at specific wavelengths there is the potential for hybrid imaging with OCT [46] or PA [47]. Dual imaging/therapeutic applications, such as the

real-time monitoring of tissue ablative procedures, may also be realised [48].

1.3.4 Current Limitations

Currently OpUS has been demonstrated in a forward-viewing configuration. Clinical utility for the assessment of coronary vessels, however, requires a side-viewing orientation in order to generate a rotational image. Further work is required to develop post-processing algorithms in order to optimise the image quality and reduce artefact. Additionally these elements need to be incorporated into a robust medical device, with suitable characteristics and dimension, to enable successful in-vivo imaging. Finally there is a lack of validation of this imaging modality against both other gold-standard imaging techniques and histology.

Chapter 2

Mesoscale Imaging Phantoms

The work of this chapter is based on my publication below:

'Micron resolution, high-fidelity three-dimensional vascular optical imaging phantoms'
Little CD, Poduval RK, Caulfield R, Noimark S, Colchester RJ, Loder CD, Tiwari MK, Rakhit RD, Papakonstantinou I, Desjardins AE (2019).
Journal of Biomedical Optics 24(2)
https://doi.org/10.1117/1.JBO.24.2.020502

2.1 Introduction

Phantom models are important tools that aid the development and characterisation of emerging imaging technology. Broadly speaking, within the field of intravascular imaging, phantom models can be divided into two main categories. Those that characterise resolution and performance of a given system (Resolution phantoms) and those that provide an realistic simulation of the properties of a given imaged structure (Tissue-mimicking phantoms). In this chapter I will discuss the development of a new hybrid fabrication process for creating both of these types of phantom model which are suitable for intravascular OCT. OCT was the imaging modality chosen as this modality currently possesses the highest axial resolution capability (10 μm) of the widely available intravascular imaging technologies. The method proposed, however, is applicable for creating phantoms suitable for alterna-

tive imaging techniques such as IVUS and OpUS. These phantoms are referred to as mesoscale imaging phantoms as the dimensions involved are between the micron to millimetre scale.

2.1.1 Resolution phantoms

Typically there are two main types of phantom model for resolution characterization. The first type is based on the concept of the 1951 USAF resolution test chart. With this a repeating pattern of lines and spaces, at incrementally decreasing predetermined sizes (line pairs per millimetre), is imaged. The modulation transfer function, which compares the observed image to spatial frequencies, can be used to determine the resolution of a given system. Several studies have demonstrated OCT resolution phantoms based on this concept, fabricated either through femtosecond laser micro-inscription [49] or multi-layer silicone film spin-coating [50]. A major limitation of this method is that characterization only occurs in two dimensions and is therefore not suitable for rotational systems. The second type of resolution phantom involves the inclusion of sub-resolution sized scattering particles or nanoshells within an imaging medium. Using these particles as targets, a point spread function can be characterized defining resolution of a system in both lateral and axial terms. This has been demonstrated using gold nanoshells ($\sim$196 nm diameter) within cured silicone [51] and silica microspheres ($\sim$1500 nm diameter) or iron oxide ($\sim$300-800 nm diameter) within epoxy [52]. Phantom fabrication in this manner does not allow specific geometrical positioning of these particles as their distribution within a medium is random, exposing them to the risk of aggregation. Imperfections within the medium may also create variability of the measurements obtained. Clinical intravascular imaging occurs using rotational catheters. An ideal imaging phantom for these modalities would include multiple targets of differing sizes, at distinct geometrical locations, in order to accurately characterize resolution capabilities and also quantify both subsampling in the angular domain and image distortion due to non-uniform rotation. To date this has been challenging and presents a current gap in the literature. Advances within microscale fabrication using nanoscopic additive methods with photoresists offers the potential to overcome these challenges. Two

photon polymerization (2PP) is a leading technique within this field which, depending on the photo-sensitive polymer used, offers sub-micron scale 3D printing to a resolution of less than 200 nm [53]. The concept is summarised in Figure 2.1. Cross-linking within a photocurable polymer occurs through exposure to a focused femtosecond laser beam [54]. The polymer requires a threshold of 2 photons to be reached before cross-linking occurs, allowing a highly localized volume to be targeted [55]. Non-polymerized material can be washed out using propylene glycol monomethyl ether acetate, a photoresist solvent, leaving behind the printed model. This technique has been successfully used for microfabrication of cell colonization scaffolds and represents an attractive option for phantom fabrication [56].

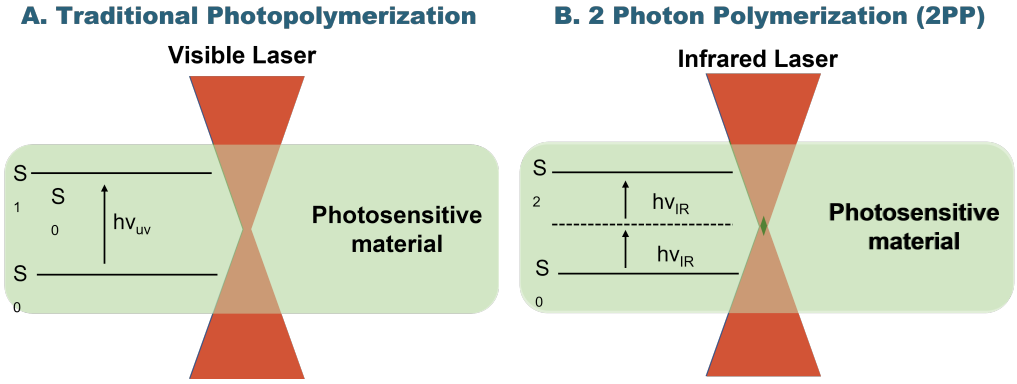

Figure 2.1: 2 photon polymerization printing process

A) With traditional photopolymerization techniques visible light from a laser source is directed at a photosensitive material (green rectangle). The energy delivered (hvUV) induces cross-linking within the material (red triangle). This material does not have a specific threshold at which cross-linking occurs and therefore even with a tightly focused beam there is still a large area of polymerization. B) With 2PP a tightly focused femtosecond laser beam is used to deliver energy to the photosensitive material. Within this material cross-linking only occurs where a 2 photon energy threshold (HvIR + HvIR) is reached (green diamond).

2.1.2 Tissue-mimicking phantoms

In addition to providing resolution targets, phantom models that replicate the anatomical appearance and molecular contrast of vascular structures can guide image interpretation and appreciation of how these present with a given imaging technique [57]. Significant work has been undertaken to generate tissue-mimicking

	Scatterers	Advantages	Disadvantages
Silicone	Titanium dioxide, Silica, alumina	Widely available, Robust after curing, uniform refractive index similar to tissue	Non-Organic
Hydrogels	Polystyrene nanoparticles	Cheap	Short shelf-life and semi-solid at room temperature
Resins	Titanium Dioxide	Durable	Much stiffer than vascular tissues
Fibrin	Blood, Lipid	Compatible with organic scatterers	Difficult to fabricate
PVA-C	Alumina	Controllable mechanical properties	Non-Organic

Table 2.1: Comparison of phantom base materials

materials (TMM) with optical absorption and scattering properties equivalent to vascular tissues. Light emitted from an intravascular OCT catheter is subject to both attenuation and backscattering as it passes through tissues, along an incident path. Light that is backscattered from a surface then returns to the probe and is subjected to further attenuation and backscattering [58]. The degree to which light is backscattered is determined by both the anisotropy of the tissue and its attenuation coefficient. This in turn alters the strength of the returning signal and can allow differentiation of tissue structures and constituents [59]. The materials used within phantoms should ideally have both backscattering amplitudes and attenuation coefficients that are closely matched to the desired tissues that they are simulating. As previously mentioned phantom model materials usually constitute of a base matrix within which scattering agents can be integrated. Several different materials have been used including hydrogels [60], resins [61], fibrin [62] and poly(vinyl alcohol) cryogels (PVA-C)[63], however silicone remains the most prominent of these [64][57]. The advantages and disadvantages of these various materials are summarized in Table 2.1.

Regardless of the tissue mimicking materials used, it has been challenging to

model these with heterogeneity in all dimensions, and at the micron to millimeter size scales relevant to small vascular structures. Various methods have been proposed to generate phantoms with suitable architecture including, sequential molding [65], where separately cured components are brought together to form a final structure or soft lithography, where negative casts are generated using photo-lithography [66]. Additionally, tubular structures mimicking both healthy and diseased vascular structures have been demonstrated using deposition curing on a rotating lathe set-up [57][67]. 3D additive printing technologies offer a viable method for the fabrication of scaffolds that resemble biological structures, however not at the mesoscopic scale relevant to a number of anatomical structures [68][69]. 2PP may offer a suitable method for fabricating mesoscale scaffolds, into which tissue mimicking materials can be introduced.

2.2 Aims

To assess the feasibility of a novel hybrid fabrication process utilising 2PP to create i) a resolution phantom capable of performance characterisation; ii) a side-branch phantom, capable of demonstrating complex vascular anatomy; iii) a lipid plaque phantom, capable of simulating high risk pathology.

2.3 Methods

2.3.1 Phantom Design

2.3.1.1 Resolution Phantom

Initial design of a mesoscale wire phantom model, suitable for characterization of optical systems, took place using a cloud-based computer aided design (CAD) software (Fusion 360, Autodesk Inc, San Rafael, Ca, US). Designs on this software can be exported as a standard tessellation (STL) file which is compatible for 3D printing technologies. The design (Figure 2.2.a) consisted of a central cylindrical channel with a diameter of 1 mm, through which an OCT imaging probe (outer diameter (OD): 0.9 mm) could be introduced, to facilitate a pullback rotational acquisition. 28 Wires were arranged in a circular pattern, with each wire centered at a distance

of 0.7 mm from the central channel. Beginning with the thinnest wire (OD: 5 μm), the wire OD was augmented by 1 μm increments in a clockwise fashion at an angular interval of 12° to reach a maximum OD of 34 μm. The diameter of 5 μm was chosen for the smallest wire as this is a factor of 2 lower than the quoted resolution limit of the commercial OCT system used in our setup. The addition of side and base plates to the model provided increased structural stability.

2.3.1.2 Side-Branch Phantom

Vascular anatomy is both variable and complex consisting of multiple bifurcations, where a main vessel gives rise to a side-branching vessel. Fabrication of a phantom that replicates this geometry incorporated a hybrid technique of 2PP printing of a scaffold model and micro-injection of TMM into the scaffold. The design of the vessel side-branch phantom model is shown in Figure 2.2.b. This comprised a main vessel (OD: 1 mm; length: 2 mm) with a side branch (OD: 0.6 mm) that bifurcated from the main vessel at an angle of 45°. This geometry is consistent with that found in the distal coronary arteries [70]. These vessel structures were contained within a 2 mm open-topped cube, to allow a cavity into which TMM could be introduced, surrounding these vessel structures.

2.3.1.3 Lipid Plaque Phantom

Atherosclerotic plaque is made up of multiple constituents with heterogeneous optical contrast. To demonstrate how this hybrid fabrication method of using 2PP printing and TMM micro-injection can simulate vascular pathology, a phantom model with a scaffold replicating a lipid-rich thin capped fibroatheroma (TCFA), was designed. TCFAs are of increasing clinical interest as their presence is thought to increase the risk of developing a myocardial infarction [22]. TCFAS are not visible with X-ray fluoroscopy and therefore the use of intracoronary imaging technology is crucial in their detection. The hallmark of a TCFAs is a large necrotic lipid rich core covered by a thin (less than 65 μm) fibrous cap [22]. Identifying these lesions may provide a cohort of patients that would benefit from aggressive lipid lowering therapies [71]. Accordingly, the design (Figure 2.2.c) consisted of a vessel supported within a 2 mm open top cube to replicate a coronary artery. An arc-shaped

cavity close to the vessel lumen was included, creating a region into which lipid could be microinjected in order to simulate the necrotic core. Outside this cavity and the vessel lumen, there was a second region in which the optically scattering silicone/TiO_2 mixture could be introduced. This second region extended into a narrow gap between the vessel lumen and first region, representing the fibrous cap of the TCFA (50 μm in diameter).

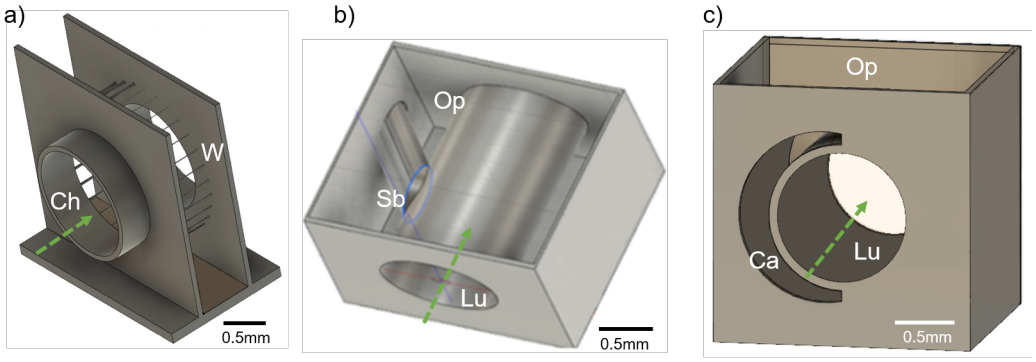

Figure 2.2: Mesoscale phantom computer aided designs

a) Resolution phantom; Ch is the central cylindrical channel with wires (W) arranged in a circular pattern around the centre. Base and side plates included for print stability. The green dashed arrow represents the intended passage of the IVOCT catheter. b) Side-branch phantom; Lu is the main vessel lumen with SB the side-branch. These structures are contained in an open-topped cube (Op), which provides a compartment for TMM to be included. c) Lipid plaque phantom; Lu is the main vessel lumen with Ca providing an arc-shaped cavity for the lipid mimicking material to be introduced. Op is the open topped compartment for TMM to be introduced.

2.3.2 Phantom Fabrication

2.3.2.1 Resolution Phantom

Printing using the 2PP technique was performed with a commercial system (Photonic Professional-GT; Nanoscribe GmbH, Eggenstein-Leopoldshafen, Germany) [72]. The photocurable polymer used as the printing substrate was IP-S, a proprietary photoresist which has been optimized for mesoscale structure fabrication [73]. All 2PP fabrication was undertaken on glass slides coated with an optically transparent film of Indium Tin Oxide (ITO). After the 2PP process, the model was developed for 90 minutes in propylene-glycol monomethyl-ether-acetate (PGMEA)

solvent, followed by 5 minutes in isopropyl-alcohol (IPA). Uncured photoresist was washed out by the PGMEA. The 3D printed model was then separated from the ITO-glass substrate by immersing it in concentrated hydrochloric acid for 5 minutes, followed by de-ionised water and then IPA for 2 minutes each. Following 2PP printing, the mesoscale wire phantom model was affixed to an uncoated glass slide using a UV-curing epoxy, which was transferred onto the sides and base of the model with a cleaved optical fibre. The completed model was imaged under both an optical and scanning electron microscope (SEM) to determine the accuracy of the print and assess the appearance of the small wires (Figure 2.4).

2.3.2.2 Side-Branch Phantom

The scaffold for the phantom model was printed using the aforementioned 2PP process. Following attachment to a glass side with an ultraviolet-curing epoxy, optical microscopy confirmed the fidelity of the 2PP printing process. At the size scales of these printed structures, the polymerized photoresist used is optically transparent (propagation losses of 4.38 dB/cm at 633 nm wavelength) [74]. For the TMM, a combination of a commercially available poly(dimethyl siloxane) (PDMS) (Sylgard 184, Dow Corning, Midland, MI, US), Titanium Dioxide (TiO2) nanoparticles, and silicone oil was utilized. To achieve tissue-mimicking optical backscattering, the TiO_2 nanoparticles with a nominal primary particle size of 21 nm (13463-67-7, Sigma-Aldrich, Germany), were included in a concentration of 2 mg/ml [75]. PDMS has a relatively high viscosity at 3000 - 10,000 cps. The silicone oil (Silicone Thinner, Smooth-On, Bentley Advanced Materials, UK) decreased the viscosity of the mixture and allowed for easier integration into the phantom models, minimizing the risk of entrapped air bubbles. Sylgard 184 comes in two parts with a resin requiring a reactive component to initiate curing. This was combined in a 10:10:1 ratio of silicone oil:PDMS resin:cross-linking agent. Following mechanical stirring, the sample was sonicated for 30 minutes to ensure that the TiO_2 nanoparticles were uniformly distributed to provide scattering homogeneity. Formal assessment of particle distribution was not performed. The mixture was then degassed within a vacuum chamber for 30 minutes to allow for complete removal of any entrapped air.

Once fully prepared, this mixture was transferred to the printed scaffold model by using a cleaved optical fibre to deposit the material into the open-topped chamber. The integrated model was then placed in a convection oven and heated to 100°C for 1 hour allowing uniform curing.

2.3.2.3 Lipid Plaque Phantom

The silicone consisting of the previously-described PDMS (Sylgard 184), silicone oil, and TiO_2 mixture was introduced into the main body of the phantom model, using a cleaved optical fiber. The model was then cured at 100°C for 1 hour. Coconut oil was used as the lipid mimicking material to simulate the lipid pool. The aperture size of the arc-shaped cavity (<235 μm) was much narrower than that of the main open topped compartment and therefore the previously used method of transferring material with a cleaved optical fibre proved unsuitable. Glass micropipettes provided a practical solution to this, by allowing precise introduction of small volumes of the lipid mimicking material into the 2PP printed scaffold, under direct visualization [76]. This process is demonstrated in Figure 2.3. The micropipettes were manufactured using a micropipette puller (P–1000, Sutter Instrument, Novato, Ca, US). They had a long 3 mm taper to diameter at the tip of 50 –60 μm. Coconut oil has a low melting point of 23-27°C [77] and therefore once warmed was a suitable material for micro-injection using the micropipette. To enable easy coupling with syringes, Luer lock adapters (EFD 15-gauge tips, Nordson, Westlake, Ohio, US) were fitted. In preliminary tests with these glass micropipettes, injection generated large droplets of material that built up on the outside walls of the micropipettes, resulting in accidental spillage into unintended structures, such as the central imaging lumen. This challenge was overcome by functionalizing the micropipettes with a mixture of perflurooctyl-trichlorosilane and hexane in order to induce oleophobicity. For the purpose of orientating the arc-shaped cavity facing upwards, the 2PP printed scaffold was mounted to an aluminum block. A syringe containing the lipid mimicking material, coupled to the micropipette, were then positioned above the opening with a 3-axis translational stage (Thorlabs Inc, Newton, NJ, US). With the aid of an objective lens (M Plan Apo SL 50X, Mitutoyo UK

Ltd, Andover, Hampshire, UK) and a complementary metal oxide semiconductor sensor camera (DCC1545M, Thorlabs Inc, Newton, NJ, US) the exact position of the micropipette was monitored and precisely adjusted adjusted. The micropipette was lowered into the arc-shaped cavity under direct visualization and then applied a pneumatic back-pressure to the syringe (VPPM Proportional-pressure regulator, Festo Belgium, Brussels, Belgium) to inject lipid-mimicking material from the tip. Once fully integrated, the phantom was cooled to 4 °C allowing the coconut oil to solidify, prior to imaging.

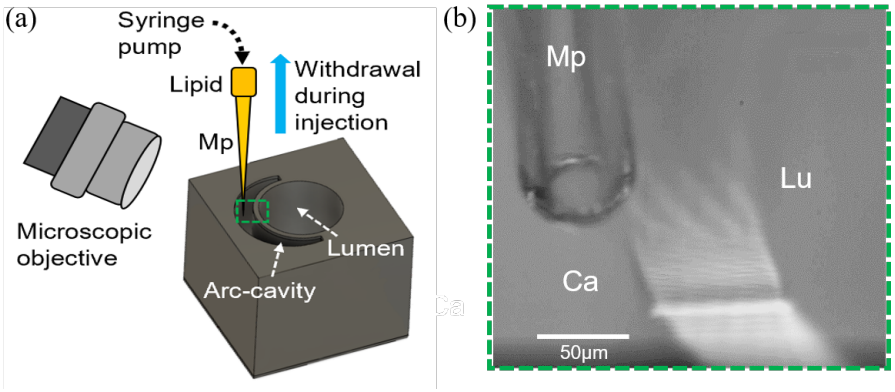

Figure 2.3: Fabrication of lipid plaque phantom

a) Schematic showing injection of liquid coconut oil, as the lipid mimicking material, via a functionalised micropipette (Mp) into the arc-cavity. b) Optical microscopy of the dashed-green region in Fig 2.4.a, showing the micropipette (Mp) positioned above the arc-cavity (Ca) prior to injection. The area between the arc-cavity (Ca) and the lumen (Lu) is filled with TMM and represents the fibrous cap of the arterial plaque.

2.3.3 OCT Imaging

The mesoscale wire phantom model was imaged using a commercial IVOCT probe (ILLUMIEN OPTIS IVOCT imaging system and Dragonfly Duo imaging catheter; St Jude Medical, St Paul. MN, US). This system operates in the 1250 - 1350 nm spectral range. The model was attached to a stand and submerged in a water bath at room temperature ($\approx$ 18°C). The imaging catheter was passed through the central cylindrical channel of the phantom model. In the case of the mesoscale wire phantom model images were acquired in a stationary position with an acquisition speed of 180 frames per second. This was to allow frame averaging (540 frames)

to facilitate resolution characterisation. Although frame averaging is not utilised in-vivo it was performed to improve the accuracy of the imaging. For the vessel side-branch and the lipid plaque phantom models imaging was performed using an automated 2-axis translation stage (Thorlabs Inc, Newton, NJ, USA). Images were acquired with a controlled pullback speed of 0.89 mm/s, to ensure that the entire length of the phantoms ($>$ 2 mm) were imaged during the acquisition period (3 s) and that the number of frames of the phantom acquired was maximised. In-vivo the pullback speed of the system is set to 12 mm/s, however this is to ensure that sufficient vessel length is imaged (54 mm).

2.4 Results

2.4.1 Resolution phantom

The completed model was imaged under both an optical and scanning electron microscope (SEM) to determine the accuracy of the print and assess the appearance of the small wires (Figure 2.4). Figure 2.5 shows the IVOCT acquisition from within the phantom.

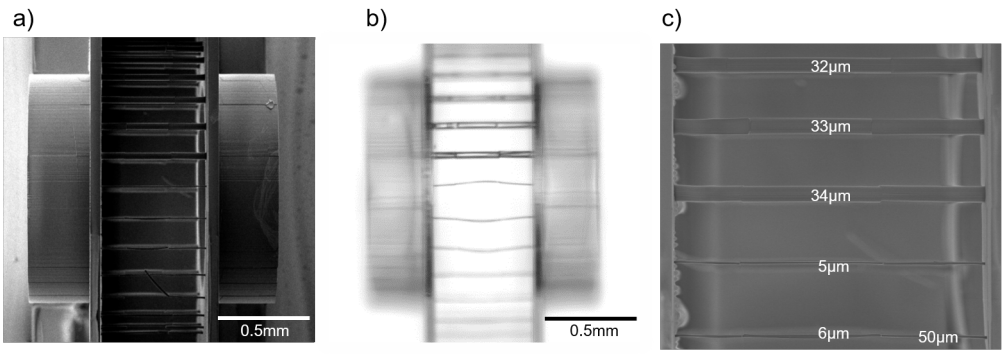

Figure 2.4: Microscopy of the printed resolution phantom

a) Scanning Electron Microscopy (SEM) image of the resolution phantom model and b) corresponding optical microscopy. c) SEM image of the transition region that spans the thickest (34 µm) and thinnest (5 µm) wires

Figure 2.5: OCT of the resolution phantom

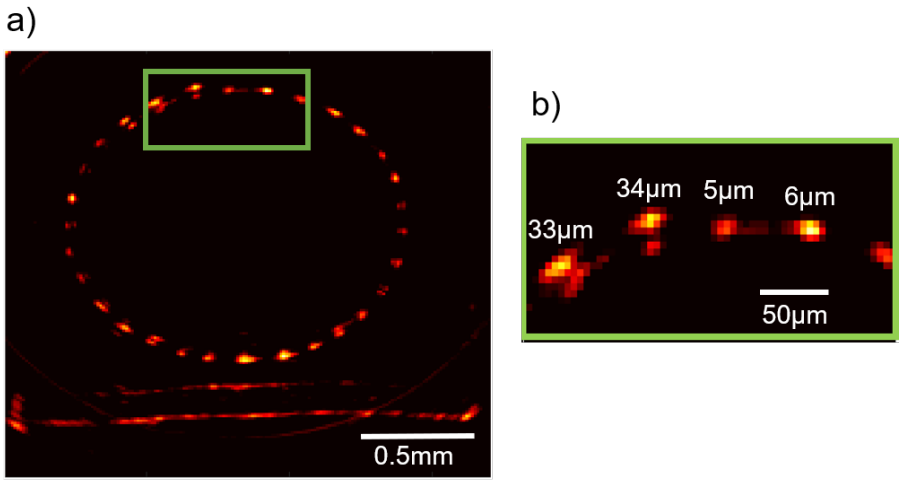

a) Single averaged frame from IVOCT stationary acquisition. The IVOCT catheter has been digitally subtracted from the centre of the channel. The wires are visible as an interrupted circular structures around the channel. The transition point from the largest diameter wire to the smallest diameter wire is in the 12 o'clock position. The base plate is visible below as a rectangular structure. b) Magnified view of the transition between the largest diameter wire (34 μm) and the smallest diameter wire (5 μm).

2.4.2 Side-branch phantom

Optical microscopy of the side-branch phantom is demonstrated in Figure 2.6.a. On the cross-sectional IVOCT display shown in Figure 2.6.b the vessel side-branch can be clearly visualized exiting the main lumen in the 12 o'clock position. The tissue mimicking material is visible as a homogeneous scattering medium surrounding the lumen and the side-branch. The entire acquisition was post-processed in a medical image viewer (Horos, Nimble Co LLC d/b/a Purview, Annapolis, MD, US) to generate a 3D reconstruction demonstrating the vessel side-branch (Figure 2.6.c).

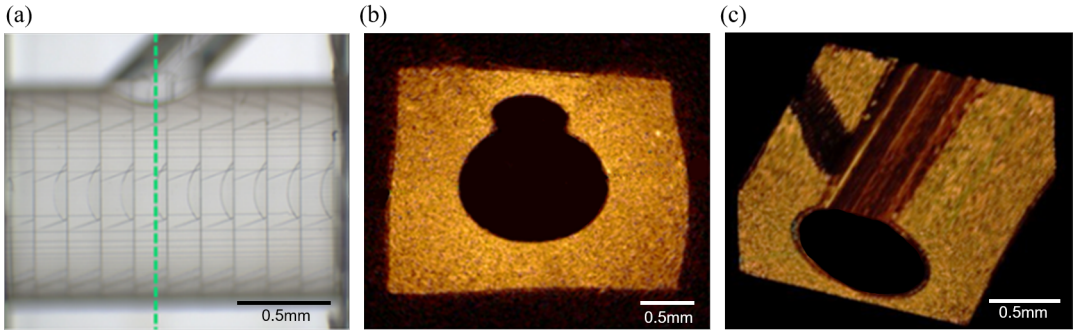

Figure 2.6: Microscopy and OCT of the Side-branch phantom

a) Bird's-eye view optical microscopy of the side-branch phantom. (b) IVOCT image acquired from the side-branch region (dashed green line in b). (d) 3D reconstructed IVOCT image volume.

2.4.3 Lipid plaque phantom

On IVOCT imaging the lipid core appeared as a hypoechoic area and there was slight shadowing behind this region that likely resulted from optical attenuation by the lipid (Figure 2.7). This appearance of microscale regions with distinct optical contrast is consistent with the molecular distribution that would be expected within a diseased vascular structure.

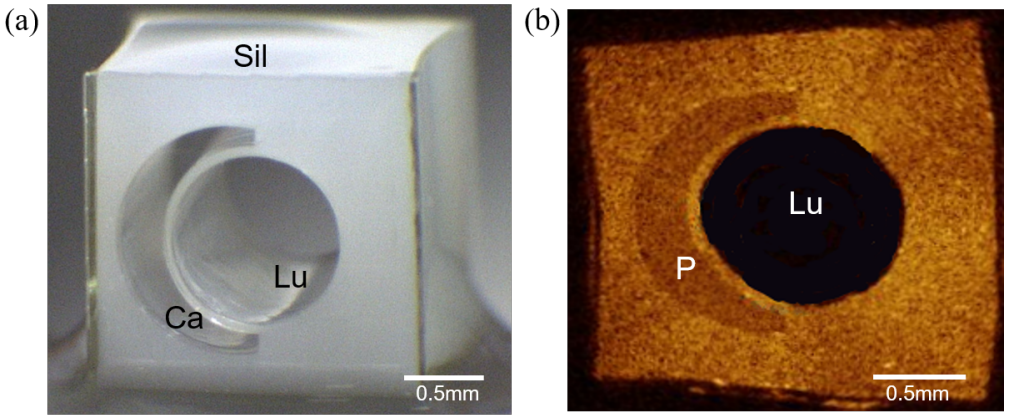

Figure 2.7: Microscopy and OCT of the Lipid plaque phantom

a) Optical microscopy of the model, after the main body was filled with optically scattering silicone (Sil), where the main lumen (Lu) and the arc-cavity (Ca) are unfilled.b) IVOCT image of the phantom model, in which arterial plaque (P) presents as a region with decreased scattering and with shadowing farther from the lumen (Lu) center. The region between the lumen and the plaque represents the fibrous cap.

2.5 Discussion

Fabricating phantom models using this hybrid approach of 2PP printed scaffolds and micro-injection of tissue mimicking materials offers several key advantages. 2PP printing allows for the simulation of highly complex vascular geometries, and micro-injection using the functionalized micropipettes allows for significant optical heterogeneity. Here a phantom model with a single bifurcating vessel side-branch was demonstrated; however, multiple branches of differing orientations and sizes can be realized. There is the option to import patient-specific geometries from high-resolution imaging modalities in order to generate freeform CAD files. These files can be readily shared in digital form, using cloud based software, allowing multiple research institutions to benefit from the designs. The IPS photoresist when cured is rigid with a refractive index of 1.515, Young's modulus of 5.1 GPa and a degradation temperature of 286°C [78]. Once cured, these fabricated phantom models were robust, showing no apparent damage despite repeated imaging from IVOCT imaging catheters after a period of 3 months. The smallest feature that was included in the mesoscale wire phantom was 5 μm in diameter, acting as a resolution point target for IVOCT. 2PP printing technology has the potential to print structures as small as 200 nm, dependent on the photoresist used[78], which may prove useful for imaging techniques with higher resolution capabilities. The printed wires were not measured to confirm accuracy, however, the resolution of the printer used is 160 – 200 nm (lateral) and 500 – 600 nm (vertical). Differences in 1 μm would therefore be expected to be realised. One observation that was made was that for extended, wire-like structures, it can be useful to limit the aspect ratio in order to achieve structural stability. Small structures with an aspect ratio of $>$100 tended to fail during the printing process as they were extremely fragile and susceptible to stitching artifact. As with other 3D printing technologies there are limitations on the geometry of print that is achievable, dependant on the orientation of the print, and some unsupported structures may not be realised. This technology, although commercially available, does represent a relatively high cost ($>$£250,000 for a Photonic Professional GT2 Nanoscribe printer) method for phan-

tom fabrication. The printing time was approximately 8 hours per model. Other 3D printing technologies, such as stereo-lithography, can also be used to fabricate the scaffolds used for the anatomical phantom models [79], provided the size of the included structures does not exceed the resolution capabilities of the system used. The coconut oil was chosen in the lipid plaque phantom to provide optical contrast, representative of a lipid pool. This was a suitable material as it had a low melting point, facilitating integration into the small cavity with the lipid plaque phantom. It would be of interest in future work perform a quantitative comparison to lipid from ex-vivo atherosclerotic plaque. Lipid type has an impact on near infrared spectrum and optical scattering is influenced by micro-architecture and macrophage infiltration which is likely to be variable from patient to patient. These differing aspects give rise to the overall appearance in-vivo [80]. It important to note that the relatively low melting point of the oil requires imaging at below 18 °C which may affect the optical appearance of the materials used compared to the expected appearance at body temperature. Additionally, the inclusion of coconut oil within the lipid plaque phantom presents several challenges to the long-term durability of the model. Firstly, refrigeration of the model during storage is required to prevent leakage of material. Secondly, as an organic compound the lipid is susceptible to decomposition. With this degradation the exhibited optical properties will change and the qualitative appearance of the phantom may be affected. One solution to this would be to use an inorganic lipid mimicking material. Lipid is highly attenuating to light and so the lipid mimicking material would need to exhibit this characteristic. Carbon black particles have been shown to provide realistic attenuation when included in silicone based phantoms [57] and may provide a suitable alternative. Attempts were made to produce a lipid plaque phantom using a concentration of 0.8 mg/ml [67] to the silicone/TiO2 mixture. The carbon black used had a particle size of 50 nm diameter and a specific gravity of 1.7 –1.9. This mixture was sonicated and degassed before integration into the printed scaffold. Unfortunately, this lipid mimicking material did not provide the qualitative visual representation of lipid that was expected. It proved challenging to ensure homogeneous dispersion

of the carbon black particles as they tended to agglomerate and block the tip of the micropipette during material transfer. As a result, the concentration of carbon black within the deposited lipid-mimicking material was likely to be significantly less than expected. For the purposes of this study a lipid rich TCFA was chosen as the pathology to simulate as this has been implicated in the mechanism of plaque rupture mediated myocardial infarction [22][81]. It would also be of interest, in future work, to develop phantoms that simulate calcification and coronary stent structures as intravascular imaging has roles in the assessment of both of these [82][83]. A limitation of the printing method used is that the refractive index of the IP-S photoresist (1.49 in the near-infrared spectral range) [84] is greater than that of tissue (1.36 –1.43). The mismatch between the photoresist and tissue-mimicking materials may therefore generate brighter boundaries than would be expected on imaging vascular tissues. In future work this effect could be mitigated by imaging within fluids that have higher refractive indices. As 2PP fabrication of mesoscale structures can be achieved for photosensitive materials with a range of refractive indices (1.3 –1.54 [84]), there is the potential to directly print phantoms containing multiple photosensitive materials with different optical properties designed to match the optical characteristics of tissue. Additionally, the spatial resolution of 2PP printing could enable inclusion of complex minute capillary networks for fluid flow phantoms, which are of interest in a wide range of imaging techniques [85]. Furthermore, specific to florescence imaging, there is the option to introduce fluorescence labeled cells or fluorophores into fabricated mesoscale structures [86], as has been demonstrated with other 3D printing technologies [87]. This method for fabrication is suitable for OCT imaging phantoms due to the structure dimensions and the TMM utilised. OCT was chosen as the intravascular modality for phantom validation due to its high resolution capabilities and widespread commercial availability of this technology. This fabrication method, however, would be appropriate for creating phantoms suitable for other imaging technologies by tailoring the TMM to that chosen modality [88]. It would be of interest, in future work, to evaluate the performance of these phantoms using IVUS and OPUS.

2.6 Conclusion

This hybrid approach of optically-generated 3D scaffolds and micro-injection of tissue mimicking materials will facilitate complex imaging phantoms for a wide range of microscopic and mesoscale optical imaging techniques.

Chapter 3

Patient-specific Vascular Multimodality imaging Phantoms

The work of this chapter is based on my publication below. The concept was to develop large scale anatomical models that could be used for benchtop characterisation of interventional devices such as the OpUS imaging catheters, described in Chapter 1, and simulation of procedures that are additionally guided by external imaging modalities such as computerised tomography.

'A Patient-Specific Abdominal Aortic Aneurysm multi-modality imaging phantom'

Little CD, Mackle EC, Maneas E, Chong D, Mastraccia TM, Desjardins AE, (2022). *International Journal of Computer Assisted Radiology and Surgery* https://doi.org/10.1007/s11548-022-02612-4

3.1 Introduction

3.1.1 Vascular targets for multimodality imaging

Certain vascular structures are of interest to clinicians due to their high incidence or corresponding morbidity of pathology. Multiple imaging modalities may be utilised in the assessment of these structures due to the complementary information provided. Two commonly assessed vascular structures of interest are the Carotid artery and the Abdominal Aorta.

3.1.1.1 Carotid artery

The carotid artery is the main arterial conduit that supplies the head and neck with oxygenated blood. Anatomically this structure consists of a common carotid artery, bifurcating into the internal and external carotid arteries. Atherosclerotic disease within these vessels can precipitate ischaemic cerebrovascular events, either through plaque rupture with vessel occlusion or by plaque embolization. Significant carotid artery luminal narrowing has been reported in up to 20% of patients with anterior circulation strokes [89]. Imaging of the carotid bifurcation is recommended by the Society for Vascular Surgery guidelines in patients who develop neurological symptoms consistent with a CVA or in asymptomatic patients who are deemed at high risk (history of peripheral vascular disease with multiple risk factors for atherosclerotic disease) or those who are awaiting coronary artery bypass grafting [90]. Carotid artery duplex ultrasound (DUS), a form of transcutaneous US, remains the most widely used imaging modality to screen for carotid disease. This is due to the widespread availability of ultrasound, which provides both anatomical data and flow parameters such as peak systolic velocity (PSV). It has been reported that using a PSV of $\geq$ 230cm/s has a sensitivity of 99% and specificity of 86% for predicting a stenosis of $\geq$ 70%, which is deemed significant [91]. Other non-invasive imaging modalities recommended as options for assessment of carotid disease include magnetic resonance angiography (MRA) and computed tomography angiography (CTA). Whilst the sensitivity (88%) and specificity (84%) of MRA for diagnosing a stenosis of $\geq$ 70% is similar to DUS [92], it is not suitable for patients with ferromagnetic devices such as non-MRI safe pacemakers/defibrillators or patients with claustrophobia. The gadolinium used as a contrast agent is contraindicated in pre-existing severe renal impairment due to the risk of nephrogenic systemic fibrosis. CTA provides superior resolution to MRA and has an 85% sensitivity and 93% specificity at detecting a stenosis of $\geq$ 70% [93], however it requires the use of ionising radiation and extensive calcification can lead to disease overestimation. A multimodality carotid phantom compatible with these three imaging modalities would provide a powerful research tool for emerging technologies.

3.1.1.2 Abdominal Aorta

The Aorta is the largest diameter vascular structure in the human body. It carries oxygenated blood directly from the heart and gives rise to the majority of the arterial conduits. The abdominal aorta, defined as the section of aorta extending from the diaphragm to the common iliac artery bifurcation, is of particular interest due to the propensity for aneurysm formation. An abdominal aortic aneurysm (AAA) is defined as a progressive dilatation of the abdominal aorta to greater than 3.0 cm or $\geq$ 50% of the suprarenal aortic calibre. It affects around 1.3% of men in the UK aged between 65-74 years [94]. Current recommendations from the European Society for Vascular Surgery suggest patients should be referred for aneurysm repair with aortic diameters of $\geq$ 5.5cm [95], above which, dependant on the size of the aneurysm, the annual risk of a potentially fatal aneurysm rupture is between 3.5-6.3% [96]. Similar to the assessment of carotid disease, ultrasonography in the form of abdominal ultrasound (US) and duplex ultrasonography (DUS) are the primary imaging modality used, due to availability of access and high sensitivity/specificity for diagnosis [97]. Current recommendations are that all men over the age of 65 should be offered an abdominal ultrasound for screening purposes. Due to a paucity of clinical data, MRA is not routinely used in the assessment of AAA, but represents a promising tool for further research [95]. CTA is crucial for the planning of aortic interventions given its high resolution ($\leq$ 1mm slice) and ability to provide a complete data set on the orientation of major side-branches. In addition to external imaging, intravascular ultrasound (IVUS) provides operators with the ability to directly visualize side-branch anatomy during EVAR procedures and has been associated with decreased fluoroscopy time and contrast usage [98]. Therefore, the ideal aortic aneurysm phantom model would be able to replicate the complex and highly variable geometry of an abdominal aortic aneurysm, with both CTA, US/DUS and IVUS compatibility. Furthermore, phantom models can also provide opportunity for benchtop characterization of emerging procedural devices and techniques for treatment of AAA, such as in-situ fenestration of EVAR [99], prior to in-vivo testing. The proposed phantom will also be crucial for the development of novel US based

endovascular devices such as the in-situ fenestration catheter explored in Chapter 5.

3.1.2 Macro-scale vascular phantoms

Various methods are presented in the literature for creating vascular phantoms, including 'walled' and 'wall-less' phantoms. In walled phantoms, materials such as plastic tubing are used to create vessel structures [100][101]. In contrast, for a wall-less phantom, the material used to create the vessel structure is removed from the tissue mimicking material (TMM) once it has set, leaving a hollow space, through which fluids can be passed [102][103][104]. These wall-less phantoms are often preferred for imaging studies and simulating interventional procedures (such as EVAR), because the materials used in walled phantoms can result in high ultrasound attenuation coefficients that make them unsuitable for imaging at depth [105]. However, it is very challenging to create complex, anatomically realistic wall-less phantoms using current techniques. Published methods use plastic rods to create vascular structures, however, these need to be pulled out from the TMM, meaning that complex anatomical structures are precluded [106]. Alternatively, low melting point metals are cast into vessel shapes and then removed by melting then once the TMM has set [107][108][109], but this is a complex and expensive process. More recently, Ho et al. [110] used 3D printing to create wall-less phantoms for flow studies and external imaging, but the fabrication involves the use of chloroform, a highly toxic substance requiring careful handling. Casting of water soluble materials, such as isomalt, that are surrounded by TMM before being dissolved out, has yielded promising results [111], however it remains challenging to generate models of sufficient complexity. Poly(vinyl alcohol) (PVA), a water-soluble material typically used in 3D printing to provide support to overhanging structures, has shown promise in the fabrication of haemodynamic simulations [112][113], however to date has not been used to fabricate multimodality imaging phantoms. The properties that a phantom must possess depend on the proposed application. In the case here, of their use in developing new imaging technologies, phantoms must be suitable for imaging with a range of modalities and have realistic tissue-mimicking properties. It is also beneficial for phantoms to be created using real patient data,

so that they reflect the complexity of human vasculature. Ideally, phantoms must be hollow to allow devices and blood mimicking fluids to be passed through the vessels. IF requires fixed radiological landmarks visible on both imaging modalities used, such as the spine. Therefore inclusion radiological landmarks within the phantom is desirable.

3.1.3 Tissue-mimicking materials

Materials that exhibit properties that can mimic the imaging appearance and mechanical behaviours of biological structures are of significant importance to the performance and utility of phantom models. Other important considerations for these materials are cost, stability, shelf-life and toxicity. Specific to ultrasound imaging, multiple different TMMs have been trialled [114]. Among the most frequently utilised materials are silicones, a group of synthetic polymers. Although these tend to be mechanically robust and stable, the acoustic appearance is sub-optimal due to high levels of ultrasound attenuation [115]. Aqueous-based materials such as gelatin gel and agar are widely available and of low cost. Ultrasound properties can be altered through the addition of flour, cellulose powder, or psyllium husks [116][117], however gradual evaporation of water leads to material degradation and a resultant short shelf-life. Poly(vinyl alcohol) cryogel (PVA-c) is synthetic polymer solution. Through repeated alternating free-thaw cycles acoustic properties can be altered [118]. Preparation of these materials, however, is labour intensive and requires electronic stirring of the solution at 1800 rpm [113]. Additionally they are susceptible to degradation from both evaporation and bacterial contamination [119]. Gel-wax has recently emerged as a promising TMM and has been used to create heterogenous anatomical ultrasound tissue phantoms [120][121]. It is an insoluble, mineral-oil based material that is solid at room temperature. It has a low melting point of 70°C, above which it becomes highly mobile. Ultrasound properties can be tuned through the addition of glass spheres. Gel-wax offers several advantages compared to other TMMs such as Agar, PVA-C or silicone. Firstly, it is both mechanically and thermally stable; secondly, it has a low viscosity (30-330 mPa/s), facilitating integration into phantom models; lastly it is insoluble in water which fa-

cilitates generation of wall-less phantom models when using a water-soluble inner model.

3.1.4 Phantoms as training models

Endovascular intervention is often the preferred treatment option for complex AAA over an open surgical approach due to decreased patient recovery time and risk of wound complications [122]. Traditionally, surgical training has been undertaken on human and animal cadavers, before progression to supervised participation on patients. Endovascular aortic repair (EVAR) procedures are particularly challenging to learn due to the need for radiological familiarisation and the requirement for complex psychomotor skills to manipulate the endovascular devices. Furthermore, shortened post-graduate training programmes and increasing clinical commitments can limit the opportunities that trainees have to gain experience and competency with these procedures [123]. Phantom models are powerful tools for trainee surgeons learning to perform these procedures. They can provide both a realistic representation of patient anatomy and an opportunity to gain familiarity with surgical equipment and techniques, without risking harm to a patient. Multimodality imaging phantoms ideally have clinically-relevant anatomical structures that have realistic appearances on at least two imaging modalities. Simulation training on phantom models has been shown to result in decreased fluoroscopy and procedural times [124][27] as well as overall volume of contrast used [125], compared to traditional teaching methods. Additionally, patient-specific phantom models can be used in the pre-operative planning of interventions [126][127]. Current simulation tools include both virtual reality (VR) platforms and physical phantoms. Although VR training platforms have shown promising outcomes in EVAR, with decreased procedural time and post-procedure endoleaks observed [128], physical phantoms are also important tools for surgeons seeking to develop the complex motor skills required for EVAR procedures [129]. However, most commercially available models have many limitations. Currently, phantoms that are low-cost often tend to have a low level of anatomical accuracy and are not typically patient specific, which limits their use for surgical planning or in-depth training. Others that are more anatom-

ically realistic tend to be very expensive, and even those may only be compatible with one imaging modality. Many methods for creating AAA models in the literature include the use of high cost or difficult-to-source materials and techniques, such as resin printing, so they cannot readily be reproduced for clinical training. Additionally, most current phantoms include only the vessel structures [130] without surrounding tissues, so that their realism and use with multimodality imaging are limited. Image fusion (IF) is a technique where data from one imaging modality is combined with another to produce an overlay in real time. Within the field of vascular surgery, it has an increasing role in the endovascular treatment of complex aortic aneurysms, and therefore, it is important that EVAR training phantoms are designed to be compatible with IF. Using IF, pre-operative CT data can be overlaid onto intra-procedural fluoroscopic images, to facilitate fenestrated stent deployment [131][99]. This requires fixed radiological landmarks, such as the spine, to be visible on both imaging modalities used.

3.2 Aims

To validate a novel technique, based on 3D printing of vascular structures and inclusion of tissue-mimicking materials, for creating anatomically accurate vascular phantoms, which can be used with multiple complementary imaging modalities and allow simulation training. The vascular structures that were chosen for these phantoms were i) a Carotid Artery Phantom and ii) an Abdominal Aortic Aneurysm (AAA) Phantom.

3.3 Methods

3.3.1 Phantom fabrication

There are several key steps in the fabrication method presented, which are illustrated in Fig 3.1. Firstly, patient CT data is acquired allowing segmentation of areas of interest. Next, the segmentations are converted into models for 3D printing; the vasculature is then printed in a water-soluble material, whilst bone structures are printed in a non-water-soluble material. Finally, the phantom is constructed by

pouring the TMM over the 3D printed model. Once the TMM has set, the phantom is submerged in water to dissolve out the vascular structures, producing a hollow, or "wall-less" phantom.

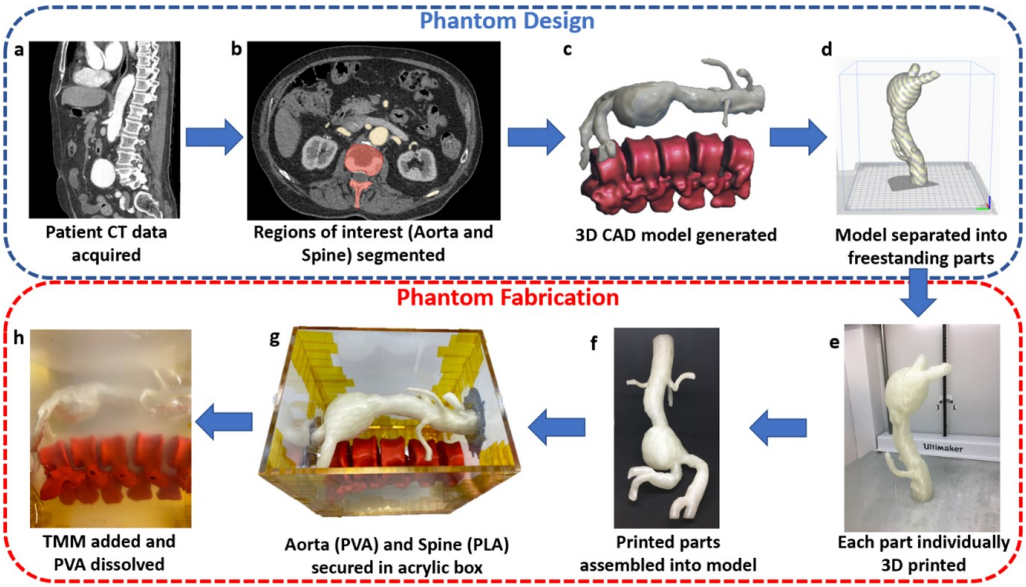

Figure 3.1: Fabrication overview - AAA phantom

a) Volumetric data is acquired from a patient CT scan and b) regions of interest from this data-set are manually segmented; c) these segments are then exported as 3D computer aided design models and the mesh is refined to create an STL file compatible with 3D printers; d) the models are orientated to negate the requirement for support material; e) large overhanging structures are separated and printed individually using PVA before f) assembly into the completed model; g) the printed Aorta and Spine are secured in an acrylic box with both ends of the PVA Aorta exposed; h) tissue mimicking material is integrated into the box and the inner PVA Aorta is dissolved out using water.

3.3.1.1 Model generation

For both models, volumetric patient-specific data was obtained from arterial phase contrast CT acquisitions (Fig 3.1.a). For the carotid phantom the source of data was an open source database (www.grabcad.com). The AAA phantom data was obtained from the Vascular department at the Royal Free Hospital London. The data set was fully anonymised and informed consent from the patient was obtained for use of the data-set in clinical research in accordance with the local research ethics policy. The data set was segmented manually, using an open source medical image analysis software platform (3D Slicer), according to vascular regions of interest (Fig

3.1.b). A 3D model of the segmented data was exported to Meshmixer (Autodesk Inc, San Rafael, Ca, USA) to allow for smoothing and refinement (Fig 3.1.c), before generation of an STL-file compatible with 3D extrusion printing software. Unsupported structures with an overhead angle to the base plate of greater than 70° were segmented into separate models, to prevent the requirement for support material during the printing process, before later amalgamation (Fig 3.1.d).

3.3.1.2 3D printing

The models were printed using a dual extrusion, commercially available 3D printer (Ultimaker S5, Ultimaker B.V., Utrecht, Netherlands) (Fig 3.1.e). The material used for printing was Poly(vinyl alcohol) (PVA) (RS components Ltd, Northants UK) which is a water soluble, non-toxic filament commonly used as a support material for 3D printing. Once printed, the separate segments were combined together to form the final model using PVA glue (Elmer's Products Inc, NC, USA), a water-soluble adhesive (Fig 3.1.f]). The models were secured in custom laser-cut acrylic open-topped boxes, with either end of the main vascular structure exposed (Fig 3.1.g). An additional insoluble spine, 3D printed using Polylactic acid (PLA), was included within the model. This provided an anatomical landmark, allowing for image fusion (IF) guidance techniques and facilitating benchtop endovascular procedures. These structures were manually positioned to give a close approximation of relative geometries.

3.3.1.3 Tissue-mimicking material

The gel-wax (Mindsets UK, Essex, UK) was heated,on a hot plate, to a temperature of 150°C for a period of 4 hours to ensure uniform consistency. Air removal was facilitated using a vacuum chamber before glass microspheres were added in a concentration of 0.5% for acoustic scattering. The mixture was sonicated for 5 minutes, to guarantee uniform particle distribution and achieve acoustic homogeneity. Following this the mixture was introduced into the acrylic open-topped box, allowing the gel-wax to surround the PVA aorta and PLA spine models, cooling into a solid state. Finally, the box was immersed in de-ionised water for 24 h. The exposed ends of the main vascular structure provided an entry point for the water resulting in the

dissolution of the PVA aorta, leaving behind a negative, wall-less vascular structure, surrounded by tissue-mimicking material (Fig 3.1.h).

3.3.2 Imaging

3.3.2.1 Transcutaneous ultrasound

Transcutaneous ultrasound imaging of both phantoms was obtained using a commercially available clinical system (HS40, Samsung Healthcare, Seoul, South Korea) with a curved array transducer probe (C2-8) operating with a frequency range of 2-6 MHz. The phantoms were submerged in water to remove acoustic shadowing from air.

3.3.2.2 Intravascular ultrasound

Intravascular ultrasound was performed using an intracoronary imaging system (Opticross, Boston Scientific, Marlborough, MA, USA) operating with a transducer frequency of 40 MHz. An 0.018-inch diameter coronary guidewire (Hi-Torque Balance Middleweight, Abbott Cardiovascular, MN, USA) was passed through the water-filled (temperature range 20 - 22°C) AAA phantom and fixed at either end. The imaging catheter was then loaded onto the coronary guidewire and positioned in the region of an iliac vessel. Images were acquired with an automated pullback speed of 1 mm/s.

3.3.2.3 Computerised tomography

CT acquisition was acquired using a 320-slice scanner (Aquillion One, Canon Medical Systems Corporation, Tochigi, Japan), with a CT angiography protocol (thickness 0.5 mm; 100 kV; rotation time 0.5 s; mA R 388). To provide realistic contrast enhancement for the vascular structures, the phantom was submerged in a mixture of water and Iodixanol (Visipaque, GE Healthcare, Chicago, Illinois, US), a water soluble, isosmolar, non-ionic, iodinated radiographic contrast agent.

3.3.3 EVAR simulation

The AAA phantom model was utilised as part of an EVAR training simulation. A surgical trainee, with no prior experience in EVAR but with 3 years general surgical

experience, was instructed on how to perform the procedure under fluoroscopic guidance with direction from a Consultant Vascular Surgeon. Local radiation safety measures were followed and all participants had lead-lined personal protective wear. The device used was an AAA endovascular bifurcated stent (Zenith Flex, Cook Medical, Bloomington, Il, USA) The entry site for the EVAR device was through the right iliac artery as this provided the least tortuous passage for the device.

3.4 Results

3.4.1 Carotid artery phantom

Fig 3.2 shows direct comparison of transcutaneous ultrasound imaging with computerised tomography imaging of the carotid artery phantom.

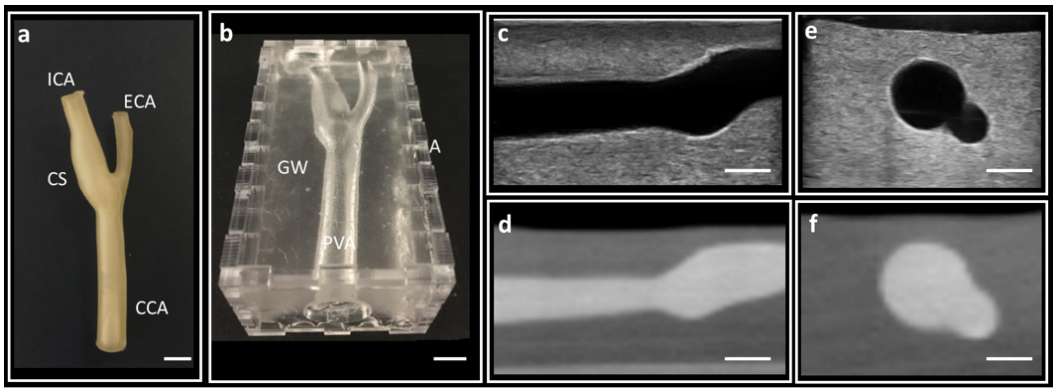

Figure 3.2: Imaging of Carotid Artery Phantom

a) 3D PVA print of the carotid artery. The common carotid artery (CCA) bifurcates into the internal (ICA) and external (ECA) carotid arteries. The carotid sinus (CS) is visible as an out-pouching of the ICA. b) The completed carotid artery phantom. The printed carotid artery (PVA) has been dissolved out of the gel-wax (GW) leaving a wall-less structure. The gel-wax is contained within an acrylic box (A). c) Transcutaneous ultrasound imaging of phantom displaying the longitudinal view with hyperechoeic homogenous signal from the TMM and a hypoechoic water filled vessel. d) Corresponding longitudinal view of computerised tomography imaging with iodinated contrast visible in the carotid artery. e) Transcutaneous ultrasound imaging of phantom displaying the axial view at the level of the internal and external carotid artery bifurcation. f) Corresponding computerised tomography imaging at the bifurcation level. The horizontal scale bar in all figures represents 5 mm.

3.4.2 Abdominal aortic aneurysm phantom

With transcutaneous ultrasound imaging various anatomical areas of interest were clearly delineated. The transcutaneous axial view (Fig 3.3.a) demonstrates the main aorta (A), renal (LR/RR), and superior mesenteric (SMA) arteries, visible as hypoechoic areas. The TMM appears as a homogenous hyperechoic medium surrounding these structures. In the longitudinal view (Fig 3.3.b) the abdominal aortic aneurysm sac (AAA) and neck are visible. Intravascular ultrasound of the phantom (Fig 3.3.c) demonstrates an echo-bright cylindrical structure consistent with the appearance of vascular endothelium, with underlying low attenuation material consistent with the appearance of adventitia. This comparison to in-vivo tissue was done qualitatively based on clinical experience and review by multiple vascular surgeons with expertise in intravascular imaging. This was deemed to be realistic based on the architecture, geometry and boundaries of the vessels included. d) is a intravascular ultrasound acquisition of a human carotid artery for comparison, displaying the expected appearance of the intima and adventitia [132]. An acoustic artefact generated by the coronary guidewire was apparent.

The CT acquisition of the phantom was compared to the original patient CT dataset from which the phantom was derived (Fig 3.4.). Three different radiological planes, at similar slices, are demonstrated; axial (Fig 3.4.a, Fig 3.4.b), sagittal (Fig 3.4.c, Fig 3.4.d) and coronal (Fig 3.4.e, Fig 3.4.f). In both acquisition sets, there is contrast clearly visible within the vascular structures, allowing delimitation from surrounding material. The aneurysmal sac of the complex abdominal aortic aneurysm (AAA) is seen in two orthogonal views (Fig 3.4.d, Fig 3.4.f), with orientation of visceral side branches, such as Iliacs (IL), Renals (RR/LR), Superior Mesenteric (SMA) and Coeliac (C), preserved. The PLA spine (S) included in the phantom model is visible as a radiopaque structure (Fig 3.4.b) and corresponds with the appearance of the spine from the patient's CT scan (Fig 3.4.a).

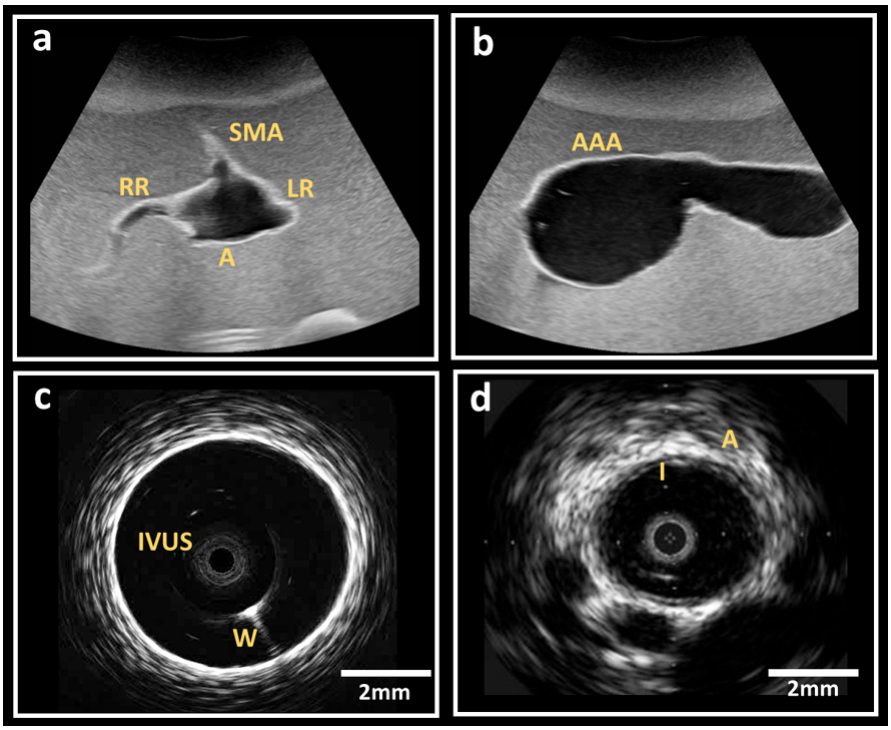

Figure 3.3: Ultrasound Imaging of AAA phantom

a) External ultrasound demonstrating an axial view of the Aorta (A) surrounded by an ultrasonically homogenous tissue mimicking material. Left (LR)/ Right (RR) Renal arteries and the Superior Mesenteric Artery (SMA) origins are visible. b) A longitudinal view demonstrating the Abdominal Aortic Aneurysm sac (AAA). c) Intravascular ultrasound with the imaging catheter (IVUS) located centrally within the lumen of the vessel. W represents acoustic artefact created by the coronary guidewire. d) Intravascular ultrasound of a human carotid for comparison [132]. The intima (I) and the adventitia (A) are displayed.

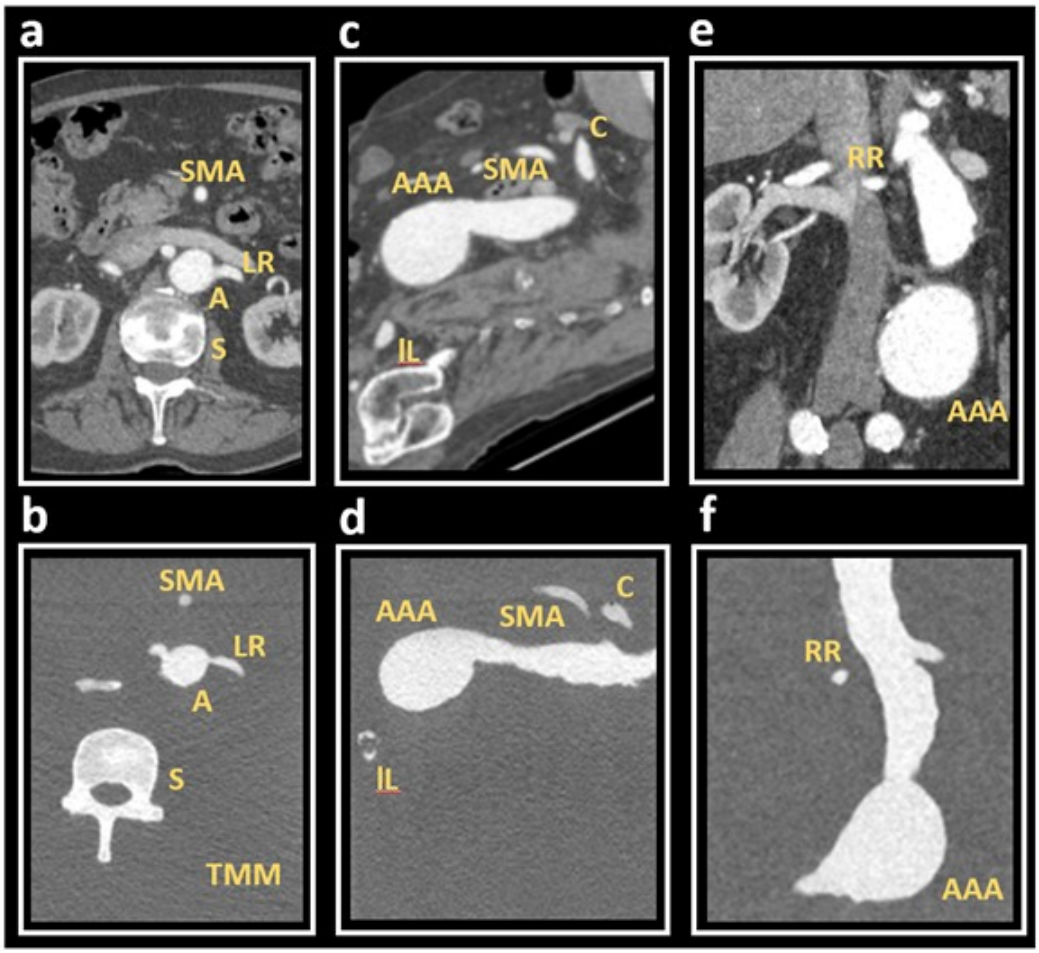

Figure 3.4: Comparison of CT from both the original patient data-set and the AAA phantom

a) Axial view of patient CT at the level of the renal artery bifurcation with the left renal artery (LR), spine (S) and aorta (A) demonstrated; b) Corresponding axial view from the phantom model CT demonstrating the same structures surrounded by tissue mimicking material (TMM); c) Sagittal view of patient CT demonstrating abdominal aortic aneurysm (AAA) sac, coeliac artery (C), superior mesenteric artery (SMA) and Iliac artery (IL) ; d) Corresponding sagittal view from the phantom model CT; e) Coronal view of patient CT demonstrating the abdominal aortic aneurysm (AAA) and right renal artery (RR); f) Corresponding coronal slice of phantom model CT

During the EVAR simulation the trainee successfully deployed the EVAR stent. Fig. 3.5.a demonstrates the insertion of the device catheter into the phantom. Fluoroscopy was used to confirm positioning of the device (Fig. 3.5.b).

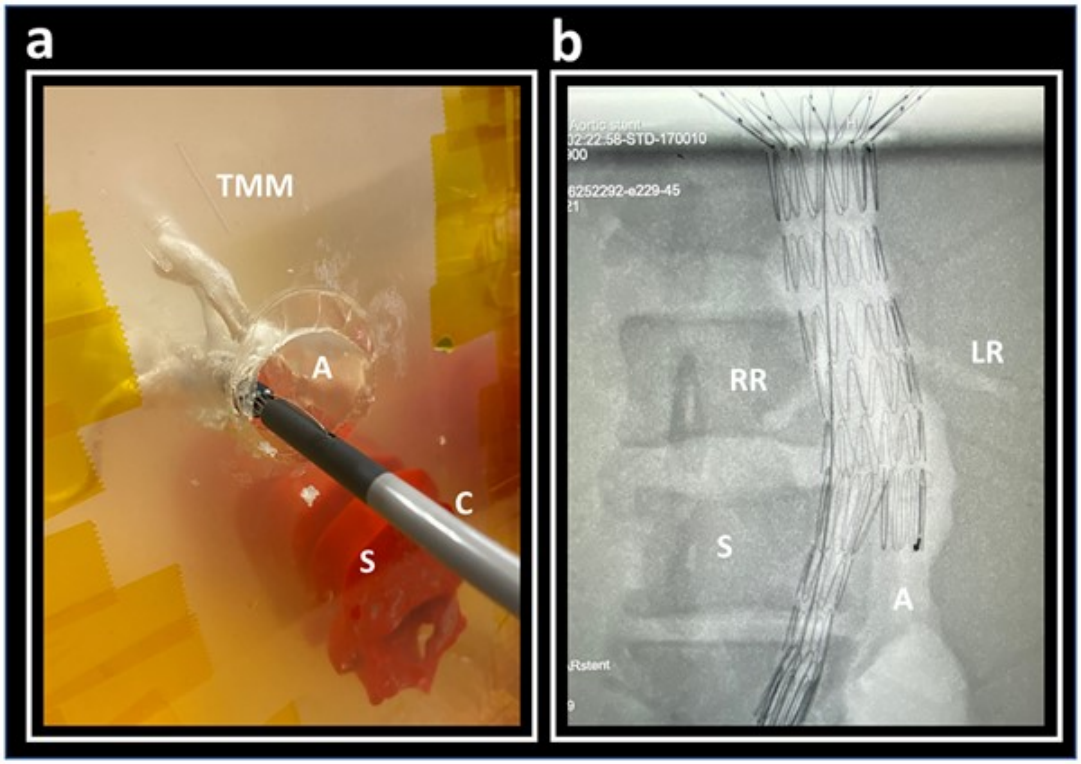

Figure 3.5: Simulated EVAR procedure

a) Insertion of catheter (C) into the Aorta (A) during the simulated EVAR procedure with the Spine (S) visible within the tissue mimicking material (TMM) ; b) Anterior-Posterior fluoroscopic view of the phantom model post EVAR stent deployment. The Spine (S) is visible as a hyperdense structure with the left renal artery (LR), right renal artery (RR) and Aorta (A) visible as hypodense structures.

3.5 Discussion

The method of fabrication that we have presented here can be used to create a high-fidelity patient specific vascular phantom of an AAA, compatible with both US and CT imaging. Current multimodality imaging phantoms that use materials such as silicone or plastics have unrealistic attenuation coefficients which can make them unsuitable for imaging at depths with techniques such as ultrasound [105]. Furthermore the rigidity of the material may not facilitate insertion of interventional devices for training. The novelty of this study stems from several factors. Firstly, the use of a 3D printed dissolvable complex AAA model embedded within TMM. Secondly, we have demonstrated the phantom's utility as a training tool during simulation of

an EVAR procedure. The materials used in the fabrication process are inexpensive, stable at room temperature and have no specific limitations on shelf-life. The use of 3D printed dissolvable models allows for complex geometries to be generated, which not achievable using current techniques. The inclusion of radiopaque landmarks within the model ensures compatibility with image fusion guidance techniques, which help facilitate detection of visceral side-branches during complex EVAR procedures [131]. A further advantage of this fabrication method is that the process of dissolving the printed structures out of the model leaves behind a hollow, wall-less vasculature. This then has a realistic ultrasound appearance, and does not have the highly reflective signals that are present using traditional silicone tubing or resin-based imaging phantoms. Whilst the fabricated AAA phantom model can be used in the simulation of EVAR procedures, other complex vascular structures, such as the coronary or cerebral vessels, can be recreated using the same method. This may allow fabrication of suitable phantoms for simulation of procedures relevant to trainee Interventional Cardiologists or Radiologists, provided accurate luminal casts can be made of small vessels. This would be dependant on the resolution capability of the printing system used (20 - 200 μm with a 0.4 mm nozzle on Ultimaker S5). The proximal diameters of coronary and cerebral vessels range from 3-5 mm diameter, however smaller distal vessels may not be realised using this fused filament fabrication technology. In addition to compatibility with transcutaneous ultrasound, the phantom model produces realistic imaging when IVUS is used. IVUS has a role in EVAR procedures allowing accurate sizing of vessels and reducing contrast volume [133]. IVUS is also frequently used to guide coronary and peripheral vascular angioplasty and therefore compatibility with this imaging modality broadens the applicability of this phantom.

Although the elasticity of the gel-wax based TMM facilitates insertion of devices into the model, deployment of the EVAR and then subsequent removal of the stent led to crack formation. This allowed a space for the CT contrast solution to track, reducing the qualitative appearance for subsequent experiments. Furthermore, the manual method of fixing the 3D printed structures within the acrylic

box may lead to geometrical inaccuracies in comparison to the original volumetric imaging. Additionally, it would be of interest in future work to perform quantitative comparison of the geometry and radiological characteristics with the source data.

The smallest vessel size fabricated in this model was the right renal artery (5 mm diameter), however depending on the resolution of the 3D printer system used, it may be possible to include vessels as small as 1 mm in diameter [113]. This would allow reproduction of complex arteriole vascular beds, such as those seen with arterio-venous malformations [134] if a good luminal model could be created. Indeed, the utility of dissolvable structures is not limited to recreation of vascular structures but can also potentially be used to simulate other hollow branching systems such as lymphatics, ureters or the biliary tree. Surrounding these structures with tissue mimicking material, cast in organ-specific shapes, could allow for realistic imaging phantoms for visceral organs such as the liver, kidney or prostate. The TMM used was specific to ultrasound imaging, however inclusion of alternative materials with differing imaging contrast could potentially allow for compatibility with further imaging modalities such as magnetic resonance imaging (MRI). Furthermore, the elastic properties of the tissue mimicking material used in this study can be altered by the addition of paraffin oil [120], allowing further tailoring of vascular phantoms for use with flow simulations in a wide range of clinical contexts [8].

3.6 Conclusion

Through a hybrid approach including 3D printing patient-specific vascular structures in water-soluble material, and integration of tissue mimicking materials, anatomically complex multimodality patient-specific imaging phantoms can be fabricated, which are of use in simulation training of EVAR.

Chapter 4

Optical Ultrasound: Ex-Vivo Vascular Imaging

The work of this chapter is based on my publications below:

1) **'Optically generated ultrasound for intracoronary imaging'**
Little CD, Colchester RJ, Noimark S, Manmathan G, Finlay MC, Desjardins AE, Rakhit RD (2020). *Frontiers in Cardiovascular Medicine*
https://doi.org/10.3389/fcvm.2020.525530 [135]

2) **'All-optical rotational scan ultrasound imaging'**
Colchester RJ, Little CD, Dwyer G, Noimark S, Alles EJ, Zhang EZ, Loder CD, Parkin I, Papakonstantinou I, Beard P, Finlay MC, Rakhit RD, Desjardins AE (2019). *Nature Scientific Reports*.
https://doi.org/10.1038/s41598-019-41970-z [136]

3) **'All-Optical Ultrasound: A new platform for intracoronary imaging'**
Little CD, Colchester RJ, Manmathan G, Rakhit RD, Desjardins AE (2020).
Journal of the American College of Cardiology.
https://doi.org/10.1016/S0735-1097(20)31975-6 [137]

4.1 Introduction

The paradigm of Optical Ultrasound, development of OpUS transducers and receivers is described in detail in Chapter 1.3 (General Introduction: Optical Ultrasound (OpUS)). In summary as opposed to the electronic paradigm of conventional IVUS, where US is generated through the use of piezoelectrics or CMUTS, with OpUS the US is generated and received using pulsed or modulated light. US generation is facilitated by engineered optically-absorbing nanocomposite materials coated onto the distal end of a multimode optical fibre. US reflections are detected by a miniaturised fibre-optic hydrophone, comprising a Fabry-P*é*rot cavity, and interrogated using interferometry techniques.

4.1.1 Previous work

4.1.1.1 Development of OpUS imaging probes

Although previous studies had demonstrated the OpUS paradigm [138][139], Colchester et al., were the first group to demonstrate the potential for OpUS to generate ultrasound pressures and bandwidths sufficient to allow high axial resolutions relevant to intravascular imaging [35]. In this study 105/125 μm and 200/220 μm core/cladding diameter multimode optical fibres, dip-coated with a carbon nanotube (CNT)-PDMS composite, were coupled to a 1064 nm pulsed laser light source. Delivering pulse energies of 3.6 μJ to the 105 μm core and 11.4 μJ to the 200 μ core fibres, fluence values of 41.6 mJ/cm^2 and 36.3 mJ/cm^2 respectively were achieved. Corresponding ultrasound pressures, at a distance of 2mm from the fibre surfaces, were recorded as 0.44 MPa (105 μm core) and 0.89 MPa (200 μm core). -6 dB bandwidths generated were 12 MHz and 15 MHz respectively. These fibre-optic transducers were then utilised to demonstrate the first OpUS ex-vivo imaging of an ovine left ventricle [140]. The nanocomposite material thickness in these studies was $\approx$20 μm. The thicker the nanocomposite coating the greater the attenuation of generated ultrasound [141], therefore minimizing the coating thickness is crucial to facilitate higher frequency imaging [38]. In a follow-on study by Noimark et al., a novel bilayer coating method, including a submicron-thick dense layer of func-

tionalised multiwalled carbon nanotubes (MWCNT) and PDMS integration, was proposed [40]. With this the efficiency of ultrasound transduction showed marked improvement, allowing generation of US pressures of 12.2 MPa , at a distance of 3 mm from the fibre tip, and a corresponding -6 dB bandwidth of 39.8 MHz, comparable to commercial electronic IVUS intracoronary imaging probes.

4.1.1.2 Ex-Vivo imaging

Using a 200 μm core multimode optical fibre, coated with the aforementioned MWCNT-PDMS composite, real-time OpUS ex-vivo imaging was performed on a segment of swine carotid artery. All 3 layers of the arterial structure (intima, media and adventitia) were identifiable. Other structures of interest that were identifiable included a lymph node, a vein and a vessel side-branch. Tissue was visualised to a depth of 7 mm from the probe. These results compared favourably with histological analysis. [142]

4.1.1.3 In-Vivo imaging

Finlay et al., provided the first demonstration of in-vivo intravascular OpUS imaging [45]. A 300 μm core multimode optical fibre, coated with the MWCNT-PDMS composite at the distal end, was paired with a FOH and integrated into a cardiac transeptal puncture needle (BRK Transseptal needle, Abbott Cardiovascular, Plymouth, MN, US). This device was inserted into the right atrium of an anaesthetised swine via femoral venous access. A pullback of the device was performed with continuous A-Line acquisition, demonstrating multiple cardiac structures with real time kinematics due to cardiac motion. Finally the device was used to locate the foramen ovale within the inter-atrial septum, facilitating direct guidance of a transeptal puncture, a step crucial to allow access to the left atrium during the ablative treatment of specific cardiac arrhythmia.

4.1.2 Gaps in literature

Despite the described advancements made in the field of intravascular OpUS, there remains two significant developments that have to date not been realised. Firstly, the ability of OpUS to detect the pathological hallmarks of atherosclerotic disease

has not been validated against existing intravascular imaging modalities. Secondly, intravascular OpUS imaging is currently performed using forward-viewing probes. Commercial intrasvascular IVUS/OCT probes employ side-viewing imaging to provide rotational pullbacks acquisitions. Development of a side-viewing OpUS probe would be a crucial step towards clinical translation of this technology.

4.2 Aims

To validate a forward-viewing OpUS imaging probe by imaging an atherosclerotic plaque and to develop a side-viewing OpUS imaging probe capable of performing rotational imaging within a vascular structure.

4.3 Method

4.3.1 Forward-viewing imaging

4.3.1.1 Probe fabrication

A multimode optical fibre of 400/440 μm core/cladding diameter (CeramOptec, Germany), was used as the light transmitter for the OpUS transducer. The distal 5 mm of polyimide coating (30 μm thickness) was stripped from this fibre, cleaned with ethanol, before manual cleaving with a tungsten blade. The cleaved distal surface was manually polished flat to create ensure uniformity. The transducer coating comprised an integrated MWCNT-PDMS composite [40], the preparation of which consisted of two steps. For the first MWCNTs (6–9 nm $\times$ 5 μm particle size, Sigma Aldrich, UK) were manually mixed with Xylene in a concentration of 14 mg/mL[1] and applied to the distal fibre surface. For the second step the fibre was dip-coated in a solution of PDMS (MED-1000, Polymer Systems Technology, UK) and Xylene (1:1 ratio) and allowed to cure for 24 hours. The OpUS transducer was paired with a FOH, comprising a 125 μm core single mode optical fibre tipped with a FP cavity. These fibres were secured together with heat shrink tubing (Nordson Medical, Minneapolis, MN, US) to form the OpUS imaging probe.

4.3.1.2 Ex-Vivo sample

An ex-vivo human aortic root sample was obtained from the Cardiac Transplantation team at Harefield Hospital, London, UK. This sample was unsuitable for transplantation due to preexisting infection with an unspecified pathogen. Local ethical approval for imaging and tissue characterization was obtained. The sample was frozen on site and transported to our group for imaging. After defrosting, the sample was carefully dissected and a 3 cm section of right coronary artery was retrieved, splayed longitudinally and then imaged (Figure 4.1a). Following imaging the sample was fixed in formalin solution, embedded in wax and then stained with haematoxylin and eosin. The slides were examined by Dr Michael Ashworth, clinical lead for Histolopathology at Great Ormand Street Hospital, London, UK.

4.3.1.3 Experimental setup

The tissue sample was secured to a cork board, with the portion of board underlying the imaged area removed. This was then submerged in de-gassed water before sequential imaging with OpUS, OCT and IVUS probes. De-gassing the water was performed to reduce attenuation artefact due to the presence of air bubbles. The OpUS probe was affixed to an automated 2-axis translation stage (Thorlabs Inc, Newton, NJ, USA) and longitudinal imaging was performed with a controlled pull-back and a linear scan pattern, at a distance of 2 mm from the tissue (Figure 4.1b). The image acquisition protocol, similar to previous studies, consisted of 600 lateral steps with a 50 μm step size [142][36]. The light source for the OpUS transducer was provided by a diode pumped Q-switched Nd:YAG laser (SPOT-10-500-1064, Elforlight, UK) with an operating wavelength of 1064 nm, pulse duration 2 ns, and repetition rate of 100 Hz. The FOH was interrogated using a continuous wave laser (Tunics T100S-HP CL, Yenista Optics, France) operating in the wavelength range 1500-1600 nm (Figure 4.1c). OpUS Images were created as concatenated A-lines and synthetic aperture imaging [142][36]. Further imaging of the sample was performed using commercial OCT (ILLUMIEN OPTIS IVOCT imaging system and Dragonfly Duo imaging catheter; Abbott Cardiovascular, Plymouth. MN, US) and IVUS (Opticross, Boston Scientific, Marlborough, MA, US) probes. These acqui-

sitions were post processed to generate a longitudinal reconstruction analogous to the forward-looking OpUS probe pullback.

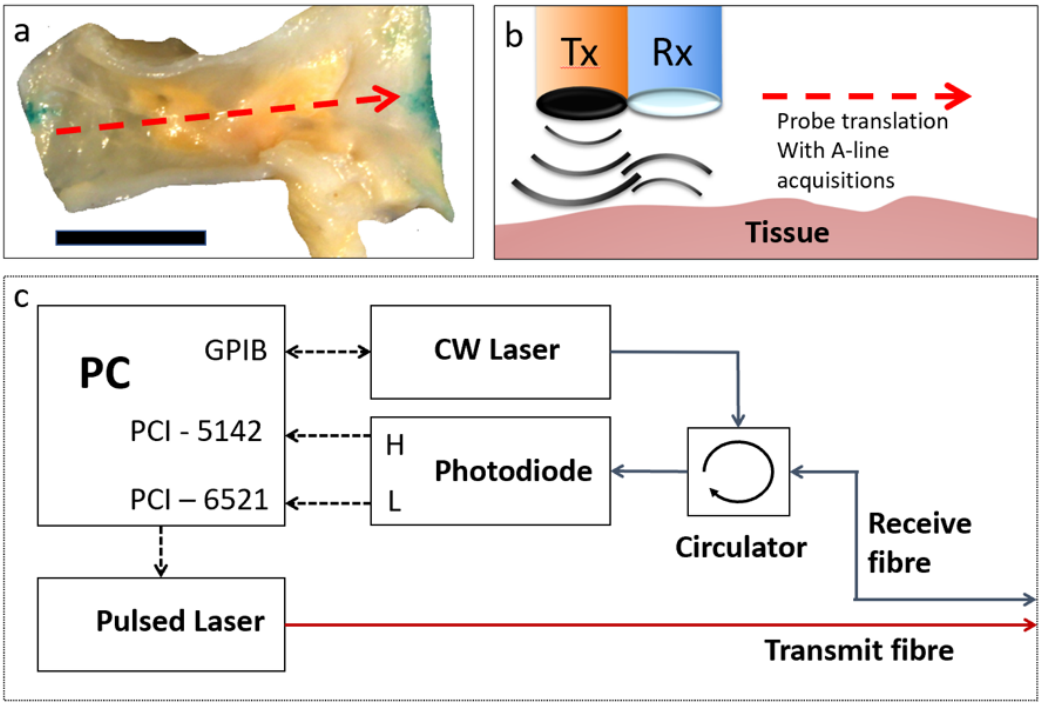

Figure 4.1: Setup for ex-vivo tissue imaging

a) Longitudinally splayed ex-vivo human right coronary artery. The dashed red line shows the direction of imaging. The black scale bar represents 1 cm. b) Representation of OpUS imaging: Tx is the OpUS transmitter and Rx is the FOH receiver. US is generated by the Tx and reflects off the tissue back to the Rx. This generates an A-line acquisition. The probe is translated in the direction of the red dashed arrow to create a 2D longitudinal image of the coronary artery surface. c) The custom made console used to perform the imaging consists of a pulsed laser source coupled to the OpUS transducer (Transmit fibre). US reflections are detected by the FOH (Receive fibre), which is interrogated using interferometry techniques by a CW laser. Peripheral component interconnector (PCI) units connect these external devices to the general purpose interface bus (GPIB), allowing remote control.

4.3.1.4 Post-processing

In addition to US reflections from tissue the FOH also detects US that is propagated directly from the OpUS transducer, generating cross-talk artefact. In order to optimise the image quality and reduce artefact the signal was post-processed prior to image reconstruction. For this a digital high-pass filter was utilised to remove excessive noise. Then a previously developed cross-talk removal algorithm was

applied to the signal to remove this artefact [142].

4.3.2 Side-viewing Imaging

4.3.2.1 Probe Fabrication

The OpUS transducer for the side-viewing probe consisted of a silica multi-mode optical fibre with core/cladding diameters of 400/440 μm (CeramOptec GmbH, Germany) and a 30 μm polyimide buffer coating thickness. The polyimide coating was removed from the distal 10 mm of fibre using warmed sulphuric acid. Subsequently, the tip was polished to a 45° angle using an optical fibre polishing unit (KrellTech, NJ, USA). The polished surface was covered with a silver paint (186–3600, RS Pro, UK) in order to reflect transmitted light perpendicular to the direction of initial transmission. After the paint had dried, a UV-curable epoxy cap (NOA81, Norland Products, UK) was affixed to the distal end (width × length × depth = 0.6 × 7.5 × 0.6 mm). Finally, the previously described MWCNT-PDMS coating was applied to the optically emitting side of the epoxy cap. The side-viewing OpUS transducer was inserted into a needle hypotube and paired with an omni-directional FOH using sealant wax (Figure 4.2). The performance of the transducer probe was evaluated prior to integration with the FOH and resolution characterised using a resolution phantom comprising parallel 27 μm diameter tungsten wires.

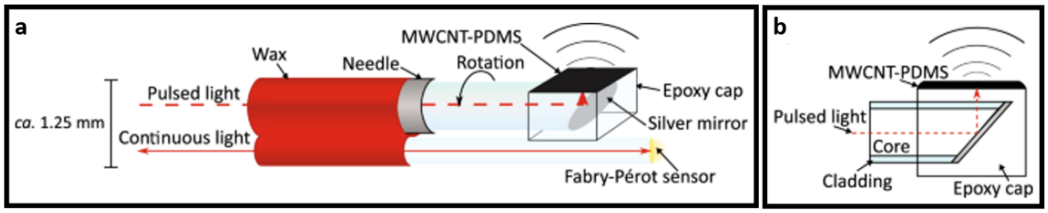

Figure 4.2: Side-viewing OpUS probe

a) Schematic of the side-viewing OpUS probe: The distal end of the transducer fibre is polished to a 45° angle and an epoxy cap is affixed. Pulsed light (dashed red line) is transmitted by the fibre and reflected by the silver mirror onto the transmitting surface of the epoxy cap. This is coated with a MWCNT-PDMS nanocomposite for OpUS generation. US reflections are detected by a FP sensor affixed to a single mode optical fibre, interrogated with continuous light (solid red line). The two fibres are fixed together with wax to create an imaging probe [136]. b) Magnified view of the distal portion of the transducer fibre demonstrating the reflected path of pulsed light (dashed red line) [136].

4.3.2.2 Device characterisation

Imaging resolution of the device was characterised using a wire phantom comprising multiple tungsten wires (27 μm outer diameter) arranged in series and suspended on custom built frame. Axial resolution was calculated using the full width of half the maximum point spread function of the acquired wire images. Furthermore, high-pass US frequency filtering was applied to these images to assess the relationship between US frequency and image resolution. 5 data samples were obtained for each separate high-pass frequency filter cut-off. These were then averaged to give a single value. Finally a depth-dependant frequency filter was applied to the received signal. For this the cut-off value of the high-pass US filter sequentially decreased in a linear fashion from 15 MHz at a depth of 0 mm from the probe surface to 1 MHz at 10 mm depth.

4.3.2.3 Experimental setup

A segment of swine carotid artery was used as the ex-vivo tissue sample for this experiment. This was obtained as a bi-product derived from healthy animals intended for human consumption, humanely slaughtered in EEC-approved abattoirs in accordance with EEC regulations (Medical Meat Supplies, London, UK). The sample was frozen for transportation after slaughter and then defrosted 1 hour prior to use to prevent cell degradation. The tissue was affixed to a custom built plastic frame and aligned with pre-drilled holes to allow for imaging probe intubation. The frame was submerged in de-gassed water prior to imaging. The previously described console (Figure 4.1c), used for the forward-viewing OpUS experiments, provided light for US transmission and signal interrogation. Rotation of the probe was facilitated using a custom built fibre-optic rotary junction (Princetel Inc, Hamilton, NJ, US) and a stepper motor (ST2818M1006-B, Nanotec Electronic GmbH, 85622 Feldkirchen, Germany). The acquired imaging signal was processed using a depth-dependent filter and cross-talk removal algorithm.

4.4 Results

4.4.1 Forward-viewing OpUS

Once fabricated, the forward-viewing OpUS probe had a lateral dimension of $<$ 700 μm. Characterisation of the transmitting fibre revealed a recorded US pressure of 1.36 MPa at 3 mm distance from the probe surface (Figure 4.3a), 21.5 MPa at the surface, and a corresponding -6 dB bandwidth of 39.8 MHz (Figure 4.3b), comparable to previous studies [40][142].

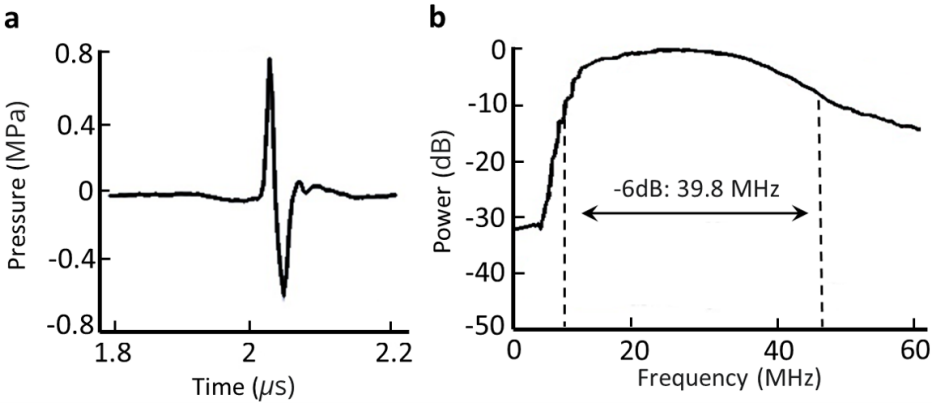

Figure 4.3: Forward-viewing OpUS probe characterisation

a) Transmitted ultrasound time series at 3mm from fibre surface. b) Corresponding ultrasound spectrum [40].

The reconstructed OpUS pullback demonstrated visible tissue structures at a distance of over 6 mm from the probe surface (Figure 4.4a). Below the tissue the appearance of a linear structure was consistent with the cork board that the tissue was affixed. An area of high attenuation was visible in the left third of the image (LP). This corresponded with the IVUS (Figure 4.4b) and OCT (Figure 4.4c) appearance of lipid infiltration. Histology confirmed the presence of a lipid pool in this region (Figure 4.4d). Additionally an area of high signal intensity was visible extending from the middle portion of the tissue to the right third (Ca). The IVUS acquisition showed a similar area of high reflectivity and histological analysis confirmed this to be an area of calcification.

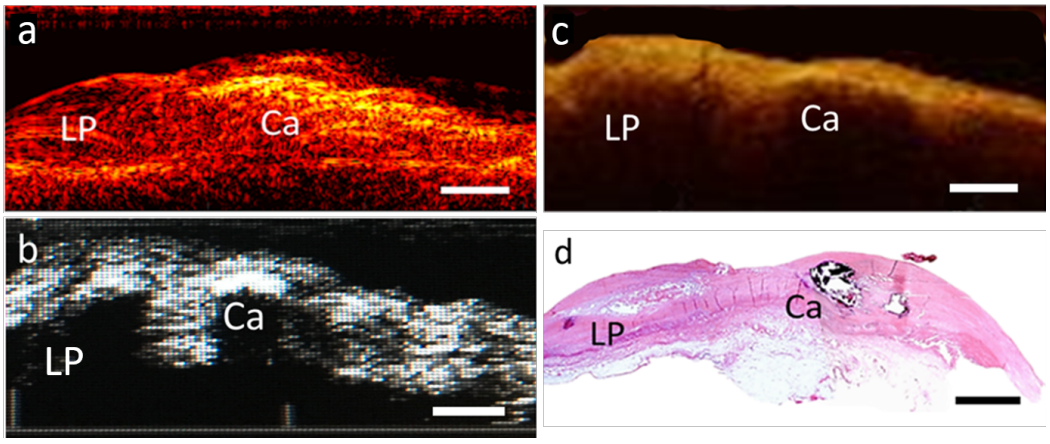

Figure 4.4: Comparison of OpUS with OCT/IVUS on Ex-Vivo human coronary artery

a) OpUS imaging of ex-vivo tissue with calcification (Ca) and lipid pool (LP) visible. b) Corresponding IVUS imaging, c) OCT imaging and d) Histology with haematoxylin and eosin staining. Scale bars represent 2 mm.

4.4.2 Side-viewing OpUS

The fabricated side-viewing probe had a lateral dimension of $<$1.25 mm. The recorded US pressure generated by the transducer was 1.87 MPa at a distance of 1.5 mm from the surface of the fibre (Figure 4.5a). The corresponding -6 dB US bandwidth achieved was 31.3 MHz, centred on a frequency of $\approx$20 MHz (Figure 4.5b). The US beam profile was highly collimated, with a full-width half-maximum angular divergence of 13°. With regards to the relationship between axial resolution and high pass frequency filtering, the greater the cut-off value of the filter the superior the image resolution obtained (Figure 4.5c). Increasing the high-pass frequency cut-off from 0.5 MHz to 20 MHz resulted in a corresponding improvement in average axial resolution obtained from 122 μm to 71 μm at a depth of 3 mm from the probe surface. Using the aforementioned depth-dependant frequency filter, an axial resolution of 54 μm was achieved at shallow depths ($<$3 mm). At a greater depth of 10.5 mm from the probe surface, the axial resolution was 59 μm.

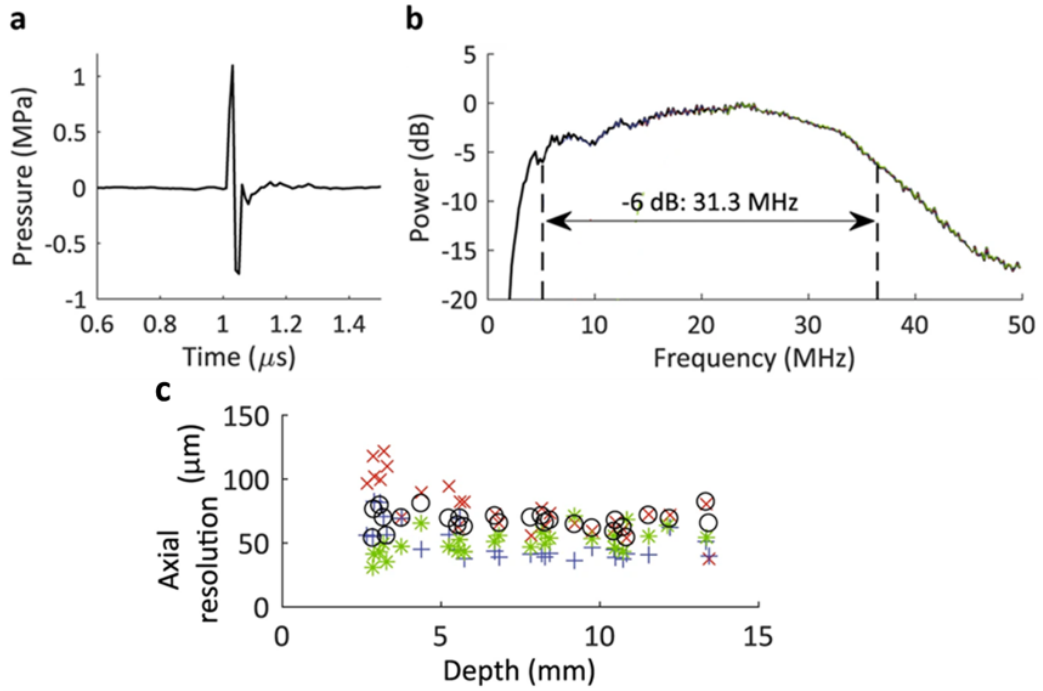

Figure 4.5: Side-viewing OpUS probe characterisation

a) OpUS probe transmitted ultrasound time series at 1.5mm from the fibre surface. b) Corresponding ultrasound spectra with a -6 dB US bandwidth of 31.3 MHz . c) Axial resolution achieved with varying high-pass frequency filter cut-offs (Red ×: 0.5 MHz; blue +: 10 MHz; green *: 20 MHz; black o: depth-dependent filter) [36].

The sample of ex-vivo swine carotid tissue was measured to have an inner luminal diameter of ≈4 mm. Following image acquisition, varying high-pass frequency filters were applied to the raw data to produce a reconstructed rotational image (Figure 4.6a-c). Although the inner luminal surface of the vessel was well visualised with all frequency filters, there was increased clarity of the endothelium as the cut-off of the high-pass frequency filter was increased. At high frequency filter cut-offs (i.e 20 MHz (Figure 4.6c)), deep tissue structures were no longer readily visible. Following application of the depth-dependant filter the luminal surface was well visualised with additional preservation of full vessel depth penetration (Figure 4.6d).

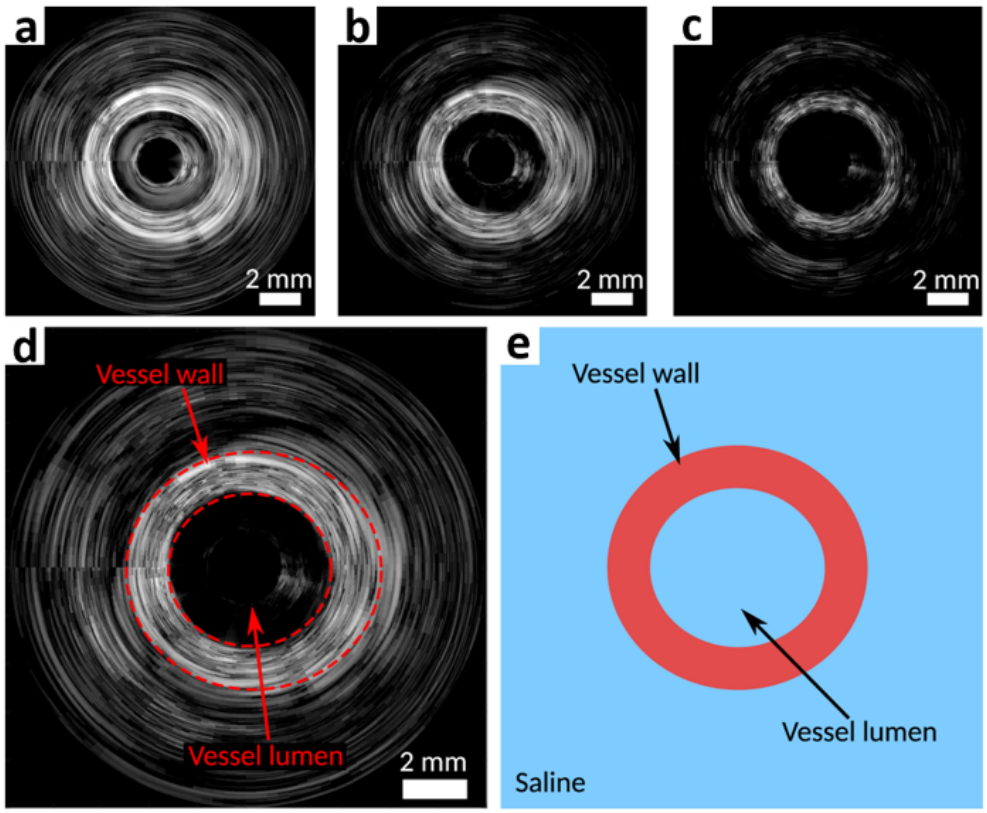

Figure 4.6: Side-Viewing OpUS imaging of Ex-Vivo tissue

Reconstructed rotational image acquisition with a) 0.5 MHz b) 10 MHz and c) 20 MHz high-pass frequency filter cut-offs applied. d) Reconstructed image with depth-dependant filter e) Corresponding vessel schematic [36].

4.5 Discussion

There are two key developments in the clinical translation of OpUS presented in this work. Firstly; validation of OpUS with diseased vascular tissue. Secondly; the development of a side-viewing imaging probe capable of performing rotational imaging akin to current intravascular imaging modalities.

Previously OpUS imaging of ex-vivo tissue has been performed [142], however the sample used in this study was derived from a healthy animal model. With increasing interest in the molecular characterisation of atherosclerotic disease, it is crucial to evaluate the capability of OpUS for identifying pathology. This study represents the first histological validation of OpUS intrasvascular imaging

using diseased human tissue. Furthermore a comparison to contemporary imaging modalities, widely used in clinical practise, is provided. With OpUS areas of tissue lipid infiltration and calcification within the coronary tissue were readily visible and corresponded to expected appearances on IVUS, OCT and histology. Whilst OCT provides superior imaging resolutions to OpUS, tissue penetration and assessment of calcium at depth are limited [143]. Figure 4.4c demonstrates that for OCT only the first 2mm of tissue are readily visible, with significant loss of signal at greater depths. OpUS demonstrated superior tissue penetration with tissue visible at over 6mm depth from the probe surface, comparable to IVUS. This depth of imaging offers the potential to facilitate accurate assessment of large diameter vessels such as the main stem of the left coronary artery. Additionally whereas OCT requires a blood-free field to acquire images, OpUS can be performed without injection of saline or contrast agents. This may increase the utility of this technology for patients with pre-existing renal impairment, in whom high contrast volumes can precipitate a contrast-induced nephropathy. Furthermore, OpUS can be readily combined with complementary imaging modalities, such as photoacoustic imaging, that may aid in molecular characterisation of atherosclerosis. This can be realised through the use of alternate nanocomposite transducer coatings that are optically absorbing at selective wavelengths but transmissive at others [34]. Speculatively, the inclusion of OCT as a complementary imaging modality within a hybrid catheter, could be achieved using a double-clad optical fibre. With this ultrasound reception and OCT imaging could be performed using a single-mode inner core for light transmission. Whereas light for OpUS generation could be transmitted with the multi-mode outer core. OpUS represents an exciting development in the field of intravascular imaging.

Through the inclusion of a reflective 45° angle at the distal fibre surface, side-viewing OpUS imaging has been demonstrated for the first time. When connected to a fibre-optic rotary junction, rotational B-mode imaging of a vascular structure can be performed. This offers the potential for appropriate luminal siz-

ing and assessment of vascular stenosis. Further modifications can be envisaged to optimise this device for in-vivo intravascular imaging. Firstly, typical clinical acquisitions employ an automated pullback to evaluate entire segments of vessel. For this a torque coil could enable rapid rotation in combination with a pullback motor. Secondly, integration of the probe into an over-the-wire catheter will provide added protection for the optical fibres and aid deliverability into potentially tortuous anatomy. The real-time frame rate for the acquisition was measured at 5 fps. Commercial IVUS catheters achieve frame rates of up to 30 fps [144]. The US transmitter used in this study can allow a pulse repetition rate of 8 KHz [36]. Predominantly the frame rate limitation of of OpUS is due to the time taken for data transfer and computation, rather than US generation. Therefore, in theory further refinements to the console could potentially increase imaging rates to over 100 fps, provided that there is adequate dissipation of heat generated by excitation light in the coating . An additional constraint is the time taken for ultrasound to propagate back and forth from the probe to the farthest depth for each A-line. However this is also the case with electronic IVUS probes.

OpUS image resolution is determined by both the US bandwidth generated (axial) and collimation of the US beam (lateral). High US frequencies allow superior axial resolution but at a cost of tissue depth penetration due to signal attenuation. Conversely lower US frequencies allow imaging of tissue at greater depths but with reduced axial resolution and a lower signal to noise ratio. The ideal intravascular imaging modality would allow high resolution imaging with deep tissue penetration. For this imaging with both high and low US frequencies are therefore desirable. The OpUS probes demonstrated in this work allow generation of broad US bandwidths (forward viewing probe -6dB 39.8 MHz and side-viewing probe -6dB 31.3 MHz). Through selective depth-dependant frequency filtering of the generated US we have demonstrated that it is possible to optimise image acquisition for both high resolution at shallow (54 μm at 3 mm) and greater depths (59 μm at 10.5 mm). This compares favourably with conventional 40 MHz IVUS catheters

(axial resolution $\sim$100 μm) and is comparable to new generation 60 MHz 'high-definition' IVUS technology (axial resolution 50 μm) [145]. OCT axial resolution remains superior (5-10 μm). Further improvements in image post-processing are possible. Methods for this include complex filtering and reconstruction, in addition to adaptive frequency filtering to allow differentiation between acoustically heterogenous tissues [34][146][147][148]. Several refinements to beam collimation, with subsequent improvement in lateral resolution, can also be envisaged. Firstly, employing a concave rather than flat transmitting surface may lead to a tighter beam focus [149]. Secondly, increasing the aperture of the transmitting fibre will allow for a less divergent beam. This however comes at a cost of increased device lateral dimension and reduced flexibility [149].

With regards to the manufacturing of the probes there is a degree of probe to probe variability for US generation. This may be due to variations in the nanocomposite thickness which are dependent on material viscosity and dipping speed. It would be of interest in future work to examine this variability and explore automated methods for fabrication. Furthermore, reproducibility of imaging was not assessed and this limitation should be the subject of further work and device characterisation. The comparison of OpUS to OCT and IVUS was performed qualitatively. Further quantitative assessment will be necessary, such as tissue component volumes or vessel sizing, to demonstrate non-inferiority to these alternative imaging modalities. As these experiments were performed ex-vivo, it is unclear what the effect of cardiac motion would have on the image quality. However, it can be foreseen that these challenges will be similar to those that have been experienced with IVUS, which have been overcome with high real-time frame rate. Methods for increasing the frame rate with OpUS have previously been discussed.

This work demonstrates the feasibility of OpUS form performing intravascular imaging. In addition to vascular imaging this technology may have further clinical applications for imaging additional luminal structures such as the biliary or endo-

bronchial tree. An absence of electronic components allows for MRI compatibility which may facilitate manipulation of the probe to regions of interest within these structures. Immunity to electromagnetic interference may be of benefit for guiding procedures such as radiofrequency ablations in real-time [150]. In the near future it can be envisaged that in-vivo intracoronary imaging of both healthy and diseased vessels will be performed using a purpose built over the wire imaging microcatheter. Continuing work on selectively absorbing optical coatings will enable hybrid imaging using both PA and NIRS during these studies. Further software development for image acquisition and processing will improve utility and facilitate broader clinical use.

4.6 Conclusion

OpUS can provide high resolution imaging of diseased vascular strutures comparable to other established imaging modalities. Furthermore, rotational OpUS imaging, facilitated through a side-viewing probe, is viable and paves the way for a future clinical device.

Chapter 5

Optical Ultrasound: Development of an Interventional Device

The work of this chapter is based on my publications below:

1) **'Flexible and directional fibre optic ultrasound transmitters using photostable dyes'**
Colchester RJ, Little CD, Alles E, Desjardins AE (2021). *OSA Continuum*
https://doi.org/10.1364/OSAC.431444 [1]

2) **'Dynamic physiological temperature and pressure sensing with phase-resolved low coherence interferometry'**
Coote JM, Alles EJ, Noimark S, Mosse S, Little CD, Loder CD, Rakhit RD, Finlay MC, Desjardins AE (2019). *Optics Express*
https://doi.org/10.1364/OE.27.005641 [2]

5.1 Introduction

5.1.1 Abdominal aortic aneurysm

An abdominal aortic aneurysm (AAA) is a persistent localized dilatation of the aorta, involving all three vascular layers (intima, media and adventitia), to more than 1.5 times the expected diameter [151]. Data derived from screening studies suggest a UK population prevalence of 1-2% of males over the age of 65 years [152]. Progressive expansion of the aneurysm may lead to rupture with resultant high mortality. Out of hospital ruptures have a quoted mortality of $\sim$50% prior to arriving in hospital and are thought to account for up to 5% of sudden unexpected deaths in the Western world [153]. As a result, screening and surveillance programmes have been recommended to allow timely intervention prior to significant risk of rupture [122] [154]. Current indications for intervention on unruptured aneurysms include those with a diameter of $>$5.5 cm or those $>$4 cm with an annual size increase of $>$1 cm [151].

5.1.2 Endovascular repair of AAA

Intervention options for the treatment of AAA include open surgery or endovascular repair (EVAR). EVAR is a minimally invasive procedure that involves the peripheral delivery of one or more covered endografts, to the aneurysmal segment, via a catheter-based system. Two landmark trials, published in 2004, demonstrated the superiority of this technique with regards to early mortality. The DREAM trial comprised a multi-centre RCT with 345 patients, with a AAA $>$5 cm, randomised to either open surgery or EVAR [155]. With respect to the primary outcome of 30 day all-cause mortality, EVAR appeared superior to open-surgery (1.2% v 4.6% (RR 3.9 0.9-32.9) p=0.1), although this did not reach statistical significance. Additionally EVAR was associated with shorter procedure time (median 120 mins vs 151 mins, p$<$0.001), less estimated blood loss (median 250 mls vs 1500 mls, p$<$0.001) and shorter hospital stay (median 4 days v 10 days, p$<$0.01) than open surgery. The larger EVAR 1 trial enrolled 1082 patients with a AAA $>$5.5 cm and randomised them to EVAR or open surgery in a 1:1 ratio. The 30-day mortality in the EVAR

group was 1·7% (9/531) versus 4·7% (24/516) in the open surgery group (odds ratio 0·35 [95% CI 0·16–0·77], p=0·009) [156]

5.1.3 Fenestrated endovascular repair of AAA

A particularly challenging group of patients to treat are those in which the aneurysmal sac extends proximally to include the origin of the renal +/- coeliac arteries. These are known as juxtarenal (JRAAA) or 'complex' AAAs and account for roughly 15% of all AAA [157]. With complex AAA repair it is of paramount importance to maintain the patency of major aortic sidebranches to allow for end-organ perfusion. Traditionally open surgery was preferred for these complex cases however with the advent of endografts with pre-made openings (fenestrations) in the graft material these patients can be treated using an endovascular approach known as a fenestrated endovascular repair of abdominal aortic aneurysm (FEVAR). To date there is a paucity of comparative outcome data comparing FEVAR to open surgery. No multi-centre RCTS have been performed. 5 year registry data, including 1742 patients undergoing treatment for complex AAA (535 FEVAR and 1207 open surgery), from the American College of Surgeons National Surgical Quality Improvement Program (NSQIP), demonstrated a significantly lower 30 day mortality for FEVAR (2.4% vs 4.7%; $p<0.2$) [158]. Additionally FEVAR was associated with less incidence of renal failure requiring dialysis (1.9% vs 6.4%; $p<0.0001$), fewer cardiac events (2.2% vs 5.8%; $p<0.001$), less major bleeding requiring transfusion (17.4% vs 50.2%; $p<0.0001$), and less requirement for re-intervention within 30 days (4.5% vs 9.6%; $p<0.0001$). The median length of hospital stay was also significantly shorter for patients undergoing FEVAR (2 days vs 7 days; $p<0.0001$). These findings of apparent real world superiority of FEVAR to open surgery come despite increased pre-procedural morbidity in the FEVAR patient population. Patients undergoing FEVAR had a higher prevalence of Diabetes Mellitus (15.5% vs 10.8%; $p<0.01$) and smoking (43.7% vs 30.5%; $p<0.0001$). They were older (median age 75 years vs 72 years; $p<0.0001$) and the percentage of patients defined as having a dependant functional status was greater (3.9% vs 1.6%; $p<0.002$). A major challenge to delivering FEVAR as a treatment option for complex AAA re-

pair is the device cost. A European centred cost calculation study demonstrated that the average total cost of a FEVAR procedure, excluding pre-operative planning and post-operative recovery, was $36,695 compared with $13,395 for a standard EVAR procedure [159]. This difference is predominantly driven by device cost. For FEVAR the options for industry manufactured devices consist of 'off-the-shelf' (OTS) endografts or custom made devices (CMDs). OTS endografts have pre-fenestrated holes that are suitable for most common anatomical configurations. Aortic aneurysms are however highly heterogenous and this is particularly true regarding the orientation of the renal arteries. CMDs are based on patient derived volumetric CT data and provide optimum conformity. This comes at an increased device cost and there are significant lead times for fabrication of these devices, potentially increasing the risk of a pre-procedural event. In terms of cost comparison an OTS endograft costs ∼£15,400, whereas a CMD is ∼£24,000 [159].

5.1.4 In-situ fenestration

The concept of in-situ fenestration (ISF) for endografts during FEVAR has been proposed as an alternative to the use of pre-fenestrated endografts. With this paradigm the fenestrations are generated at the time of the procedure. Potential benefits to this include both a greater anatomical conformity and reduced device cost. A non-fenestrated endograft costs ∼£6,000 [159]. Several methods have been proposed for generating fenestrations of which mechanical puncture and thermal ablation of stent material are the most prominent. Once ISF has been successful a wire is passed through the fenestration into the side-branch. The fenestration is then dilated with incrementally sized non-compliant or cutting balloons and secured with a stent that maintains communication between the aorta and side-branch [160].

5.1.4.1 Mechanical ISF

The first recorded ISF involved use of the stiff end of a coronary guidewire to puncture through endograft material into a subclavian artery [161]. Since this successful demonstration mechanical ISF, using a wide variety of devices, has been explored including biopsy [162][163], sub-intimal re-entry [164] and trans-septal puncture

needles [165]. The main limitation to these methods is that puncture and subsequent dilatation of the endograft material has a high incidence of fabric tear [166]. Additionally, the results vary significantly dependant on the endograft material used and the angle at which the needle makes the puncture [167]. Furthermore, significant force needs to be applied to the endograft material in order to generate a mechanical ISF, increasing the potential risk of damage to underlying vascular structures.

5.1.4.2 Thermal ablation ISF

Thermal ablation strategies for ISF are attractive as there is no specific requirement to exert penetrative force on the endograft material. Instead the material is vaporized through the use of either radiofrequency (RF) or laser probes. With RF ablation the endograft material is locally heated using a bipolar generator and a guidewire. Numan et al. provided the first in-vivo demonstration of this technique. The group used RF to generate ISF of a Valiant thoracic endovascular stent deployed in the aortic arch of a pig [168]. Subsequently several other studies have demonstrated the efficacy of RF ISF [160][169] . The largest case series of patients undergoing RF ISF during EVAR demonstrated technical success in 6 out of 10 planned cases. There were no ISF related complications and at 12 month follow-up of the successful procedures all fenestrations remained patent with no endoleak [169]. During this series only woven polyethylene terephthalate (PET) based endografts, such as Zenith Flex (Cook Medical, Bloomington, Il, USA) and Endurant (Medtronic, Ontario, Canada), were used. Attempts to create a fenestration on polytetrafluoroethylene (PTFE) based endografts, such as the Excluder (Gore,Flagstaff, Az, USA), were unsuccessful suggesting that this material may be resistant to the effects of RF. Additionally, contact with the metallic stent scaffold of the endograft during RF ISF can lead to device damage [169]. An alternative method for thermal ablation during ISF employs amplified optical energy from a laser source. The most widely used delivery system for this is a re-purposed Turbo Elite Laser Ablation Catheter (Spectranetics, Colorado Springs, CO, USA). This is a commercially available atherectomy catheter, used in the treatment of peripheral and coronary atherosclerosis. The light source is an Excimer laser system (CVX-300, Spectranet-

ics, Colorado Springs, CO, USA), employing a combination of noble and reactive gases, providing UV light with a wavelength of 308nm. The largest case series to date, using this device for ISF in 16 patients, demonstrated a 94% technical success rate with no major complications [170]. These devices tend to be bulky and are designed to be used in an over-the-wire delivery system, therefore are not optimized for use in this context. Furthermore the wavelength of light used is optimised for absorption by tissue and blood, a characteristic not required for ISF. Tissue absorption is minimised in the range of 600-900 nm [171] and therefore a laser source operating in this range is preferable. Recently an alternative method, using a laser diode operating with a wavelength of 808 nm, has been proposed for ISF by condino et al. [172]. The group demonstrated, on ex-vivo Human aortic tissue, that using this wavelength with a $\leq$ 250 ms irradiation time and power $\leq$ 4 W resulted in no histologically evident tissue damage (Hematoxylin and eosin staining) [173].

5.1.5 Intravascular imaging

The relatively large vessel diameters involved in AAA limits the choice of intravascular imaging to low frequency IVUS. A commercially available catheter (Philips Vision PV 0.035, Philips, Amsterdam, Netherlands), operating around a frequency of 10 MHz allowing 60mm imaging depths, is available for use during EVAR procedures. Data from a study by Pearce et al. suggested that routine adjunctive IVUS use resulted in decreased contrast volume and fluoroscopy time [174]. IVUS can also be useful in assessing the diameter of the aneurysmal neck, allowing post deployment balloon dilatation of the stent graft to an appropriate size, in order to reduce the risk of long term endoleak [98]. Additionally IVUS may have a role in assessing technical completion in FEVAR with incremental benefit when combined with plain angiography of visceral side-branch stents [175][176]. The main barriers to routine IVUS use appear to be device cost and learning curve required for interpretation of imaging.

5.1.6 OpUS imaging

Alles et al. have previously demonstrated the feasibility of OpUS to detect side-branches on an ex-vivo aortic sample [177]. In light of this OpUS is a potentially attractive option for guiding ISF for several reasons. The depth penetration achieved for OpUS (>1 cm) [135] is relevant to aneurysmal vessels and a blood-free environment is not required for image acquisition. The forward-viewing configuration of OpUS may offer direct visualisation beneath the endograft. This is important as it can allow side-branch detection and then subsequent appropriate ISF positioning, thereby maintaining side-branch patency. Lastly, the optical fibres used are of small diameter (<1 mm), highly flexible and could potentially offer an all-optical design whereby both imaging and ISF are provided using the same fibres. This offers benefits including reduction of device size, increased device flexibility/deliverability and reduced cost of the potential device.

5.1.7 Gaps in the evidence

To date there is no purpose made device that allows for direct imaging of aortic sidebranches with the added capability of achieving fenestration through an endograft. It is unclear whether the pressures generated with current OpUS technology are sufficient to visualise tissue through endograft material.

5.2 Aims

To develop and characterise a catheter-based device capable of imaging side-branches through an an endograft and generating in-situ fenestrations, thereby facilitating complex EVAR.

5.3 Methods

5.3.1 Device design

The design of the device prototype comprises 4 key elements, all of which are optical fibre components. These are 1) OpUS transducer, 2) fibre-optic hydrophone, 3) contact sensor and 4) ISF fibre. The paired transducer/hydrophone enables OpUS imaging to locate the side-branch. The ISF fibre delivers optical energy to the en-

dograft material to generate a thermal ablation. The contact sensor provides the operator with feedback regarding proximity of the catheter to the endograft material. Close contact of the ISF fibre with the graft may facilitate ISF by allowing the use of lower energy in order to minimise the risk of damage to surrounding tissues. These 4 fibres are secured together in a bundle using heatshrink material and housed within a 6Fr (2 mm ID) catheter (Multipurpose-1, Cordis, Santa Clara, CA, USA), leaving a 0.7 mm diameter channel to allow a 0.014 or 0.018 inch guidewire to be delivered through a generated fenestration. The catheter is delivered to the endovascular stent graft using a 7Fr ID steerable sheath (Tourguide, Medtronic, Minneaopolis, MN, USA). This device is inserted through the femoral artery over a 0.035 inch guide wire and positioned in the distal Aorta. It offers bi-directional 180°/90°deflection which is manually controlled by the operator. The steerable sheath allows the catheter to be appropriately positioned to detect side-branches underneath the endovascular stent. Figure 5.1 demonstrates the device design.

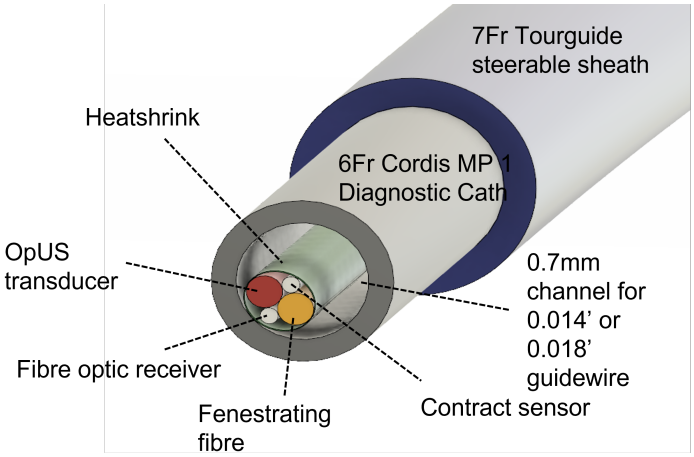

Figure 5.1: In-situ fenestration device design

The design consists of 4 optical fibres; i) OpUS transducer - 200 μm core multimode fibre spliced to a 400 μm core distal tip; ii) Fibre optic receiver with FP cavity on distal tip of 125 μm core single mode fibre; iii) Fenestrating fibre - 400 μm core multimode fibre; iv) Contact sensor - 200 μm core single mode fibre with epoxy dome on distal tip. These fibres are bundled together with heatshrink and housed within a Multipurpose 1 diagnostic coronary angiography catheter. The catheter is directed to target structures with a steerable sheath.

5.3.2 OpUS transducer

5.3.2.1 Design

With optical fibre transmitters there is an intrinsic trade-off between resolution and device physical flexibility. A general rule is that the greater the acoustic aperture of an optical fibre, the greater the resultant resolution of generated OpUS. Larger diameter optical fibres, however, are generally more rigid and have a greater bend radius. This limits utility in intravascular clinical applications where vessels can be tortuous, requiring devices that can navigate smoothly through tight bends. Furthermore, direct imaging of a side-branch to position an ISF requires the transducer to be facing a perpendicular axis to that of the main vessel. A solution to overcome these challenges would involve an OpUS transducer comprising a short segment of larger diameter fibre attached to a smaller diameter optical fibre body. The large acoustic aperture of this distal tip offers directional OpUS, whilst the small diameter body maintains device flexibility. To this end 3 separate OpUS transducer designs were compared: a monolithic 400 μm core diameter optical fibre, a 200 μm core fibre with a spliced 400 μm core fibre distal tip, and a 200 μm core fibre with a 400 μm core glass capillary distal tip. These OpUS transducer configurations are henceforth respectively referred to as ‘simple’, ‘spliced’, and ‘capillary’.

5.3.2.2 Fabrication

Figure 5.2 summarises the fabrication process for the three OpUS transducer configurations. For the simple configuration, the distal 1 cm of polyimide coating was stripped from a 400 μm core diameter optical fibre (WF 400/440/470P, CeramOptec, Germany). The minimum bend radius of this fibre was 22 mm. The exposed section of fibre was cleaned with ethanol to remove any residue, before manual cleaving with a tungsten blade to produce a uniformly flat distal tip. For the spliced configuration, the distal 1 cm of polyimide coating was stripped from a 200 μm core diameter optical fibre (WF 200/210/235 P, CeramOptec, Germany). The minimum bend radius of this fibre was 10.5 mm. This segment was cleaned with ethanol before the distal tip was cleaved using an automated cleaver (CT-101,

Fujikura, UK). A 400 μm optical fibre (WF 400/440/470P, CeramOptec, Germany) was stripped, cleaned and manually cleaved. The cleaved surface was then manually polished to a flat finish. The cleaved surfaces of both the 200 μm and 400 μm fibres were then spliced (90S+ Core Alignment Fusion Splicer, Fujikura, UK) to form a continuous but graduated fibre. Following successful splicing the 400 μm core diameter segment was then manually cleaved at a distance of 5 mm distal to the splice point, resulting in a 200 μm core diameter fibre body with a 5 mm long 400 μm core diameter fibre tip. The tip was then manually polished to ensure a uniform surface. For the capillary fibre a 200 μm core diameter optical fibre (WF 200/210/235 P, CeramOptec, Germany) was prepared by stripping the polyimide buffer cover from the distal 1 cm tip. This segment of fibre was then cleaned using ethanol before cleaving (CT-101, Fujikura, UK) to create a uniform distal surface. A 5 mm long segment of cylindrical glass capillary (ID: 400 μm, OD: 550 μm, CV405510, CM Scientific Ltd, UK) was manually cleaved using a tungsten blade. The inner cavity of the capillary was then filled with a high refractive index UV curing epoxy (NOA 1665, Norland, USA). This specific epoxy was chosen as the refractive index of 1.665 is higher than that of the glass capillary ($\approx$ 1.5). Therefore, assuming the capillary provides an optically smooth surface, light would be expected to stay within the capillary segment after exiting the distal fibre. Subsequently, the distal 2 mm tip of the prepared 200 μm core diameter optical fibre was inserted into the filled capillary before illumination under a UV source (wavelength: 365 nm, power: ca. 10 mW, M365FP1, Thorlabs, UK) for 5 minutes to ensure curing of the epoxy.

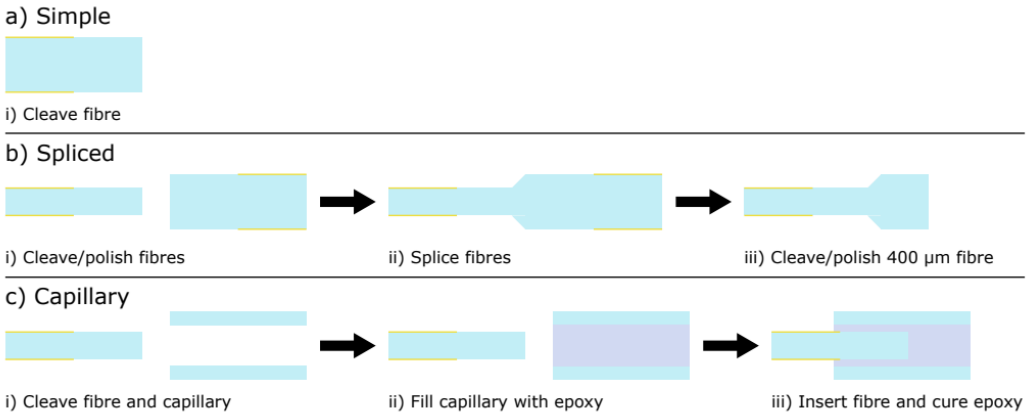

Figure 5.2: Fabrication of 'simple', 'spliced' and 'capillary' OpUS transducers [1]

Comparison of different fabrication methods for OpUS transducer. a) Simple fibre: i) a 400 μm core multimode optical fibre is cleaved and polished. b) Spliced fibre: i) 200 and 400 μm multimode optical fibres are cleaved and polished, ii) both fibres are then spliced together, iii) the 400 μm distal tip of the spliced fibre is cleaved and then polished. c) Capillary fibre: i) 200 μm multimode optical fibre and a 400 μm ID glass capillary section are cleaved, ii) the capillary is filled with a high refractive index epoxy, iii) the cleaved fibre tip is inserted into the capillary and the epoxy is cured with UV light.

5.3.2.3 Nanocomposite coating

All OpUS transducers were coated using both the same nanocomposite material and dip coating method. For the coating a dye-PDMS composite solution was prepared. This comprised of 10 mg of a near-infrared absorbing dye (Epolight 9837, Epolin, USA) mixed in 0.5 ml xylene and mechanically stirred until homogeneity was achieved. The solution was then combined with 250 mg of PDMS (MED-1000, Polymer Systems Technology, UK) and underwent further mechanical stirring. All transducers were manually dipped in this dye-PDMS solution. Following the dip coating the fibre tips were left upright and in ambient conditions for 24 hours to ensure curing.

5.3.2.4 Characterisation

All fabricated OpUS transducers were visually examined under a microscope and their optical absorption at a wavelength of 1064 nm was quantified. The US generated by the transducers was characterised using a needle hydrophone (Precision Acoustics, UK) with a calibration range of 1 to 30 MHz. During the characterisa-

tion the transducer being tested was coupled to a Q-switched Nd:YAG laser (Spot 10-500-1064, Elforlight, UK) to enable US generation. The technical settings assigned to this laser were a 2 ns pulse width, 100 Hz repetition rate and 20.1 μJ pulse energy. The hydrophone was raster scanned over a grid perpendicular to axis of the optical fibre to determine the ultrasound field generated. The grid size of the raster scan was 3 × 3 mm with uniform steps in the translation of the hydrophone of 50 μm. The hydrophone itself was positioned at a distance of 1.5 mm from the distal tip of the OpUS transducer being characterised under test.

5.3.2.5 Imaging endograft material

Frozen ex-vivo swine aorta (Medical Meat Supplies, London, UK) was obtained for the purposes of performing OpUS imaging with the fabricated probes. The sample was defrosted for 12 hrs at room temperature. The vessel was then longitudinally splayed open to create a flat surface. The specimen was secured to a cork board, with drawing pins. A portion of an endograft stent material (Zenith Flex®AAA, Cook Medical, Bloomington, IN, USA) made from a synthetic polyester Dacron material (DM) (polyethylene terephthalate) was separated from its stainless steel scaffold. This enabled the DM to be secured appropriately and placed over the ex-vivo swine aortic tissue. The sample was then immersed in de-ionised water. Similar to previous OpUS imaging studies, the acquisition protocol consisted of 600 lateral steps with a 50 μm step size [142][36]. The light source for the OpUS transducer was provided by a diode pumped Q-switched Nd:YAG laser (SPOT-10-500-1064, Elforlight, UK) with an operating wavelength of 1064 nm, pulse duration 2 ns, and repetition rate of 100 Hz. The FOH was interrogated using a continuous wave laser (Tunics T100S-HP CL, Yenista Optics, France) operating in the wavelength range 1500-1600 nm.

5.3.3 Contact sensor

Work by Condino et al. [172] demonstrated that one of the determinants of a successful fenestration is distance from the tip of the laser fibre to the stent graft material. This may be due to optical absorption and subsequent heat dissipation by

blood. When the fibre was in contact with graft material both a lower power (3 W) and lower pulse duration (0.5 s) were required to generate a reproducible fenestration. Whilst there is a degree of tactile feedback for the operator through manipulation of the optical fibre, a contact sensor integrated into the distal tip of the catheter would conceivably add confirmation to fibre positioning and reduce the requirement for fluoroscopic guidance and subsequent ionising radiation exposure. Fibre-optic pressure sensors are most commonly based on fibre Bragg gratings [178] and FP cavities [179]. With these, fabrication techniques can be complex resulting in increased manufacturing costs. Coote et al. demonstrated a novel method for fabricating dual pressure and temperature sensors on the distal tip of single mode optical fibres [2][180]. With this a low-finesse optical cavity, generated through the deposition of a PDMS dome on the fibre tip, is interrogated continuously using interferometric techniques. As a result subtle deformations in the dome, due to pressure changes, can be detected.

5.3.3.1 Sensor fabrication

The design of the contact sensor consisted of 2 parts, the optical fibre and the deformable dome, located on the distal fibre tip. The fibre used was a 0,22 NA single mode 200 μm silica core with a 235 μm diameter polyimide coating (136020003LV, CeramOptec GmbH, Germany). The polyimide buffer was stripped from the distal 10 mm of fibre and the tip was cleaved in the perpendicular plane (CT-101, Fujikura, UK). A second cleaved optical fibre was dipped into the sensor dome material, collecting a droplet on its tip. Using a 3-axis translation stage, under direct visualization with optical microscopy, the both fibres were aligned. When the two fibre tips contacted each other, a droplet of the material from the second fibre transferred to the sensor fibre, forming a dome which was then cured. Two different materials, with contrasting mechanical properties, were proposed for the dome; PDMS (734, Dow Corning, Midland, MI, USA) and a UV-curing Epoxy (Norland Optical Adhesive 81, Norland Products Inc, Cranbury, NJ, USA). The mechanical properties of these materials are summarized in Table 5.1. The Epoxy dome was cured under a UV-light source (wavelength: 365 nm, power: ca. 10 mW, M365FP1, Thorlabs,

UK) for 5 minutes.The PDMS dome was cured in 24 hour ambient conditions.

Material	Viscocity at 25°C (mPa)	Durometer hardness	Tensile strength (MPa)	Youngs Modulus (MPsi) (%)
PDMS	45,000	Shore A (27)	1.5	19 - 27
Norland 81	300	Shore D (90)	13.7	0.2

Table 5.1: Mechanical properties of dome materials

5.3.3.2 Sensor interrogation

For both fabricated sensors the optical fibre component was affixed, in the parallel plane, to an automated translation stage using a polyimide film non-residue tape (Kapton tape, Dupont, Wilmington, DE, US). The distal fibre tip , complete with deformable dome, protruded 5 mm from the end of the translation stage. A segment of splayed stent graft material (Zenith Flex, Cook Medical, Bloomington, Il, USA) was positioned in a perpendicular plane 10 mm from the contact sensor. The sensor was advanced in 0.25 mm steps under direct visualisation with an optical microscope.

In theory light travelling along the optical fibre will be partially reflected at interfaces where a refractive index differential is present. In the contact sensor design this occurs at two points. The first is the interface between the glass fibre and the dome (Z^1). The second is the interface between the dome and the outside environment (Z^2). The difference between these surfaces can be expressed as $Z^2 - Z^1 = \Delta$ Z. When the dome comes into contact with a surface Z^1 remains fixed but Z^2 is decreased leading to a change in Δ Z. These changes in Δ Z can be analyzed using phase-resolved low coherence interferometry (LCI) with a self-referenced fibre-optic Michelson interferometer. The spectra of the two reflected signals (Z^1 and Z^2) is measured by the spectrometer and an inverse Fourier transformation of the pattern of interference between these two spectra allows the amplitude peak corresponding to Z^2 to be plotted with with regards to distance from Z^1 and therefore

Δ Z to be calculated. Changes in the phase of light returning to the spectrometer can be tracked against time. Figure 5.3 shows the schematic used to interrogate the contact sensors. A superluminescent light emitting diode (SLED) with a central wavelength of 830 nm operating at an output power of 15 mW (BLM-S-820-B-I-10, Superlum, Cork, Ireland) was connected to an input branch of a 50:50 fibre-optic splitter (TW850R5A2, Thorlabs, Newton, NJ, USA). A compact broadband spectrometer (Flame-S, Ocean Optics, London, UK) was connected to the second input branch. This spectrometer had an acquisition time of 1 ms. The contact sensor fibre was connected to one of the output branches of the splitter, whilst the other output branch was redundant. An in-line attenuator (VOA-850-APC, Thorlabs, Newton, NJ, USA) was placed between the splitter and the SLED To prevent the spectrometer becoming saturated. The data acquired was analyzed in LabVIEW (National Instruments, Austin, TX, USA).

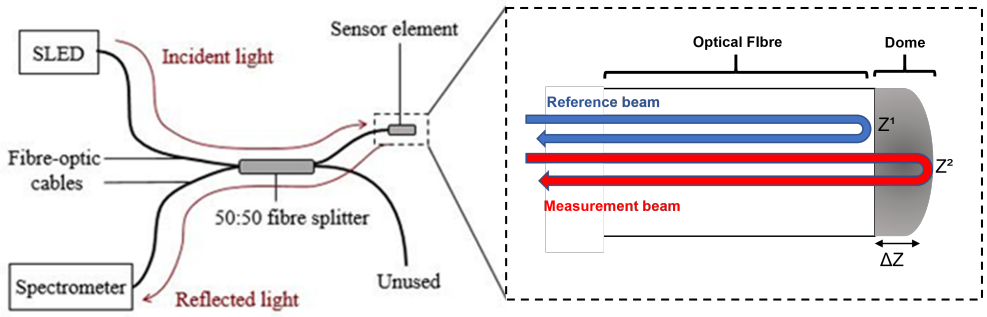

Figure 5.3: Contact sensor schematic [2]

Light from a SLED source reflects off the distal fibre tip (Z^1) and the interface between the deformable dome and environment (Z^2). Reflected light is interrogated using interferometric techniques. During contact between the dome and an object Z^1 remains constant and provides a reference. Z^2 changes and therefore dynamic differences between the interference peaks detected by the spectrometer can be used to determine contact.

5.3.4 Fenestration

A custom designed scaffold, 3D printed in PLA, was placed over a section of porcine loin tissue. The scaffold contained 16 cells each measuring 5 x 5 mm, allowing exposure to the tissue underneath. A section of endograft material (Zenith Flex, Cook Medical, Bloomington, Il, USA) was secured to the top of the PLA stand,

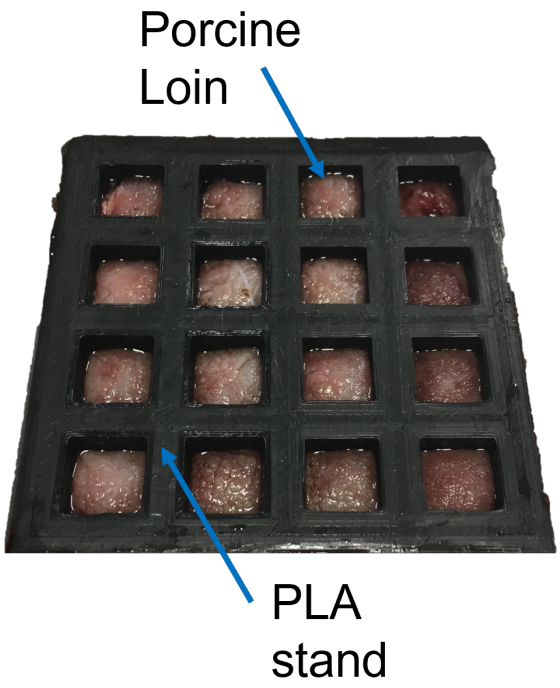

Figure 5.4: Fenestration Setup

The 3D printed PLA stand rests on top of the porcine loin tissue. With this there are 16 cells containing exposed tissue. The Dacron material is then secured to stand before immersion in blood. Each cell represents an area in which fenestration is attempted.

covering the cells. The distance from the stent graft material to the porcine tissue was ≈ 2 mm. The stand was immersed in warmed anticoagulated sheep blood (TCS Biosciences, Buckingham, UK). The light source was provided by a laser diode operating at 810 nm (Diomed D15 Diode, Diomed Holdings, Andover, MA, USA). The light was delivered to the stent graft material using a freshly cleaved multimode 400 μm core diameter optical fibre (CeramOptec GmbH, Germany), which was fixed to a 3-axis manual translation stage. The bare fibre tip was lowered into each cell until visible contact was made with the stent graft material. Parameters including pulse energy, pulse duration and distance from the stent graft material were varied. A fenestration was deemed to have been successfully achieved if tissue was visible underneath the stent graft material.

5.3.5 Device fabrication

The distal tips of the OpUS transducer, OpUS receiver, contact sensor and fenestration fibre were secured together using sealing wax. This wax has a melting point of 62-65 °C. Under direct visualization of an optical microscope the sealing wax was painted onto the fibres with a hot soldering iron. When cooled the sealing wax secured the fibres together in a bundle. This was further reinforced using heatshrink material (Nordson Medical Corporation, Marlborough, MA, USA), applied to the length of the fibre bundle, completing the device probe. The probe was inserted into a 6Fr multipurpose diagnostic coronary angiography catheter.A hydrostatic valve was placed at the proximal end of the catheter to prevent peri-procedural blood loss. Movement of the probe through this valve was facilitated by a segment of hypotube. The probe was secured to the inside of the hypotube with epoxy. The optical fibres remained bundled within flexible PVC tubing for a length of 1 metre before splinting into constituent fibres. These fibres then connect to various components within the console. The console has been previously described in Figure 4.1.

5.3.6 In-Vivo swine model

Following successful fabrication and pre-clinical testing of the device, multiple further devices were fabricated. These were used in two separate in-vivo experiments, in-vivo 1 and in-vivo 2. The animal model chosen for these was healthy swine (70kg Female Large white/Landrace crossbred pig). This was chosen as the vascular anatomy of a pig is similar to that of human, albeit with reduced dimensions throughout. The aortic diameter of this swine model ranges between 7 - 10.1 mm [181] (healthy human 20 - 30 mm [182]) and the external iliac artery between 6 - 6.8 mm [181] (healthy human 17 - 24 mm).

5.3.6.1 Ethics

The UK Home Office controls scientific procedures on animals in the UK and does so by the issue of licences under the Animal (Scientific Procedures) Act 1986. The regulations conform to the European Convention for the Protection of Vertebrate

Animals Used for Experimental and Other Scientific Purposes (Strasbourg, Council of Europe), and achieves the standard of care required by the US Department of Health and Human Services Guide for the Care and the Use of Laboratory Animals. The Home Office Project Licence governing this study (Project Licence - PPL: P14B07C34; Protocol Number: 1) directly specifies the limits of severity of effects on the animals. No formal claim of Good Laboratory Practice (GLP) compliance is made. The study was conducted in accordance with the standards of the Test Facility. The protocol for this study was reviewed and ratified by the local animal welfare ethical review board (AWERB).

5.3.6.2 Procedure

The full protocol for the experiments is described in Appendix A.

Following successful anaesthesia of the test subject, in both in-vivo experiments, transcutaneous US was used to gain percutaneous access to both common femoral arteries. 8 Fr vascular sheaths were inserted bilaterally. A 5 Fr pigtail catheter was then inserted into the Ascending Aorta via the RFA. An iodine-based contrast agent (Omnipaque 300, GE Healthcare, London, UK) was delivered, using a power contrast injector, with a total volume of 40 mls at a rate of 20 mls per second. Both fluoroscopic acquisition and digital subtraction angiography was performed, in order to create a road-map for further stages of the experiment. This process was repeated at the Aortic arch, Renal artery level, and Iliac bifurcation. The ISF device was inserted via the RFA and directed, with the steerable catheter, towards the origin of the RCA. The inner catheter of the ISF device was advanced into the proximal portion of the RCA and OpUS imaging was performed. The device was withdrawn from the RCA and directed towards the Aortic valve and OpUS imaging of the Aortic valve was then performed. Following this the device was withdrawn to the Aortic arch and an OpUS imaging pullback was performed across the left subclavian artery origin.

For the EVAR procedure a non-fenestrated iliac endograft was used (Zenith Spiral-Z, Cook Medical, Bloomington, IN, USA). The dimensions of this were 13

mm proximal diameter, 11 mm distal diameter and 129 mm in length. The RFA sheath was up-sized to a 14Fr in order to accommodate the delivery system. For in-vivo 1 the stent was deployed from the Aorta into the right external iliac. For in-vivo 2 the stent was deployed across the renal artery bifurcation. For In-vivo 1 the ISF device was inserted through the contralateral side (LFA) and OpUS imaging was performed with a longitudinal pullback from the left external iliac artery across the stented Aorta. For In-vivo 2 the ISF device was inserted into the stent through the ipsilateral side (RFA) and OpUS imaging was performed with a longitudinal pullback across the stented renal artery. Once positioned over the desired location a single pulse from the 808 nm laser (4.2 W and 5 second pulse duration) was delivered to the endograft to create a fenestration. A 0.018 inch diameter coronary wire (Balanced Middleweight Universal, Abbott, Abbott Park, Il, USA) was then inserted through the ISF device and through the fenestration into the side-branch. Ballooning of the fenestration was then performed with a 2 mm non-compliant, 3 mm non-compliant and 3mm cutting balloon in order to create a fenestration large enough to accommodate a stent. Following successful ISF the procedure was ended and the ISF device was removed.

5.3.6.3 Histology

After termination of the subjects vascular regions of interest were dissected out post-mortem. These included the aortic sections in the vicinity of the ISF procedures and four sections of healthy unaffected aorta from above the renal bifurcation (two from each in-vivo). Samples E + F were from the first in-vivo experiment and samples G + H were from the second in-vivo experiment. Two of the healthy sections (A + D) were used as the healthy control for histology. The other two healthy sections (B + C) were subjected to ablative energy from the ISF device on the benchtop and used as the diseased control. Each sample was trimmed longitudinally in as many thin strips of approximately 0.5mm as feasible, which were processed for histology and placed sideways to include all the layers of the organ (i.e. intima, media, and adventitia). The number of longitudinal sections per sample of aorta ranged from 4 to 6. Focal thermal ablation injury is expected to induce focal protein coagulation

that will involve both the elastin and the collagen of the vascular wall. These lesions may or may not be coupled with tissue loss. To examine for tissue damage each section was stained with both Haematoxylin & Eosin and elastin Van Giesson. The slides were prepared and examined by a histopathologist blinded to the source of each sample.

5.4 Results

5.4.1 OpUS transducers

Following successful nanocomposite dip coating, the three transducer configurations were examined and characterised. Optical microscopy revealed smooth and uniform surfaces (Figure 5.5). Furthermore, at a wavelength of 1064 nm, the optical absorption for all coatings was $> 95\%$, comparable with previous experiments [40].

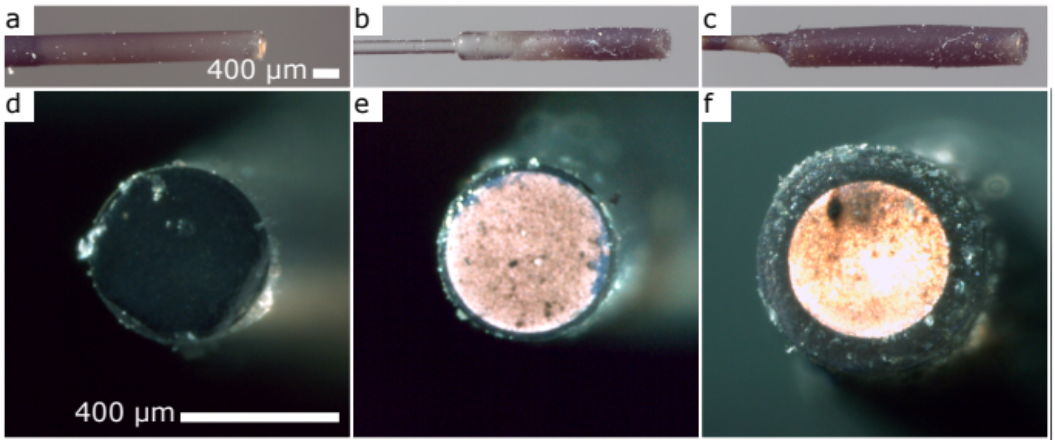

Figure 5.5: Microscopy of the three OpUS transducer configurations

The side-on view of the a) simple, b) spliced and c) capillary OpUS transducers configurations respectively. The corresponding face-on view of these transducers is shown in d), e) (with illumination) and f) (with illumination).

Table 5.2 displays the generated US characteristics for the three configurations. Measured US pressure for the simple, spliced and capillary device were 2.70, 2.69, and 2.20 MPa respectively at a distance of 1.5 mm from the transducer surface (Figure 5.6a). Corresponding -6 dB bandwidths measured for these probes were 28.5, 31.7, and 32.6 MHz, respectively (Figure 5.6b). The US field scans demonstrated that the US generated by all three configurations was circularly symmetric (Figure

5.6c−e)). The beam width was similar with increasing axial depth for the configurations, however, the simple device had the narrowest beam width at a depth of 10 mm with a value of 1.8 mm (Figure 5.6f)). Conversely the capillary configuration had the largest beam width with a value of 2.2 mm. When high-pass frequency filtering was applied the beam width decreased for all configurations, with values of 1.3, 1.5, 1.7 for the simple, spliced, and capillary devices, respectively.

Generator Type	**Pk to Pk Pressure [MPa]**	**−6dB Bandwidth [MHz]**	**Beamwidth at 10 mm > 1MHz**
Simple	2.70	28.5	1.8
Spliced	2.69	31.7	1.9
Capillary	2.20	32.6	2.2

Table 5.2: Generated Ultrasound characteristics

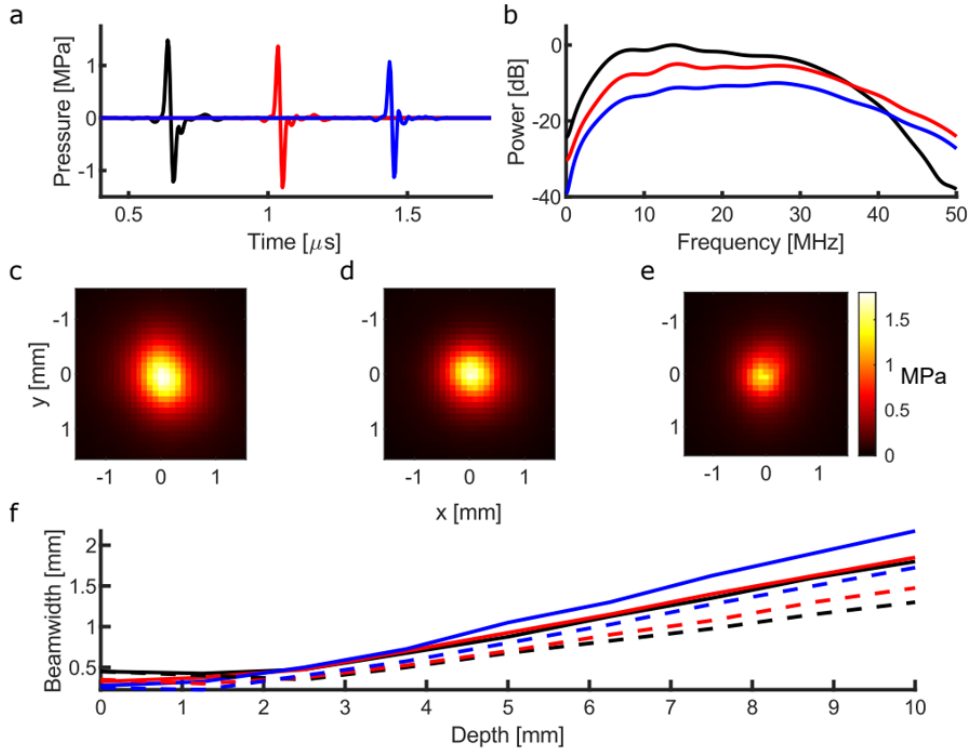

Figure 5.6: Comparison of US characteristics for the three transducer configurations

a) US time-series as measured at 1.5 mm from the devices; simple (the black line is shifted -0.4 μs for display purposes), spliced (red line), and capillary (the blue line is shifted +0.4 μs for display purposes); b) The corresponding US spectra from the configurations plotted using the same colours for comparison; c), d), e) US field scans for the simple, spliced, and capillary configurations, respectively, measured at a distance of 1.5 mm from the transducer surface; f) US beamwidth for all configurations, the solid line demonstrates the full power spectrum whilst the dashed line shows the effect of $>$ 20 MHz high pass filtering.

5.4.2 Vascular imaging

With OpUS, the stent graft was displayed as an echo-bright linear structure (Figure 5.7). Aortic tissue was clearly visible beneath this to a depth of 5 mm from the transducer surface, with no significant attenuation to signal from the stent graft. The linear pullback revealed the side-branch within the aorta, which was visible as a well demarcated area of signal drop-out, consistent with an absence of tissue.

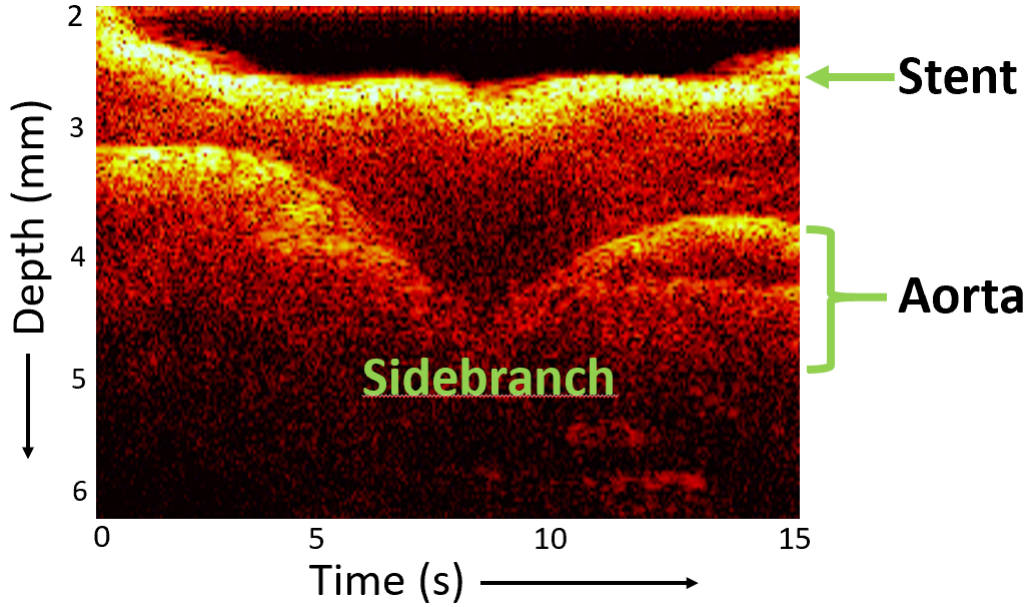

Figure 5.7: OpUS imaging of stent graft and ex-vivo Aorta

The stent graft material is highly reflective to OpUS generating an echo-bright signal. The Aorta is visible beneath this as a 2 mm thick structure. The side-branch is demonstrated as an absence of signal, representing a discontinuity in the Aortic tissue. The first 1 mm of signal from the image has been removed to exclude cross-talk artefact.

5.4.3 Contact sensor

5.4.3.1 Norland 81 epoxy dome

Figure 5.8a shows the phase of Δ Z for the epoxy dome. As the phase is directly proportional to the distance, the data plot in figure 5.8b represents the changes in the distance of Δ Z (distance from the tip of the contact sensor to the tip of the fibre) over time. For the first 0.6 minutes of recording the phase is constant as the sensor is advanced towards the dacron material (DM). Contact is the made between the sensor and the DM causing a decrease in the phase (Δ Z) by $\approx$ 1.1 radians. Once the sensor is withdrawn the epoxy dome rapidly returns to its original size with a corresponding increase in phase back to the original baseline.

5.4.3.2 PDMS dome

Figure 5.8c displays the interference pattern for the PDMS dome with Z^1 as the fibre surface and Z^2 as the tip of the PDMS dome. For the first minute of recording

the phase remains constant during sensor advancement. When contact is made with the DM there is a change in the phase, representing deformation of the dome. When the sensor is then withdrawn from the DM the phase fails to return to the baseline. Further contact with the DM is made at minute two and minute three. These cause changes in phase, similar to the original contact.

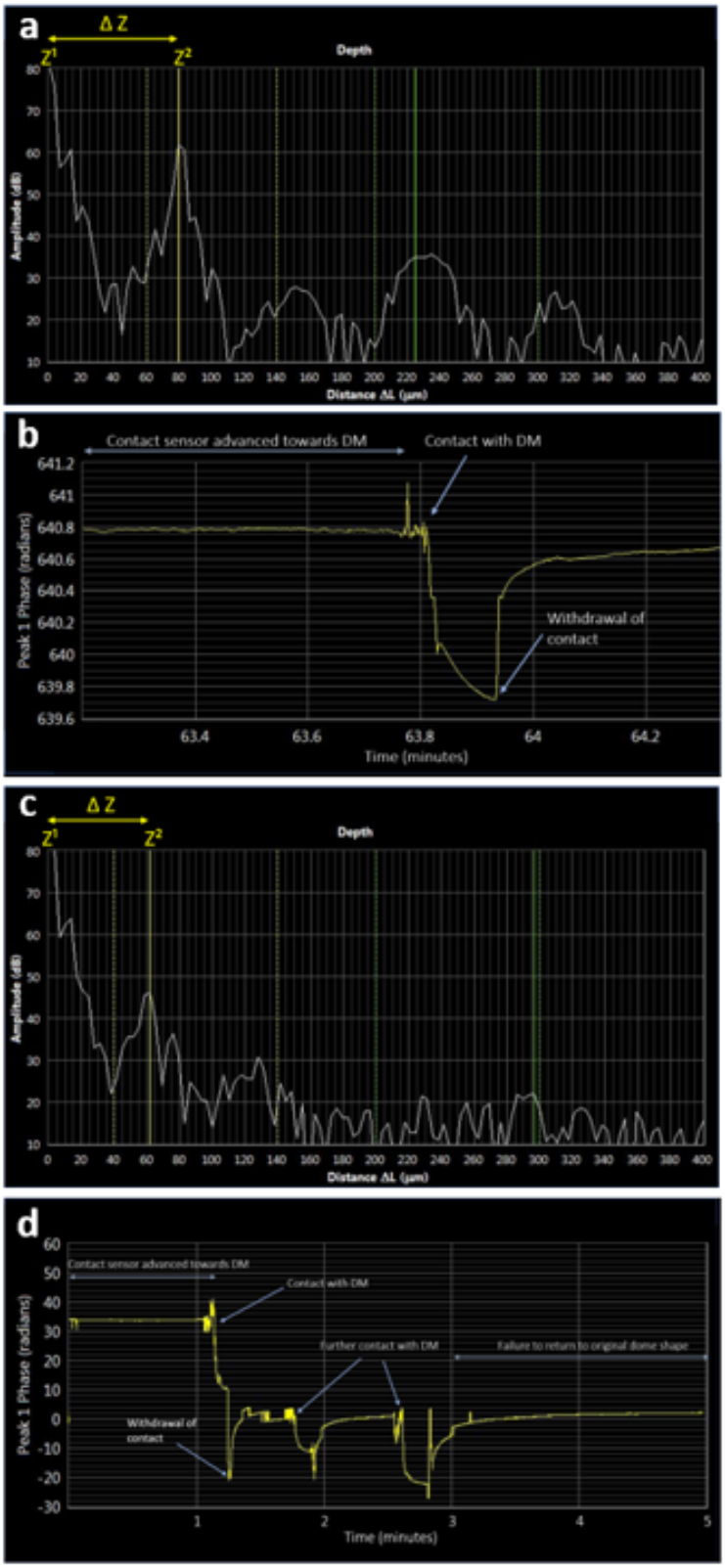

Figure 5.8: Characterisation of optical contact sensor

a) Inverse fourier transformation of the Epoxy dome interference pattern; b) Phase of ΔZ for the Epoxy dome. The ΔZ remains constant whilst the sensor is advanced towards the DM. When contact is made the dome is deformed leading to a decrease in ΔZ. Once contact is removed the ΔZ phase returns to baseline; c) Inverse fourier transformation of the PDMS dome interference pattern; d) Phase of ΔZ for the PDMS dome. The ΔZ remains constant whilst the sensor is advanced towards the DM. When contact is made the dome is deformed leading to a decrease in ΔZ. Once contact is removed the ΔZ phase fails to return to the original baseline. Subsequent contact with the DM result in a similar change in ΔZ. Once this contact is removed the ΔZ phase returns to the modified baseline.

5.4.4 Laser Fenestration

Figure 5.9 shows the effects of varying power output and laser pulse duration on the success of the fenestration and resultant macroscopic tissue damage. When in contact with the stent material a reproducible fenestration was successfully created with a minimum of 1.8 W and a 0.5 s pulse duration. There was no macroscopic tissue damage with these parameters. The size of the fenestration increased with both higher power outputs and longer duration of the laser pulse. When the optical fibre was moved to a distance of 3 mm from the stent material both a higher power output and longer pulse duration were required to generate a fenestration. No macroscopic tissue damage was identified during any of the fenestration experiments. As a control, the optical fibre was placed directly on the tissue with no stent material. A power of 4.2 W and pulse duration of 5 s resulted in a macroscopic thermal ablation of the tissue.

Power (W)	Duration (s)	Contact	Stent (x2 magnification)	Tissue (x0.7 magnification)
2.5	0.5	3mm away	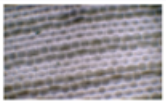	
1.8	0.5	✓		
4.2	0.5	✓		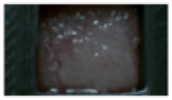
4.2	1	✓		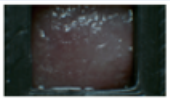
4.2	5	✓	Not present	

Figure 5.9: Laser fenestration results

The effects of varying laser power output and pulse duration on stent fenestration are shown. Contact between the fenestrating fibre and stent material is indicated by a green tick. The underlying tissue was macroscopically examined for thermal damage after each fenestration attempt.

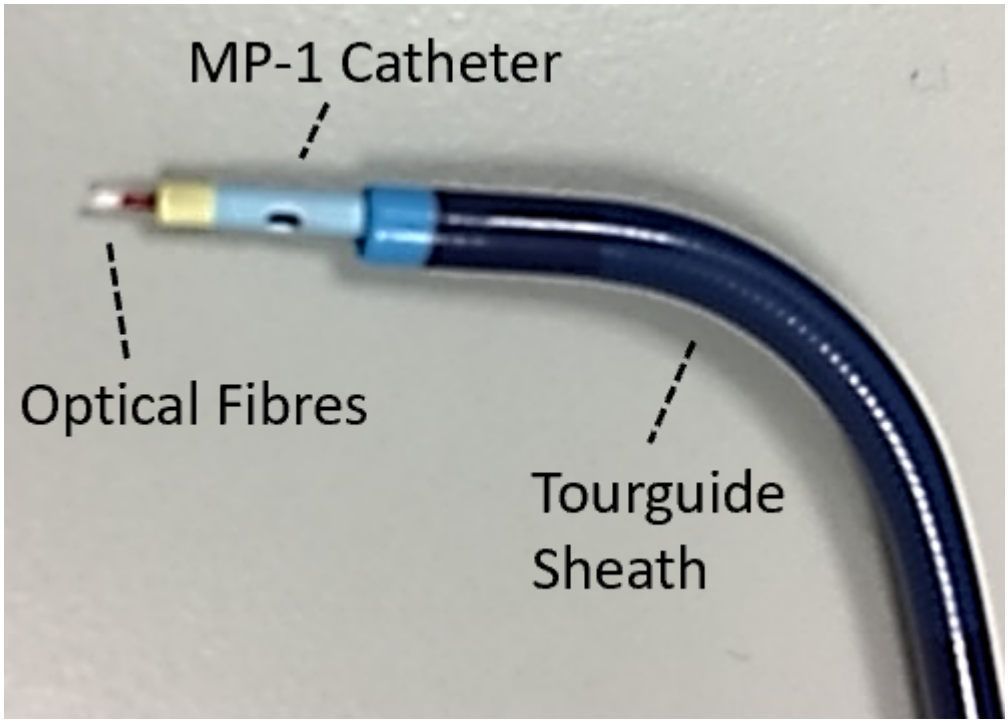

Figure 5.10: Fabricated device

The 4 optical fibres are bundled together with heatshrink to create a probe. This probe is housed within a multipurpose diagnostic catheter. The Tourguide sheath is a steerable device that offers bi-directional 180°/90°deflection, enabling the device to be positioned within the Aorta appropriately.

5.4.5 Device Fabrication

Following characterisation of the individual components, the ISF device was fabricated according to the design described in Section 5.3.1. The four optical fibres were bundled together with sealant wax and heatshrink (Nordson Medical, Louisville, CO, USA) to form a probe. This was housed within a 6 Fr ID multipurpose-1 diagnostic catheter (Cordis, Santa Clara, Ca, USA) (Figure 5.10). A haemostatic valve was connected to the proximal end of the catheter and through this a 5 cm section of steel hypotubing (ID 1.2 mm) was inserted. The probe was first passed this, before the hypotube was filled with a quick drying epoxy. The result of this was that movement of the hypotube through the haemostatic valve allowed the probe to be advanced out of or withdrawn into the tip of the catheter, without risk of excessive blood loss during a procedure.

5.4.6 In-Vivo Swine Model

5.4.6.1 OpUS imaging of vascular structures

M-mode OpUS imaging of the aortic valve is displayed in Fig 5.11a. The device is positioned in the ascending aorta with the probe directly facing the aortic valve. With this the first 5 mm of signal from the probe is cross-talk artefact. At a depth of 7 mm from the probe there is a clear signal representing an aortic valve leaflet. The aortic valve is predominantly in the closed position but the valve leaflets regularly open creating the appearance of a cleft in the tracing. These occur 3 times every 2 seconds, representing a heart rate of 90 beats per minute. M-mode OpUS imaging of the proximal right coronary artery is displayed in Fig 5.11b. The device is in the right coronary sinus with the imaging probe directed towards the right coronary artery. The signal has fine oscillations consistent with pulsatile flow. There is also a larger variation in the depth of the signal between 10 mm and 20 mm depth from the probe, consistent with respiration (rate 15 breaths per minute). Following successful imaging of the aortic valve and coronary artery an OpUS pullback from the ascending aorta across the right subclavian artery origin was performed (Fig 5.11c). Signal is seen here at a distance of 5 mm from the probe, consistent with the aorta. The signal then disappears after 4 seconds of pullback as the probe moves across the origin of the subclavian.

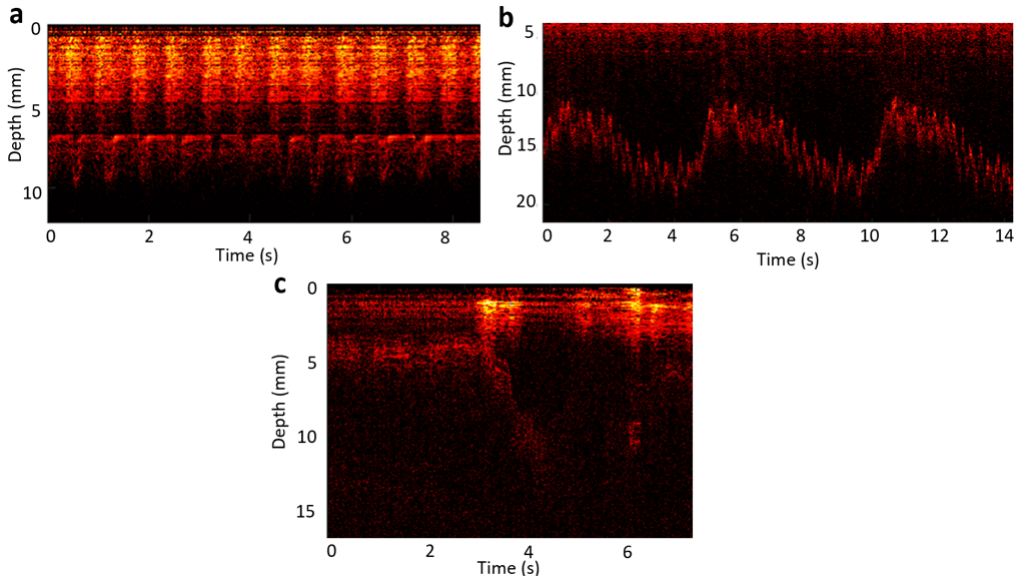

Figure 5.11: OpUS imaging of Vascular structures

a) Aortic Valve - M mode imaging showing the opening and closure of the aortic valve leaflets at a distance of 6 mm from the probe. The first 5 mm displays cross-talk artefact. b) Coronary Artery - M mode imaging of the proximal segment of the Right Coronary Artery. Tissue layers are evidence at a depth of 10 - 20 mm from the probe. c) Pullback imaging of probe from Aorta into right subclavian. Tissue is initially evidence at a distance of 5 mm from the probe surface for the first 3 seconds of recording. After 3 seconds the tissue is visible at an increasing depth from the probe surface until it is no longer visible after 4 seconds of recording. Signal between the probe surface and 5 mm of depth is due to cross-talk artefact.

5.4.6.2 In-situ Fenestration during EVAR

During in-vivo 1 the endograft was deployed from the distal portion of the abdominal aorta into the right external iliac artery. The experimental device was inserted through the LFA and positioned under fluoroscopy. OpUS imaging was then performed to confirm no tissue signal was present under the endograft. Subsequently the device was used to generate a fenestration in the graft. This fenestration was wired and sequentially ballooned to preserve distal flow through the left external iliac (Fig 5.12c. For in-vivo 2 J-tip wires were passed, via the LFA, into both renal arteries to provide radiological landmarks. The endograft was then inserted via the RFA and deployed in the abdominal aorta, across the renal bifurcation. The experimental device was inserted through the RFA and passed into the endograft. An OpUS pullback was performed (Fig 5.12a), which highlighted an area of ab-

sent tissue signal behind the endograft, consistent with the left renal artery. The device was then used to create a fenestration, which was subsequently wired with a 0.018 inch coronary wire (Fig 5.12d). This fenestration was then successfully dilated with incrementally larger diameter balloons. Figure 5.12b shows the result of the fenestration on the endograft, post explantation at the conclusion of the case.

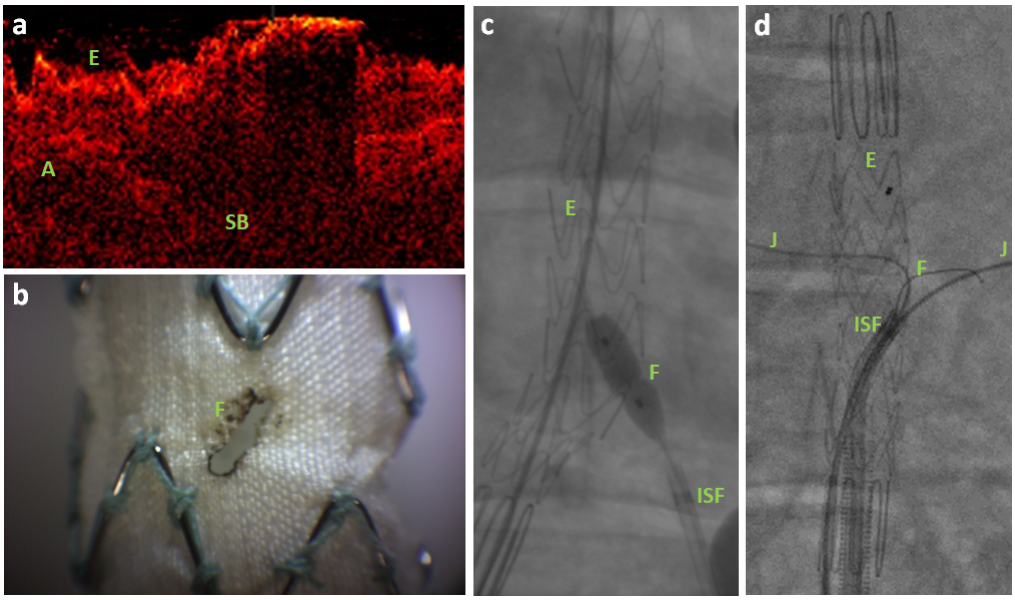

Figure 5.12: In-situ Fenestration during in-vivo experiments

a) OpUS imaging displaying pullback across renal bifurcation; A is the Aorta, E is the endograft stent material, SB is the side-branch (renal artery). b) Optical microscopy of the endograft, post autopsy, displaying a fenestration (F). c) Fluoroscopy of the ISF procedure during In-Vivo 1. E is the endograft deployed with the superior end in the abdominal aorta and the distal end extending into the right common iliac. ISF is the experimental device. F is a balloon that has been inflated across the fenestrated section of endograft. d) Fluoroscopy of the ISF procedure during In-Vivo 2. E is the endograft deployed with the superior end in the abdominal aorta and the distal end extending into the right common iliac. ISF is the experimental device. J are the J-tip wires that mark the location of the renal arteries. These are outside of the endograft. F is the fenestration within the endograft with a wire visibly passing through into the left renal artery.

5.4.6.3 Histology

In total 41 tissue slides stained with Haematoxylin and Eosin, and 41 tissue slides stained with elastin Van Giesson were submitted for histology. The full data set is described in detail in Appendix B. Of the 11 tissue samples from the healthy control group 4 showed varying degrees of tissue damage. Three of the sections (A1, A5,

A6) have areas of tissue loss with multifocal elastin/collagen disruption. Sample D1 displayed a degree of luminal tissue loss but without elastin/collagen disruption. Of the 10 tissue samples from the diseased control group 6 showed evidence of tissue damage with varying degrees of luminal tissue loss and elastin/collagen disruption. Of these, sample C3 showed evidence of significant cauterisation damage with a lesion measuring 0.92 mm in depth and 2.81 mm in length. Of the 8 samples submitted from In-vivo 1, only section G2 displayed a significant lesion measuring 0.17 mm deep and 0.76 mm wide (Figure 5.13). Of the 11 samples submitted from In-vivo 2 there were no significant lesions demonstrated (Figure 5.14).

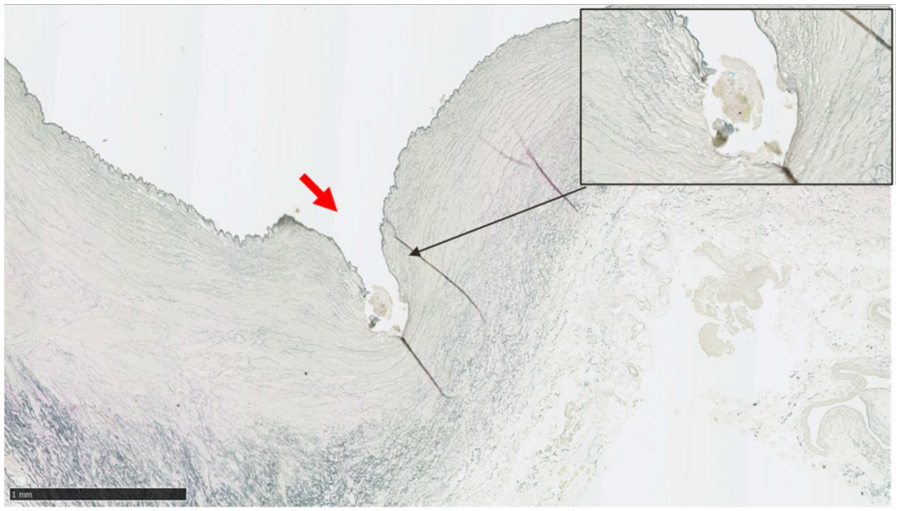

Figure 5.13: Section G2; In-vivo 1

Elastic Van Giesson staining. The red arrow indicates a focal area of vessel clefting with an intraluminal aggregate of degenerate tissue. This damage is not transmural (involving all 3 tissue layers). Scale bar: 1mm.

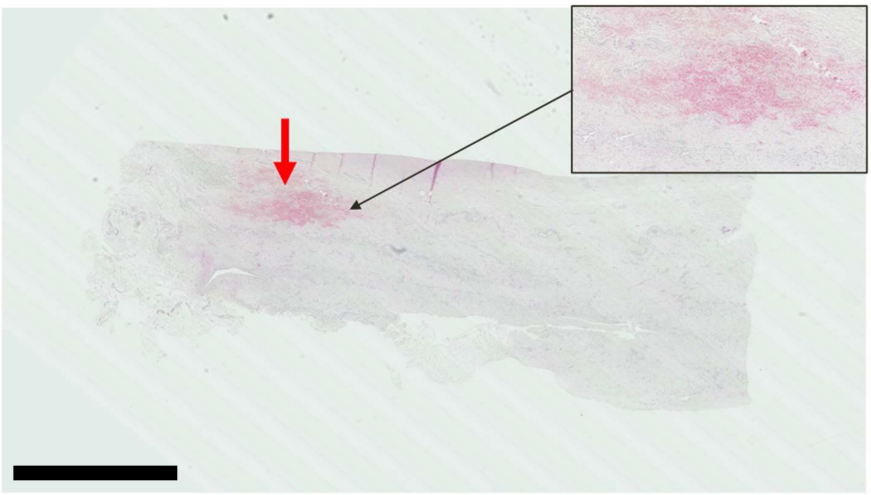

Figure 5.14: Section H1; In-vivo 2

Haematoxylin and Eosin staining. The red arrow indicates an intramural lesion that is haemorrhagic and features elastin/collagen degeneration. Scale bar: 1mm.

5.5 Discussion

Here, I have presented two differing methods for the fabrication of highly flexible OpUS generators with a smaller diameter optical fibre body and a larger distal section for ultrasound generation. The first method involved splicing a short 400 μm core diameter optical fibre section onto the end of a 200 μm core diameter optical fibre, whilst the second comprised affixing an epoxy filled glass capillary (ID: 400 μm, OD: 550 μm) to the distal tip of a 200 μm optical fibre. The use of a proximal fibre with a smaller diameter allowed a low minimum bend radius of 10.5 mm, facilitating the utility of these transducers in complex and tortuous anatomies. Furthermore the low bend radius allows for deflection of the steerable tip catheter, a crucial stage in the potential detection of Aortic side-branches. The two fabricated devices were compared to an US generator based on a 400 μm core diameter optical fibre that had no additional distal tip fibre component. All of the devices were dip-coated with a dye-PDMS optical ultrasound generating coating. The combination of a highly flexible device offering directional US generation makes these devices ideally suited to minimally-invasive imaging applications where devices must undergo tortuous pathways whilst simultaneously providing real-time imaging. The

nanocomposite coatings fabricated in this study exhibited a high optical absorption and microscopy of the coatings showed that they formed uniform layers across the distal surfaces of all the devices. The US pressures generated by all three device configurations were comparable to those previously used for in vivo imaging [45]. Furthermore, the corresponding -6 dB bandwidth for both the spliced and capillary devices was greater than 30 MHz, a value crucial for achieving high axial resolution when performing intravascular imaging [142][36][45]. For all devices the beamwidth measured at a distance of 10 mm from the device was $\approx$ 2 mm. Whilst the smallest beamwidth was achieved by the simple device, the beamwidth at 10 mm exhibited by the spliced device was 0.1 mm larger. Through the use of frequency filtering to exclude divergent lower frequencies, the beamwidth for both devices at 10 mm was reduced to $<$ 2 mm. The high directionality of these devices suggest that these US generators are ideal for M-mode or sweep imaging, where the lateral resolution is dependent on the beamwidths achieved. Longitudinal follow-up over time suggest that the dye-PDMS coatings had excellent photostability. Over a period of 2 hours the devices were in continuous use and there was no observed change in acoustical performance. Each of the two fabrication methods presented offers advantages. In terms of beam divergence the spliced device outperformed the capillary device, however the fabrication process necessitated fibre polishing and additional preparation steps to enable optical fibre splicing. During this process the 400 μm fibre section was at risk of damage. The spliced devices had to be fabricated in series and each step in the process required specialised equipment and was time consuming. The special equipment needed included fibre polishing facilities and an optical fibre splicer. By contrast, fabrication of the capillary devices did not necessitate specialised equipment and could be made using widely available epoxy and a basic low cost UV light source. Additionally, for the capillary device parallel fabrication of several devices in one batch was possible, which has implications on scalability. For instance it was possible to fabricate 20 devices within a 3 hour period, whilst for the spliced devices a similar number would require 20 hours. The devices that have been presented overcome the minimum bend radius limitation which has

been an issue with previous OpUS devices [183], with a minimum bend radius of 10.5 mm. However, to achieve higher US beam collimation, previous devices have used either larger US generating apertures (up to 600 μm [183] or a concave distal surface [41]. The fabrication methods presented here could be further adapted to incorporate wider US generating apertures, depending on the size limitations of the desired clinical application, whilst maintaining flexibility. This might be achieved by either splicing a larger core fibre, or by using a larger diameter glass capillary. This may require a stepped process, whereby there is a sequential splicing of fibres with a gradually increasing core diameter fibres, or similarly with glass capillaries, in order to provide the device with added reinforcement. As mentioned in Chapter 4 there exists a degree of manufacturing variability and overall imaging performance, likely related to variations in the probe nanocomposite. Out of a batch of 20 probes approximately 16 (80%) would be able to generate sufficient US pressures. Due to the batch manufacturing method and low cost materials involved this was deemed an acceptable attrition rate. All manufactured probes, however, needed careful characterisation before use. Performance variability is a key topic with implications for larger scale studies and commercial implementations. Further refinements to fabrication rigs may allow for improvements and will need to be the subject of further research.

Previous studies had shown the utility for OpUS to identify vascular components including endothelium, media, tunica elastica and side-branches [142]. The images obtained from the ex-vivo experiment demonstrated, for the first time, that OpUS can also be successfully used to image tissue beneath an endograft stent. The stent provides a bight echo-reflective structure but the aortic tissue layers are visible beneath this without significant signal attenuation. Tissue is visible up to a depth of 6 mm from the probe, relevant to the likely distances between an endovascular stent and Aorta in-vivo. The side-branch can be readily identified as a well demarcated area without tissue. Imaging in this fashion would allow real-time alignment of the device over the side-branch, allowing appropriate positioning of ISF. As previously mentioned in Chapter 4.5, further improvements in image post-processing can be

envisaged. These include complex filtering, reconstruction and adaptive frequency filtering [34][146][147][148]. Improvements in lateral resolution are achievable by tightening beam collimation. Methods for this include the use of a concave transmitting surface or by increasing the diameter of the transmitting fibre [149]. The latter, however, would potentially result in reduced device flexibility [149].

Both contact sensor configurations were able to detect when contact was made between the device and the Dacron material. When the contact was removed from the Epoxy based sensor there was a rapid return in the ΔZ back to the original baseline. In contrast following removal of contact from the PDMS based sensor the ΔZ phase did not return to the original baseline but instead remained permanently altered. Examination of the PDMS sensor revealed that the dome shape had been deformed during the contact process. The differences encountered between the two sensor materials can be explained by their mechanical properties. The epoxy is significantly harder than the PDMS with a lower Youngs modulus (0.2 vs 19 - 27) and is therefore more resistant to compression. This makes it less sensitive to contact than the PDMS during the experiment (1.1 vs 53 radians). Due to the softness of the material, the large contact forces exerted on the PDMS appear to have been sufficient to permanently distort the dome shape. For the purposes of the in-situ fenestration device a highly sensitive contact sensor is not required as the absolute values obtained are not of interest. Given the apparent lack of robustness of the PDMS material in this instance it appear that epoxy is the more suitable material for this indication. A significant advantage of the sensor fabrication method presented here is that the materials used are of low-cost and the fabrication time is less than 30 mins (for the epoxy sensor). Other fibre optic contact sensors, for instance those based on fiber bragg gratings, tend to be complex and allow for a degree of sensitivity/quantification that is not necessary for this application [184][185]. It could be envisaged that the FOH, comprising a Fabry-P*é*rot cavity and used in OpUS imaging, could be used as a contact sensor. This would have the benefit of further reducing the ISF to a three fibre design. A caveat to this is that the FOH tends to be fragile and is slightly recessed from the tip of the device, to prevent damage, and

therefore would require significant reinforcement.

I have demonstrated that fenestrations can be made through endograft material using an LED operating in the 808 nm range. This wavelength was chosen to minimize damage to the underlying vascular tissues [172]. The minimum requirement for generating a fenestration was a 1.8 W power output with a pulse duration of 0.5 seconds, consistent with previous studies [172]. With this there was no observed macroscopic damage to the underlying tissue. Indeed there was no macroscopic evidence of tissue damage during any of the fenestration attempts. There are several limitations to this setup. Firstly the distance of the endograft to the tissue was fixed at 2 mm. In Vivo the distance between endograft and Aortic wall is likely to vary and in places be less than 2 mm. The tissue used in this experiment was pork loin, mainly consisting of muscular tissue. The vascular endothelium of the Aorta, however, may be more susceptible to ablative changes. Lastly, in-vivo the Aorta is subject to pulsatile blood flow. The fast flowing blood surrounding the endograft may lead to greater dissipation of heat, necessitating a higher power output and/or pulse duration in order to generate a successful fenestration. The stent used in this work was a Zenith Flex (Cook Medical, Bloomington, Il, USA) made of Polyethylene terephthalate (PET). There are, however, multiple different stent materials used commercially for EVAR. Preliminary experiments of an alternative stent (GORE Excluder, GORE Medical, Newark, DE, US) made of Polytetrafluoroethylene (PTFE) demonstrated that significantly higher powers are required to generate a fenestration. This is likely due to a higher melting point of the PTFE stent (260°C PET v 330°C PTFE). It can therefore be postulated that certain stent fabrics may be more suitable for ISF than others. Previous work in this field has predominantly used peripheral vascular disease laser atherectomy catheters, operating at wavelengths in the 308 nm range (CVX-300 Excimer Laser System, Spectranetics, Colorado Springs, CO, USA). Extensive injury caused by creating fenestrations using these re-purposed catheters has generated concerns regarding the long term durability of the endovascular stents following these procedures [186]. It would therefore also be of interest to investigate the long term mechanical durability of

stents fenestrated using the ISF device as stent disruption may increase the risk of endoleak and necessitate re-intervention.

Both in-vivo experiments successfully demonstrated the clinical utility for OpUS in guiding ISF during EVAR. With OpUS the tissue layers of a variety of vascular structures, including aortic valve and coronary artery, were readily visible. Imaging of valvular apparatus in this manner may have a role in guiding percutaenous valvular treatments, such as mitraclip or tricuspid valve intervention [187][188]. By including an ultrasonic receiver in current interventional devices it may be possible to use ultrasound tracking technology to help guide the operator as to the exact location of the device [189]. Using OpUS it is possible to image beneath endograft material, at depths of over 20 mm from the probe tip, and detect vascular side-branches. The ability to detect a side-branch allows the operator greater confidence when generating a fenestration, reducing the risk of inappropriate positioning and subsequent need for conversion to open surgery in order to prevent long term complications. During the procedure there was a recurrent loss of ultrasonic tracking by the fibre-optic hydrophone. This introduced time delays in order to allow the tracking to be reset. One explanation for this is that there may be signal loss due to exceeding the bend radius of the US receiving optical fibre. A solution to this would be to use bend insensitive optical fibres for future fibre-optic hydrophones (S.Mathews et al., in preparation). The dimensions of a swine aorta necessitated a relatively small diameter endograft. As a result a steerable catheter with a short bend radius was needed in order to achieve perpendicular imaging. By contrast the endografts used in human EVAR are significantly larger in diameter and therefore a steerable catheter with a larger bend radius could be envisaged, which would minimise signal loss from the US receiving fibre. A second explanation for the loss of US tracking could be that the high velocity of blood within the aorta is generating noise within the FP cavity. This could be addressed by recessing the hydrophone from the device tip or adding a degree of protection in the form of an US transparent film. Optical fenestration with the 808 nm wavelength source generated successful and reproducible fenestrations through the endograft material. The laser output set-

tings that were used (4.2 W, 5 secs) were intentionally high to ensure a fenestration was generated. Bench-top evaluation had demonstrated that significantly lower output settings could be used to create a fenestration but this was in an environment without pulsatile flow. Due to the lack of real time visual feedback of the fenestration, during the procedure, a higher output setting was chosen to ensure success. It remains to be determined whether using a lower output setting may be possible in an in-vivo setting.

Focal thermal ablation injury is expected to induce focal protein coagulation that will involve both the elastin and the collagen of the vascular wall. These lesions may or may not be coupled with tissue loss. Of the 19 total samples submitted from the in-vivo experiments, only 1 showed evidence of an ablative lesion (H2). This was a relatively narrow cleft, measuring 0.17 mm deep and 76 mm wide. There was, however, no elastin damage or tissue mural loss. It is unclear what the clinical significance of a lesion such as this would be. Indeed a degree of intimal surface damage would be expected during a routine EVAR procedure due to the manipulation and deployment of the endograft. In the absence of significant mural damage it can be envisaged the risk of a visceral perforation would be low. Furthermore, the energy output used to generate the fenestration were intentionally above the threshold levels required in order to guarantee a successful procedure. In future work it would be of interest to examine the in-vivo histological effect of lower energy output levels.

In this chapter I have outlined the development of a interventional device capable of detecting sidebranches beneath endograft material, detecting contact with the material and then successfully generating a fenestration through the material. A device with this functionality would offer the operator the opportunity to safely create ISF during EVAR, in order to maintain access to visceral aortic branches. Current methods for generating ISF, although promising, are not guided by intravascular imaging. With these there is therefore a risk of creating a fenestration that is not aligned with the side-branch, leading to a potential endoleak, or a risk of causing injury to underlying structures. One of the most controversial topics in Vascular

surgery over the past 5 years has been the recommendation by NICE, in the 2020 guidelines for the management for AAA [154], that open surgery should be the preferred management option for patients with complex AAA. This was despite a growing body of evidence that at least in the short term clinical outcomes of EVAR were superior. The justification given for this was a lack of long term risk data with regards to EVAR and an unfavourable cost-effectiveness estimate. The high cost of EVAR is predominantly driven by the cost of the endograft device. In the most recent UK audit of complex Aortic procedures (2015 - 2017) there were 2,303 procedures performed during this time frame [190]. Of these, 90% (n = 2,074) of cases were performed using a FEVAR procedure rather than open surgical methods (n = 229). 42% (n = 871) of the FEVAR cases used custom-made devices, with the rest using pre-fenestrated devices (n = 1203). The resultant average delay in the patient undergoing their elective procedure, necessitated due to the fabrication time of these devices, was 67 days. The cost implication of using potentially using ISF rather than pre-fenestrated or custom-made devices is significant. The average cost of a pre-fenestrated graft is in the region of £15,400. A custom-made patient specific graft costs upwards of £24,000 dependant on the level of complexity required. In contrast a non-fenestrated Aortic endograft costs on average £6,000. As a rough estimate, using the audit data, the device cost to the NHS for FEVAR procedures during this 3 year period would have been £39.4 million (Pre-Fenestrated: 15,400 $\times$ 1203 = £18.5 million, Custom-made: 24,000 $\times$ 871 = £20.9 million). If all these cases had instead been performed using ISF for non-fenestrated grafts then the total cost would have been approximately £12.4 million (6,000 $\times$ 2074). The cost saving would have been £27 million (39.4 million - 12.4 million) over the 3 year period. This does not take into account the additional cost benefit of avoiding lengthy delays in patient treatment with the potential for emergency admissions and subsequent morbidity. There would be an added cost in the form of the ISF console and device, however the total fabrication cost of prototype was less than £500. Further reductions in the cost of the ISF can be envisaged with economies of scale. If the cost of performing complex EVAR procedures can be reduced then it may

have a significant impact on future clinical guidance regarding EVAR versus open surgery for the repair of unruptured AAA.

5.6 Conclusion

As an intravascular imaging modality, OpUS can be used to detect side-branches beneath an endograft. The imaging probe can be readily integrated into a custom built interventional device, capable of performing ISF and thereby facilitating complex EVAR procedures.

Chapter 6

General Conclusions and Future Work

6.1 Chapter 2: Mesoscale Imaging Phantoms

In this chapter a novel hybrid approach to creating mesoscale imaging phantoms was proposed. This involved 2PP 3D printing of intricate scaffolds coupled with micro-injection of optically tailored tissue mimicking materials. Using this method three different phantoms were demonstrated, each highlighting a different key component. The Resolution phantom included small scale features, with a minimum wire diameter of 5 μm, suitable for use in the characterisation of system performance. The Side-branch phantom displayed the potential for complex anatomical geometries with a 45°bifurcation surrounded by tissue-mimicking material. The Lipid plaque phantom included areas of differing optical contrast, both organic and non-organic, in order to simulate common pathology. These phantoms were validated using OCT which is the highest resolution intravascular imaging modality used in clinical practise. Future work in this area should focus of generation of additional phantoms which mimic common arterial pathologies such as intimal dissection and mural calcification. This will necessitate the development of further TMMs. It is also of interest to simulate the appearances of a stent scaffold within the vascular structure, given the role of intravascular imaging in the assessment of stent expansion and apposition. Speculatively, by fabricating and inter-connecting

multiple phantoms in series, a longer tubular structure similar to a coronary artery could be envisaged. This would allow for longer pullback acquisitions and the ability to assess multiple pathologies at the same sitting. Finally, 2PP printing of multiple photoresists, within the same phantom, should be explored as this may provide an alternate method for introducing optical contrast without the need for separate incorporation of TMM.

6.2 Chapter 3: Patient-specific Vascular Multimodality imaging Phantoms

The work in this chapter described a new fabrication method for large scale complex vascular phantoms, compatible with multiple imaging modalities. The use of 3D printing patient-specific vascular structures in a water-soluble printing material (PVA) and then surrounding these with TMM allowed generation of high-fidelity 'wall-less' phantoms. The vascular structures demonstrated were a carotid artery bifurcation and a complex AAA. Both structures are areas of interest to vascular surgeons, due to common occurring pathologies, and require several different imaging modalities in their assessment. After fabrication, the phantom was validated using US, CT and fluoroscopy, which are frequently used during vascular assessment. The images obtained from phantoms provided an excellent qualitative result. The US of both phantoms demonstrated clear well-demarcated hypoechoic areas consistent with vessel lumen. This was surrounded by homogenous hyperechoic signal consistent with connective tissue. CT images of the complex AAA compared favourably with the CT images that the phantom was derived from. Additionally, the utility of the complex AAA phantom as a clinical training model was demonstrated, using fluoroscopic guidance, to deploy an endograft during an EVAR simulation.

Further work in this field should include tailoring of the TMM to offer CT and MRI contrast. Addition of a lipid-soluble radio-opaque contrast agent, such a lipiodol (ethiodized oil), to the gel-wax would potentially simulate the appearances of differing types of soft tissue during CT acquisition. Differing concentrations of

lipiodol to gel-wax could be characterised using hounsfield units (a CT measurement of signal density) to increase the fidelity of the model. Additionally it would be of interest to integrate phantoms fabricated into this manner into a flow circuit, to assess the effect of pulsatile flow on the model. The mechanical properties of the TMM could be altered, to achieve the desired elasticity, through the addition of paraffin oil.

6.3 Chapter 4: Optical Ultrasound: Ex-Vivo Vascular Imaging

In this chapter a forward-viewing OpUS imaging probe was fabricated using a transducer, dip-coated in a MWCNT-PDS composite, paired with an omnidirectional FP cavity-based FOH. The probe generated a high US pressure (21.5 MPa at the surface) and a broad corresponding -6 dB bandwidth of 39.8 MHz. Using this probe, OpUS imaging of an ex-vivo human coronary artery was performed. With this areas of calcification and lipid infiltration were readily identifiable. The images compared favourably with both OCT and IVUS acquisitions of the same diseased ex-vivo sample. Histology analysis demonstrated good correlation with the OpUS findings. A side-viewing OpUS imaging probe was successfully fabricated by polishing the distal end of an optical fibre to 45°, coating with a silver mirror and affixing a MWCNT-PDMS coated epoxy cap to the distal tip. With this the US pressure at a distance of 1.5 mm from the transducer surface was 1.87 MPa with a corresponding -6 dB bandwidth of 31.3 MHz. Using depth-dependant frequency filtering the axial resolution of the system was 54 μm at < 3 mm and 59 μm at 10.5 mm from the probe surface. Using a custom built fibre-optic rotary junction and stepper motor, a rotational image acquisition was successfully acquired. This demonstrates that rotational OpUS imaging is viable and paves the way for a future clinical device.

Further work in this field should include investigating additional methods for improving image quality. These include complex filtering and reconstructive techniques to allow differentiation between acoustically heterogenous tissues

[34][146][147][148]. Additionally the lateral resolution can be improved through increased beam collimation. One method for this would be through the use of a concave transducer surface. To allow hybrid imaging with PA and NIRS, further work is required to identify and characterise additional selectively absorbing optical coatings.

6.4 Chapter 5: Optical Ultrasound: Development of an interventional device

This work describes the development of an OpUS based interventional device to facilitate ISF during complex EVAR. The all-optical design comprised an OpUS transducer, FOH, contact sensor and fenestrating fibre. The OpUS transducer incorporated a novel glass capillary based tip, designed to provide optimal beam collimation, whilst maintaining device flexibility. With this paradigm, US pressure at 1.5 mm from the transducer surface was 2.2 MPa with a corresponding -6 Db bandwidth of 32.6 MHz. Ex-vivo imaging demonstrated the ability of OpUS to image beneath an endograft and detect a vascular side-branch at depths of up to 5 mm from the transducer surface. Following successful benchtop demonstration of imaging and fenestration, the device was used in 2 in-vivo experiments on a swine model. OpUS imaging was performed of various structures including the coronary artery and aortic valve. With OpUS it was possible to detect a side-branch, covered by an endograft, and use this to perform a successful ISF procedure. Histological analysis of the surrounding tissues did not highlight any significant elastin damage or mural tissue loss. It appears that OpUS is highly suited to guiding interventional procedures.

One of the key current limitations of obtaining high quality in-vivo imaging is due to loss of hydrophone tracking. Immediate improvement in this could be envisaged through the use of bend insensitive fibres for the FOH. Research into this field is currently being undertaken by the interventional devices group at University College London. The imaging device would also benefit from integration into a catheter material transparent to light and US, to provide a degree of protection for

the sensitive FOH tip. These successful in-vivo experiments should pave the way for a first in man study of OpUS imaging and subsequent rapid clinical translation of this emerging imaging modality.

Chapter 7

Research Impact

7.1 Publications

'Micron resolution, high-fidelity three-dimensional vascular optical imaging phantoms'

Little CD, Poduval RK, Caulfield R, Noimark S, Colchester RJ, Loder CD, Tiwari MK, Rakhit RD, Papakonstantinou I, Desjardins AE (2019). *Journal of Biomedical Optics* 24(2) https://doi.org/10.1117/1.JBO.24.2.020502

'All-optical rotational scan ultrasound imaging'

Colchester RJ, Little CD, Dwyer G, Noimark S, Alles EJ, Zhang EZ, Loder CD, Parkin I, Papakonstantinou I, Beard P, Finlay MC, Rakhit RD, Desjardins AE (2019). *Nature Scientific Reports*. https://doi.org/10.1038/s41598-019-41970-z [136]

'Dynamic physiological temperature and pressure sensing with phase-resolved low coherence interferometry'

Coote JM, Alles EJ, Noimark S, Mosse S, Little CD, Loder CD, Rakhit RD, Finlay MC, Desjardins AE (2019). *Optics Express* https://doi.org/10.1364/OE.27.005641 [2]

'All-Optical Ultrasound: A new platform for intracoronary imaging'

Little CD, Colchester RJ, Manmathan G, Rakhit RD, Desjardins AE (2020). *Journal of the American College of Cardiology.* https://doi.org/10.1016/S0735-1097(20)31975-6 [137]

'Optically generated ultrasound for intracoronary imaging'

Little CD, Colchester RJ, Noimark S, Manmathan G, Finlay MC, Desjardins AE, Rakhit RD (2020). *Frontiers in Cardiovascular Medicine* https://doi.org/10.3389/fcvm.2020.525530 [135]

'Flexible and directional fibre optic ultrasound transmitters using photostable dyes'

Colchester RJ, Little CD, Alles E, Desjardins AE (2021). *OSA Continuum* https://doi.org/10.1364/OSAC.431444 [1]

'A Patient-Specific Abdominal Aortic Aneurysm multi-modality imaging phantom'

Little CD, Mackle EC, Maneas E, Chong D, Mastraccia TM, Desjardins AE, (2022). *International Journal of Computer Assisted Radiology and Surgery* https://doi.org/10.1007/s11548-022-02612-4

7.2 Presentations

Vascular Imaging with All-Optical Ultrasound Imaging: A Preliminary Comparison with Optical Coherence Tomography and Electronic Intravascular Ultrasound

Optics in Cardiology, Rotterdam 2017. Awarded Honorary Commendation

Two-photon polymerization 3D printing of phantoms for intravascular optical coherence tomography Optics in Cardiology, Zurich 2018

Complex wall-less anatomical vascular ultrasound imaging phantoms

European Society Vascular Surgery (ESVS) Spring Meeting, London 2019

All-optical ultrasound as a guide for in-situ fenestration during FEVAR

European Society Vascular Surgery (ESVS) Spring Meeting, London 2019

A hybrid approach of two-photon polymerization scaffold printing and microinjection of optically heterogenous material for the fabrication of vascular imaging phantoms

Photonics West (SPIE BioS), San Francisco 2019

Optically generated ultrasound and contact sensing as a guide for optically delivered in-situ fenestration, using a custom-built device, during FEVAR of abdominal aortic aneurysms

British Vascular Society (BVS) Annual Scientific Meeting, Manchester 2019. Finalist in the BJS prize (best scientific oral presentation)

All-Optical ultrasound: A new platform for intracoronary imaging

American College of Cardiology (ACC) World Congress, Virtual 2020

Optical ultrasound; A new imaging paradigm allowing real time visualization of in-situ fenestration of aortic endovascular grafts during aneurysm repair

TCT, Virtual 2020

Optical ultrasound (OpUS): a novel concept for intravascular imaging

European Society of Cardiology (ESC) Congress, Virtual 2020

All-Optical ultrasound: A new paradigm in intra-vascular imaging

*EuroPCR, Paris 2020. *Cancelled due to COVID-19*

Appendix A

Protocol for In-vivo experiments

A.1 Introduction

Aneurysms (localised dilatation of a vessel $>$ 1.5 times the reference diameter) of the Abdominal Aorta (AAA) affect up to 1.3% of men in the UK aged between 65-74 years. Without treatment, in those with large (¿5.5cm) or rapidly expanding AAAs, there is a significant annual risk of aneurysmal rupture with potentially fatal consequences. Endovascular treatment using covered stents is often preferred to open abdominal surgery in order to decrease hospital stay and facilitate earlier recovery. Juxtarenal AAAs (AAAs extending to within 10mm of the origin of the renal arteries) offer a significant challenge for EVAR as there may be insufficient room to deploy the stent without obstructing flow of blood to the kidneys. For these pre-fenestrated grafts can be an option, however they are expensive, have a long manufacturing lead time and may not be suitable for all anatomical variants. In-situ fenestration (ISF), the process by which fenestrations are created in the stent at time of surgery, may provide an attractive alternative as it has the potential to offer preservation of flow to aortic side-branches regardless of anatomy and in a timely and cost-effective manner. Several methods have been proposed for ISF, however to date there are no devices that have been specifically developed for this application. Challenges of ISF include 1) Locating the side-branches of interest 2) Generating reproducible fenestrations and 3) minimising damage to surrounding tissues. We have developed an entirely new family of miniaturised optical based in-

travascular imaging devices ideally suited to minimally-invasive procedures. These are incorporated into an imaging probe suitable for easy delivery to vascular structures during EVAR procedures, plus an associated console. Imaging is performed using optically generated ultrasound (OpUS) using the photoacoustic effect facilitated by custom nanocomposite coatings. These coatings absorb light at selective wavelengths allowing both generation of ultrasound for imaging and delivery of light to the stent material for laser fenestration.

A.2 Aims

i) To use OpUS to demonstrate vascular structures, such as endothelium and side-branches, through a covered endovascular stent.
ii) To use OpUS to detect a suitable site for ISF and to demonstrate the selective absorption of the nanocomposite material by creating a laser generated ISF (wavelength 808nm)

A.3 Objectives

A. Femoral
i. Obtain bilateral femoral artery access with insertion of 12Fr Sheaths (Ultrasound guidance and arterial cut-down as required)
ii. Deployment of a covered endovascular stent from the Aorta to the left Femoral artery
iii. OpUS imaging of the endovascular stent from the right Femoral artery
iv. ISF using 808nm laser of endovascular stent and subsequent fenestration dilatation
B. Abdominal Aorta
i. OpUS imaging of the abdominal aorta and renal arteries
ii. Deployment of an EVAR in the abdominal aorta and subsequent OpUS guided ISF of both renal arteries

A.4 Pre-Experimental planning

A.4.1 Regulatory Guidelines

The UK Home Office controls scientific procedures on animals in the UK and does so by the issue of licences under the Animal (Scientific Procedures) Act 1986. The regulations conform to the European Convention for the Protection of Vertebrate Animals Used for Experimental and Other Scientific Purposes (Strasbourg, Council of Europe), and achieves the standard of care required by the US Department of Health and Human Services Guide for the Care and the Use of Laboratory Animals. The Home Office Project Licence governing this study (Project Licence - PPL: P14B07C34; Protocol Number: 1) directly specifies the limits of severity of effects on the animals. No formal claim of Good Laboratory Practice (GLP) compliance is made. The study will be conducted in accordance with the standards of the Test Facility.

A.4.2 Study Identification

All documents and preparations created during this study will be marked with Test Facility study number UCL.CL.02.21.

A.4.3 Report

Depending on the requirements of the Sponsor, either a summary report will be submitted to the Sponsor, which will include the procedures carried out during the study period and the raw data presented only as tables in the appendices; or a report consisting of the procedures carried out during the study period, including the analysis of the raw data in the results section, and any raw data presented as tables in the appendices.

A.4.4 Records to be Maintained

All measurements, observations and unanticipated events, including adverse events and protocol amendments and deviations, will be recorded on the appropriate forms and stored in the study file.

A.4.5 Storage of Records

On completion of the study, any raw data will be stored for a period of three years, after which, the Sponsor will be contacted to ascertain further retention requirements, the options being to archive all tissue at the Sponsor nominated facility, to continue storing at the Test Facility.

A.4.6 Standard Operating Procedures (SOPs)

Unless specified, all procedures described in the protocol are the subject of detailed SOPs which are contained in the SOP manuals of the operating departments of the Test Facility.

A.4.7 Protocol Amendments

Any amendments to this protocol will be justified, documented and approved by the Study Director and Sponsor prior to implementation, in the form of a study note.

A.4.8 Protocol Deviations

Any deviations to this protocol will be assessed for the impact to the study, then documented on a study note and approved by the Study Director.

A.4.9 Test Device

The test device is Tourguide steerable sheath (Medtronic) with an inner custom built imaging (OpUS)/fenestration probe. The sponsor will provide and prepare all test devices. There are no specific requirements for handling or storage.

A.4.10 Animal Details

Number and Sex: 2 Female

Species and Breed: Large white/Landrace crossbred pig (Sus scrofa domestica)

Supplier: DJ and J Witherick and Sons, Winsey, Park Lane, Sharnbrook, Bedfordshire, MK44 1NA

Arrival Date: At least 7 days prior to surgery

Expected body weight on arrival: $>$70 kg: a large aorta diameter is ideal and the Sponsor requests pigs as large as possible, subject to availability.

Acclimatisation period: At least 7 days prior to surgery

Selection for Study: Examined for general health status by the NACWO shortly after arrival, before inclusion into the study

A.4.11 Justification for Choice of Species and Number on Study

The swine model is a human sized animal suitable with physical and vascular dimensions highly similar to humans. The vascular sizes and catheters available are optimised for human use therefore swine species are highly equivalent. The investigators have prior experience of using swines for device testing and these provide a highly reproducible and accepted model of device behaviour in the pre-clinical setting.

A.4.12 Humane End-Points

If any animal experiences pain, suffering distress or lasting harm, that takes it to the limits of the severity banding for the project licence and cannot be alleviated by any interventional procedure, it will therefore be deemed incompatible with life, and the animal will be terminated following a unanimous decision between the Named Animal Care and Welfare Officer (NACWO), surgeon, Study Director, NVS (if required) and other appropriate personnel. If in the unforeseeable event the animal does not survive the complete procedure, the same method for termination will be carried out for the unscheduled terminations, and the animal will only be replaced after discussion with the Study Director and NACWO.

A.4.13 Husbandry Details

Accommodation: Group housed on arrival. Then singly housed prior to surgery.

Bedding: Concrete pen with straw

Light Cycle: Automatically controlled with 12 hours light/ 12 hours dark.

Temperature: Ambient (target range: 15-24C)

Relative Humidity: Target range: 40-70%

Basal Diet: Pig Grower Pellets (Country Farm; Supplier: Lillico and Sons) provided once daily

Water: Available ad libitum. Supplier: Three Valleys Water

Basal Diet Contaminants: No known substances are expected in the diet at levels

which might adversely affect the results of the study.

Water Contaminants: No known substances are expected in the drinking water at levels which might adversely affect the results of the study.

A.5 Experimental Procedure

A.5.1 Study Design

The study will comprise of 2 animals. Each experiment will be performed under non-recovery anaesthesia over one day and the animals will be killed at the end of the experiment.

A.5.1.1 Instruments

The details for the instrument(s) to be used in this study are: Description Tourguide steerable sheath (Medtronic) with an inner custom built imaging (OpUS)/fenestration probe.

A.5.2 Procedures Pre-Surgery

The animals will be weighed 1 day prior to surgery. The general health of the animals will be observed by husbandry staff and any problems or concerns will be reported to the NACWO and Study Director.

A.5.2.1 Anaesthesia

For each animal: Diazepam tablets (10 mg/10kg) and Acepromazine (ACP) tablets (10 mg/10kg) will be administered orally in a piece of fruit or vegetable, approximately 30-60 minutes prior to other administrations. Pre-medication: Ketamine (5 mg/kg)/ Xylazine (1 mg/kg) will be administered intramuscularly. General anaesthesia will be induced with oxygen over Isoflurane, delivered via a close fitting face mask. The animal will be transferred to the appropriate operating theatre. The animal will be intubated with a cuffed endotracheal tube. After intubation, anaesthesia will be maintained using oxygen over isoflurane, with respiration controlled via a ventilator. Oxygen saturation, pulse rate, rectal/oesophageal temperature, expired CO2 and respiratory rate will be measured and recorded.

A.5.2.2 Preparation

For each animal: The analgesic Carprofen (4 mg/kg) will be administered subcutaneously. A continuous intravenous drip of Hartmann's solution (Baxter) will be delivered via a peripheral vein throughout the procedure. Animals will be clipped of hair from the femoral triangles. The exposed skin will be cleaned with Chlorhexidine (Animal Care Ltd). The animal will be covered with sterile drapes in such a way, so as to leave only the operative site exposed. All procedures will be performed using aseptic technique from this point on. A cutdown will be performed on right and left side to access right and left femoral veins and arteries, insertion of vessel sheath(s) and arterial lines with Ultrasound guidance.

A.6 Surgical Procedure

A.6.1 OpUS imaging of vascular structures - In-vivo 1 & 2

i) 5Fr Pigtail catheter inserted into the Aortic root through the Right Femoral Artery (RFA) and used to perform an aortogram to act as a roadmap for further procedures. 5Fr Pigtail then removed.

ii) JR4 6Fr guide inserted through the RFA and used to cannulated both the right coronary artery (RCA).

iii) Angiogram of RCA taken for use as a roadmap

iv) Delivery of OpUS probe to the proximal RCA using a tourguide 7Fr steerable catheter via the RFA.

v) OpUS imaging of the prox RCA.

vi) OpUS probe repositioned via the tourguide catheter to image the Aortic valve

A.6.2 Femoral EVAR ISF - In-vivo 1

i) 5Fr Pigtail catheter inserted into the Aorta through the Right Femoral Artery (RFA) and used to perform an aortogram to act as a roadmap for further procedures. 5Fr Pigtail then removed.

ii) JR4 6Fr guide inserted through the Left Femoral Artery (LFA) and used to cannulated both the left and right renal arteries. These are wired using a J-tip 0.035

inch 260cm exchange guidewire.

iii) An EVAR stent of suitable size (i.e 2x10cm) deployed from the Aorta into the left femoral artery.

iv) Delivery of OpUS probe to the stent using a tourguide 7Fr steerable catheter via the RFA.

v) OpUS imaging of the EVAR stent.

vi) ISF of stent using 808nm laser

vii) Repeat OpUS imaging of stent

viii) 0.018 coronary wire passed through the fenestration to the aorta

ix) Fenestration post dilated with non-compliant balloons (2mm, 2.5mm, 3mm, 4mm)

x) Aortogram performed at level of iliac arteries with 5Fr pigtail inserted in LFA

A.6.3 Abdominal Aorta EVAR ISF - In-vivo 2

i) An EVAR stent of suitable size (i.e 4x12cm) deployed in the Aorta at the level of the renal arteries. Inserted via the LFA.

ii) Delivery of OpUS probe to the stent using a tourguide 7Fr steerable catheter via the LFA.

iii) OpUS imaging of the EVAR stent to detect renal artery (left or right)

iv) ISF of stent into renal artery using 808nm laser

v) Repeat OpUS imaging of stent

vi) 0.018 coronary wire passed through the fenestration to the renal artery

viii) Fenestration post dilated with non-compliant balloons (2mm, 2.5mm, 3mm)

ix) Aortogram performed at level of renal arteries with 5Fr pigtail inserted in LFA.

A.6.4 Termination

Sodium pentobarbitone (140 mg/kg) will be administered intravenously. A representative sample of: Iliac and Aortic tissue will be removed and stored in 10% neutral buffered formalin (NBF) for histology. All observations will be recorded on the post-mortem examination form.

A.6.5 Safety

All necessary precautions listed in the associated SOPs will be adhered to.

Appendix B

Histology results from in-vivo ISF procedures

B.1 Sample A - Healthy Control

This sample has been serially sectioned 6 times (A1-6). Three of the sections (1, 5, 6) have variably deep areas of tissue loss and clefting at the luminal aspect of the vessel, with multifocal loss of elastin/collagen structure at the edge. The deepest and widest of these lesions is 1.2mm deep by 1.12mm wide (section A5).

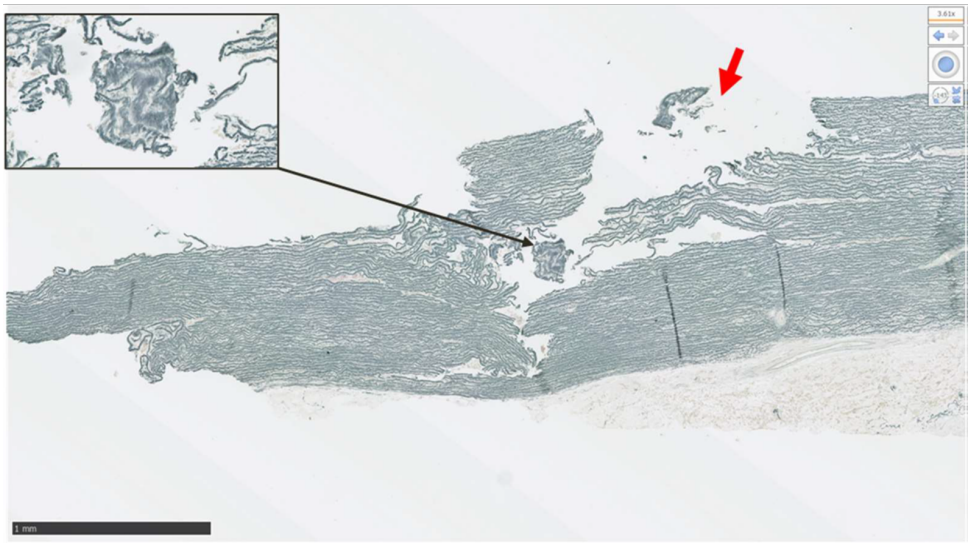

Figure B.1: Section A5

Elastic Van Giesson. The red arrow indicates the surface an area of deep clefting of the vessel, with multifocal elastin/collagen disruption (inset). Scale bar: 1mm.

B.2 Sample B - Diseased Control

This sample has been serially sectioned 5 times (B1-5). Four of the sections (1, 2, 4, 5) have lesions which involve mild superficial tissue loss (1), intramural elastin/collagen degeneration without tissue loss (2), and intramural cavitation with superficial elastin/collagen degeneration (5). The area of tissue loss in (4) is interpreted as a sectioning artefact, in the absence of elastin degeneration. The deepest of these lesions is 1.14mm deep by 1.91mm wide (section B2). This is also distinct from the rest, as it features a mural lesion that does not involve the surface of the vessel. Conversely, other lesions of this same sample involve superficial tissue loss (B1) or elastin degeneration (B2), but these are superficial.

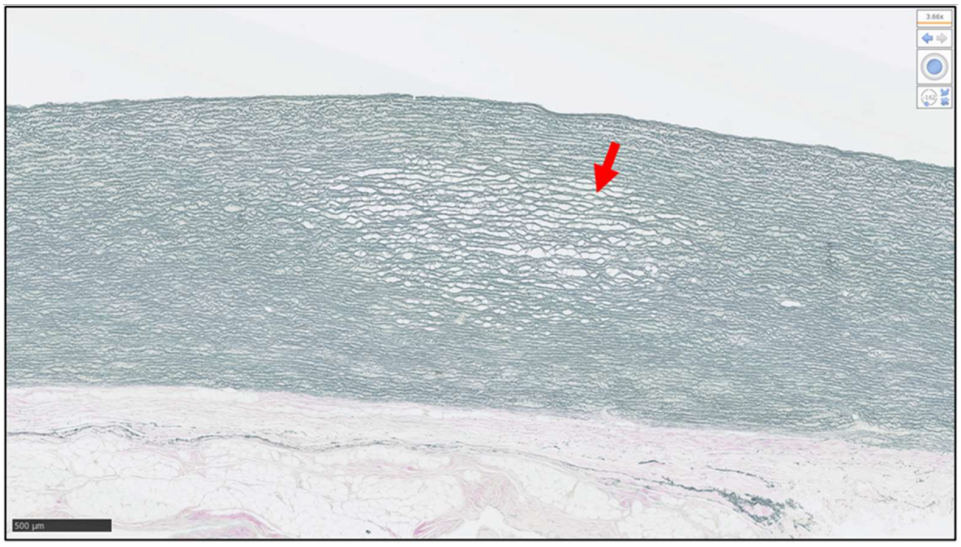

Figure B.2: Section B2

Elastic Van Giesson. The red arrow indicates an intramural area of elastin/collagen disruption without damage to the intimal surface. Scale bar: 0.5mm.

B.3 Sample C - Diseased Control

This sample has been serially sectioned 6 times (C1-5). Two of the sections (1, 3) present with lesions that involve vessel clefting without elastin/collagen degeneration (C1, interpreted as an artefact), and intramural elastin/collagen degeneration with evidence of adventitial cauterization (C3), suggesting the injury was administered from the adventitial side. This lesion is 0.92mm deep (reaching the outer

aspect of the vessel), and 2.81mm wide. It is not associated with damage to the intimal aspect of the vessel.

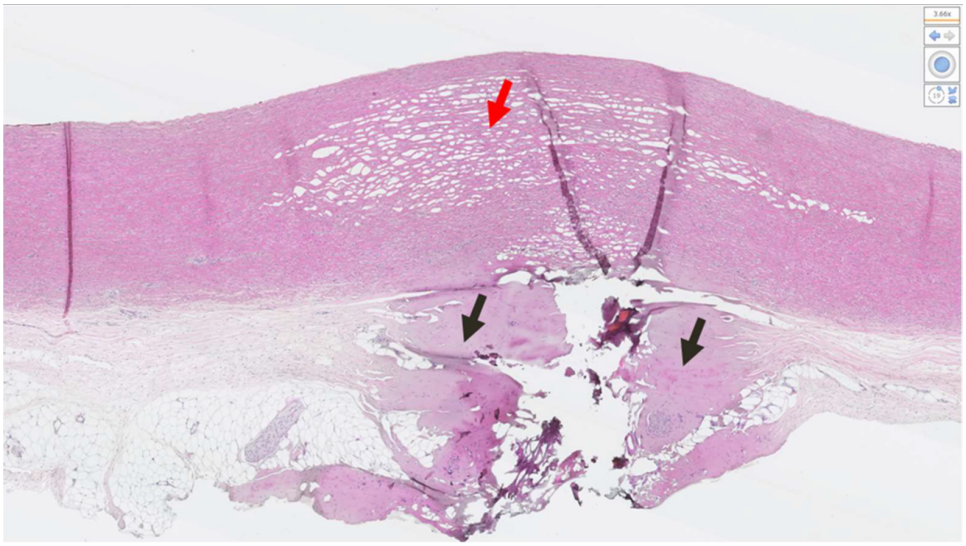

Figure B.3: Section C3

Haematoxylin and Eosin. The red arrow indicates an intramural area of focal elastin disruption, whereas the black arrows indicate adventitial cauterized areas. The intimal surface of the vessel is not affected.

B.4 Sample D - Healthy Control

This sample has been serially sectioned 5 times (D1-5). One of the sections (1) presents with a lesion that involves tissue loss at the luminal aspect of the vessel. This is not associated with elastin/collagen degeneration, and may be artefactual. This lesion is 0.45mm deep, and 4.09mm wide.

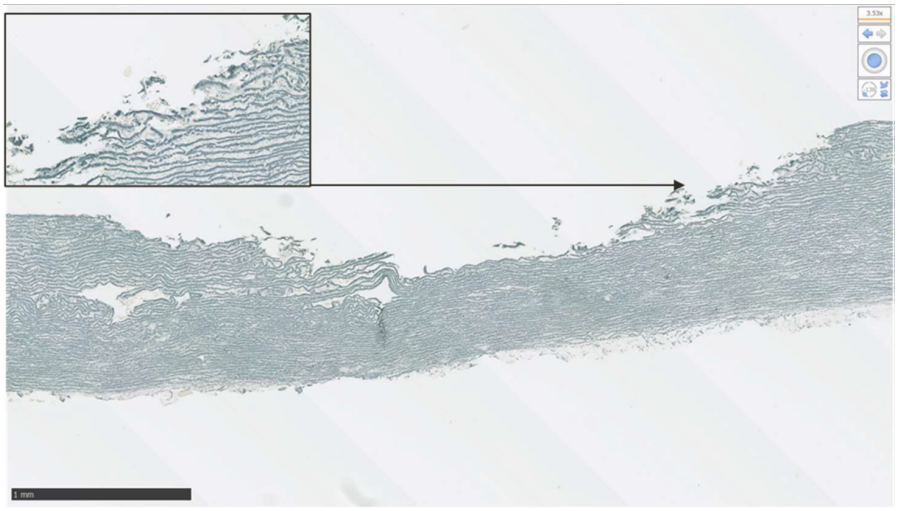

Figure B.4: Section D1

Elastic Van Giesson. There is an area of mural tissue loss at the centre of the sample. Inset: this is not associated with elastin/collagen disruption. Scale bar: 1mm.

B.5 Sample E - In Vivo 1

This sample has been serially sectioned 6 times (E1-6). One of the sections (1) presents with a lesion that involves tissue loss at the luminal aspect of the vessel without elastin/collagen degeneration (may be artefactual). This lesion is located at the edge of the sample and is 0.42mm deep, and 1.75mm wide.

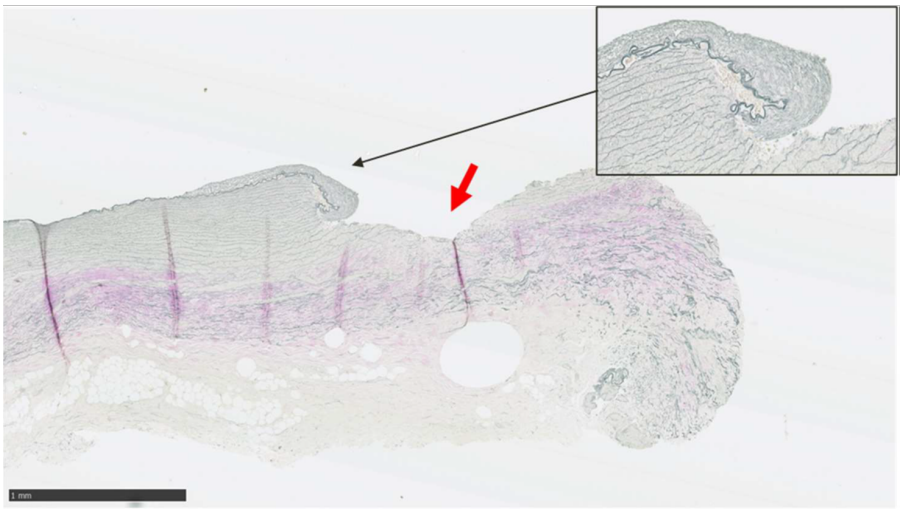

Figure B.5: Section E1

Elastic Van Giesson. There is an area of mural tissue loss at the edge of the sample. Inset: this is not associated with elastin/collagen disruption. Scale bar: 1mm.

B.6 Sample F - In Vivo 1

This sample has been serially sectioned 5 times (F1-5). There is no evidence of cauterization injury in any of the sections examined.

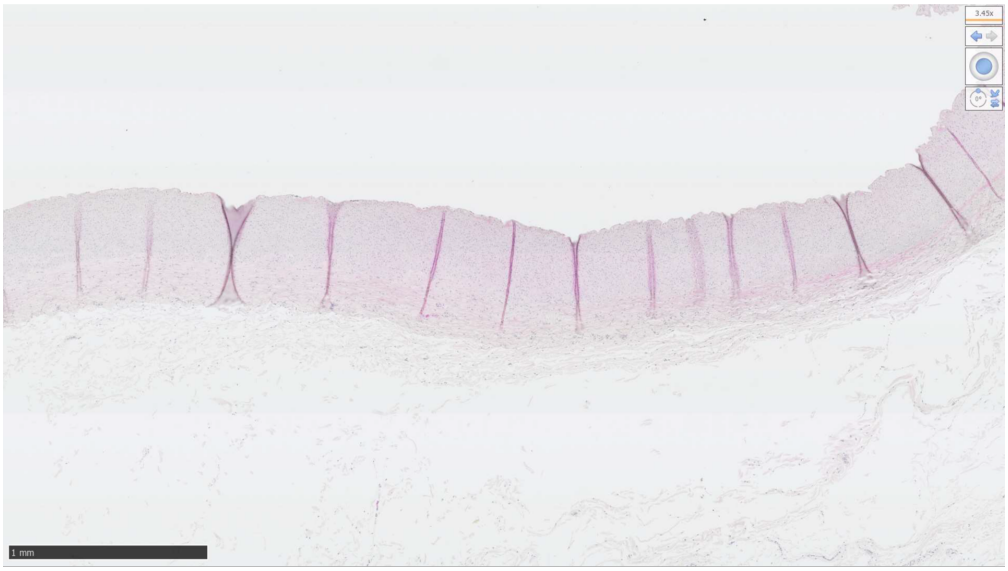

Figure B.6: Section F1

Haematoxylin and Eosin. This section of aorta is histologically normal. Scale bar: 1mm.

B.7 Sample G - In Vivo 2

This sample has been serially sectioned 4 times (G1-4). Section G2 presents with a thin mural lesion that involves a narrow cleft containing degenerate tissue. This lesion is 0.17mm deep and 0.76cm wide.

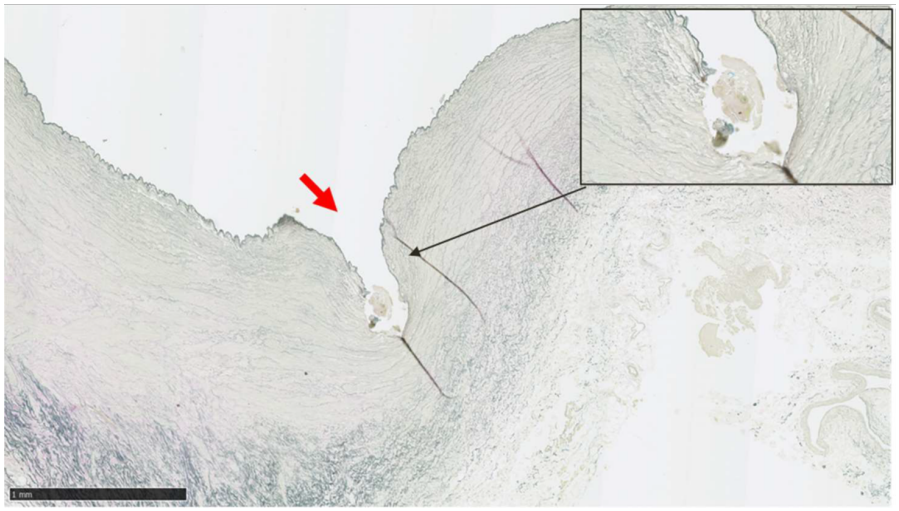

Figure B.7: Section G2

Elastic Van Giesson. There is a focal area of vessel clefting with an intraluminal aggregate of degenerate tissue. Scale bar: 1mm.

B.8 Sample H - In Vivo 2

This sample has been serially sectioned 4 times (H1-4). Section H3 has been re-orientated to improve the examination and measurement of the lesion present within it, which is the only lesion in sample H. This lesion involves elastin/collagen degeneration and haemorrhage without intimal involvement. This lesion is 1.35mm deep and 2.39cm wide.

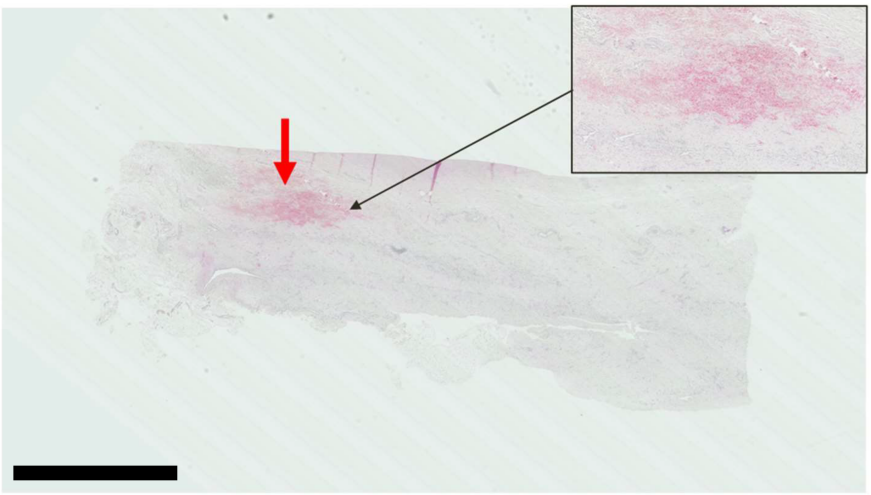

Figure B.8: Section H1

Haematoxylin and Eosin. There is an intramural lesion that is haemorrhagic and features elastin/collagen degeneration. Scale bar: 1mm.

Figure B.9: Summary of sample histology

Pathology n	Serial sections	Pot	Study	Animal	Aorta	Lesion	Elastin disruption	Mural tissue loss	Lesion depth	Lesion width
P9915	A1	Pot1	UCL.CL.02.21	CL02	A	Yes	Yes	Yes	0.51	2.44
P9915	A2	Pot1	UCL.CL.02.21	CL02	A	No	No	No		
P9915	A3	Pot1	UCL.CL.02.21	CL02	A	No	No	No		
P9915	A4	Pot1	UCL.CL.02.21	CL02	A	No	No	No		
P9915	A5	Pot1	UCL.CL.02.21	CL02	A	Yes	Yes	Yes	1.2	1.12
P9915	A6	Pot1	UCL.CL.02.21	CL02	A	Yes	Yes	Yes	0.94	unmeasurable
P9915	B1	Pot1	UCL.CL.02.21	CL02	B	Yes	Yes	Yes	0.14	2.63
P9915	B2	Pot1	UCL.CL.02.21	CL02	B	Yes	Yes	No	1.14	1.91
P9915	B3	Pot1	UCL.CL.02.21	CL02	B	No	No	No		
P9915	B4	Pot1	UCL.CL.02.21	CL02	B	Yes	No	Yes	0.48	6.13
P9915	B5	Pot1	UCL.CL.02.21	CL02	B	Yes	Yes	No	0.29	3.72
P9915	C1	Pot3	UCL.CL.02.21	CL02	C	Yes	No	No		
P9915	C2	Pot3	UCL.CL.02.21	CL02	C	No	No	No		
P9915	C3	Pot3	UCL.CL.02.21	CL02	C	Yes	Yes	No	0.92	2.81
P9915	C4	Pot3	UCL.CL.02.21	CL02	C	No	No	No		
P9915	C5	Pot3	UCL.CL.02.21	CL02	C	No	No	No		
P9915	C6	Pot3	UCL.CL.02.21	CL02	C	No	No	No		
P9915	D1	Pot4	UCL.CL.02.21	CL02	D	Yes	Yes	Yes	0.45	4.09
P9915	D2	Pot4	UCL.CL.02.21	CL02	D	No	No	No		
P9915	D3	Pot4	UCL.CL.02.21	CL02	D	No	No	No		
P9915	D4	Pot4	UCL.CL.02.21	CL02	D	No	No	No		
P9915	D5	Pot4	UCL.CL.02.21	CL02	D	No	No	No		
P9915	E1	Pot5	UCL.CL.02.21	CL02	E	Yes	Yes	Yes	0.42	1.75
P9915	E2	Pot5	UCL.CL.02.21	CL02	E	No	No	No		
P9915	E3	Pot5	UCL.CL.02.21	CL02	E	No	No	No		
P9915	E4	Pot5	UCL.CL.02.21	CL02	E	No	No	No		
P9915	E5	Pot5	UCL.CL.02.21	CL02	E	No	No	No		
P9915	E6	Pot5	UCL.CL.02.21	CL02	E	No	No	No		
P9915	F1	Pot6	UCL.CL.02.21	CL02	F	No	No	No		
P9915	F2	Pot6	UCL.CL.02.21	CL02	F	No	No	No		
P9915	F3	Pot6	UCL.CL.02.21	CL02	F	No	No	No		
P9915	F4	Pot6	UCL.CL.02.21	CL02	F	No	No	No		
P9915	F5	Pot6	UCL.CL.02.21	CL02	F	No	No	No		
P9916	G1	Pot1	UCL.CL.2nd study	Unknown	G	No	No	No		
P9916	G2	Pot1	UCL.CL.2nd study	Unknown	G	Yes	No	No	0.17	0.76
P9916	G3	Pot1	UCL.CL.2nd study	Unknown	G	No	No	No		
P9916	G4	Pot1	UCL.CL.2nd study	Unknown	G	No	No	No		
P9916	H1	Pot2	UCL.CL.2nd study	Unknown	H	No	No	No		
P9916	H2	Pot2	UCL.CL.2nd study	Unknown	H	No	No	No		
P9916	H3	Pot2	UCL.CL.2nd study	Unknown	H	Yes	Yes	No	1.35	2.39
P9916	H4	Pot2	UCL.CL.2nd study	Unknown	H	No	No	No		

Bibliography

[1] Richard J. Colchester, Callum D. Little, Erwin J. Alles, and Adrien E. Desjardins. Flexible and directional fibre optic ultrasound transmitters using photostable dyes. *OSA Continuum*, 4(9), 2021.

[2] Joanna. M. Coote, Erwin. J. Alles, Sacha. Noimark, Charles. A. Mosse, Callum. D. Little, Chris. D. Loder, Anna. L. David, Roby. D. Rakhit, Malcolm. C. Finlay, and Adrien. E. Desjardins. Dynamic physiological temperature and pressure sensing with phase-resolved low-coherence interferometry. *Optics Express*, 27(4):5641–5654, 2019.

[3] Alexander Ng and Justiaan Swanevelder. Resolution in ultrasound imaging. *Continuing Education in Anaesthesia, Critical Care and Pain*, 11(5):186–192, 2011.

[4] Paul G. Yock, David T. Linker, Bjoern A.J. Angelsen, and Tech. Two-Dimensional Intravascular Ultrasound: Technical Development and Initial Clinical Experience. *Journal of the American Society of Echocardiography*, 2(4):296–304, 1989.

[5] Sudheer Koganti, Tushar Kotecha, and Roby D. Rakhit. Choice of intracoronary imaging: When to use intravascular ultrasound or optical coherence tomography. *Interventional Cardiology Review*, 11(1):11–16, 2016.

[6] Michael F. Bode and Farouc A. Jaffer. IVUS and OCT: Current State-of-the-Art in Intravascular Coronary Imaging. *Current Cardiovascular Imaging Reports*, 12(7), 2019.

[7] Xiao Fei Gao, Zhi Mei Wang, Feng Wang, Yue Gu, Zhen Ge, Xiang Quan Kong, Guang Feng Zuo, Jun Jie Zhang, and Shao Liang Chen. Intravascular ultrasound guidance reduces cardiac death and coronary revascularization in patients undergoing drug-eluting stent implantation: results from a meta-analysis of 9 randomized trials and 4724 patients. *International Journal of Cardiovascular Imaging*, 35(2):239–247, 2019.

[8] Yue Wang, Gary S. Mintz, Zhichun Gu, Yue Qi, Yue Wang, Mengru Liu, and Xiaofan Wu. Meta-analysis and systematic review of intravascular ultrasound versus angiography-guided drug eluting stent implantation in left main coronary disease in 4592 patients. *BMC Cardiovascular Disorders*, 18(1):1–11, 2018.

[9] I. Porto, S. MacDonald, and A. P. Banning. Intravascular ultrasound as a significant tool for diagnosis and management of coronary aneurysms. *CardioVascular and Interventional Radiology*, 27(6):666–668, 2004.

[10] Hisao Kumakura, Hiroyoshi Kanai, Yoshihiro Araki, Yoshiaki Hojo, Toshiya Iwasaki, and Shuichi Ichikawa. 15-Year Patency and Life Expectancy after Primary Stenting Guided by Intravascular Ultrasound for Iliac Artery Lesions in Peripheral Arterial Disease. *JACC: Cardiovascular Interventions*, 8(14):1893–1901, 2015.

[11] Azfar Bilal Sheikh, Mahesh Anantha-Narayanan, Kim G. Smolderen, Qurat Ul Ain Jelani, Sameer Nagpal, Marabel Schneider, Fiorella Llanos, Costin Ionescu, Christopher Regan, Robert Attaran, S. Elissa Altin, and Carlos Mena-Hurtado. Utility of Intravascular Ultrasound in Peripheral Vascular Interventions: Systematic Review and Meta-Analysis. *Vascular and Endovascular Surgery*, 54(5):413–422, 2020.

[12] S. Raju, A. Martin, and M. Davis. The Importance of IVUS Assessment in Venous Thrombolytic Regimens. *Journal of Vascular Surgery: Venous and Lymphatic Disorders*, 1(1):108, 2013.

[13] Felice Pecoraro, Umberto M. Bracale, Arduino Farina, Giovanni Badalamenti, Francesca Ferlito, Mario Lachat, Ettore Dinoto, Vincenzo Asti, and Guido Bajardi. Single-Center Experience and Preliminary Results of Intravascular Ultrasound in Endovascular Aneurysm Repair. *Annals of Vascular Surgery*, 56:209–215, 2019.

[14] Coskun Tekes, Mustafa Karaman, and F. Levent Degertekin. Optimizing circular ring arrays for forward-looking IVUS imaging. *IEEE Transactions on Ultrasonics, Ferroelectrics, and Frequency Control*, 58(12):2596–2607, 2011.

[15] Seungmok Lee and Junji Ikeda. A Study of an Annular Array CMUT Device for the making of Forward Looking IVUS. In *IEEE International Ultrasonics Symposium, IUS*, pages 1–4, 2021.

[16] David Huang, Eric A. Swanson, Charles P. Lin, Joel S. Schuman, William G. Stinson, Warren Chang, Michael R. Hee, Thomas Flotte, Kenton Gregory, Carmen A. Puliafito, and James G. Fujimoto. Optical coherence tomography. *Science*, 254(5035):1178–1181, 1991.

[17] Sharonne N. Hayes, Chair Esther S.H. Kim, Jacqueline Saw, David Adlam, Cynthia Arslanian-Engoren, Katherine E. Economy, Santhi K. Ganesh, Rajiv Gulati, Mark E. Lindsay, Jennifer H. Mieres, Sahar Naderi, Svati Shah, David E. Thaler, Marysia S. Tweet, and Malissa J. Wood. Spontaneous coronary artery dissection: Current state of the science: A scientific statement from the American Heart Association. *Circulation*, 137(19):523–557, 2018.

[18] Ankush Gupta, Sanya Chhikara, Rajesh Vijayvergiya, Ashok Seth, Nalin K. Mahesh, Takashi Akasaka, and Navreet Singh. Saline as an alternative to radio-contrast for optical coherence tomography guided percutaneous coronary intervention: A prospective comparison. *Cardiovascular Revascularization Medicine*, 34:86–91, 2021.

[19] Tianshi Wang, Tom Pfeiffer, Evelyn Regar, Wolfgang Wieser, Heleen van Beusekom, Charles T. Lancee, Geert Springeling, Ilona Krabbendam, Antonius F.W. van der Steen, Robert Huber, and Gijs van Soest. Heartbeat OCT: in vivo intravascular megahertz-optical coherence tomography. *Biomedical Optics Express*, 6(12):5021–5032, 2015.

[20] Ziad A. Ali, Akiko Maehara, Philippe Généreux, Richard A. Shlofmitz, Franco Fabbiocchi, Tamim M. Nazif, Giulio Guagliumi, Perwaiz M. Meraj, Fernando Alfonso, Habib Samady, Takashi Akasaka, Eric B. Carlson, Massoud A. Leesar, Mitsuaki Matsumura, Melek Ozgu Ozan, Gary S. Mintz, Ori Ben-Yehuda, and Gregg W. Stone. Optical coherence tomography compared with intravascular ultrasound and with angiography to guide coronary stent implantation (ILUMIEN III: OPTIMIZE PCI): a randomised controlled trial. *The Lancet*, 388(10060):2618–2628, 2016.

[21] Daniel A. Jones, Krishnaraj S. Rathod, Sudheer Koganti, Stephen Hamshere, Zoe Astroulakis, Pitt Lim, Alexander Sirker, Constantinos O'Mahony, Ajay K. Jain, Charles J. Knight, Miles C. Dalby, Iqbal S. Malik, Anthony Mathur, Roby Rakhit, Tim Lockie, Simon Redwood, Philip A. MacCarthy, Ranil Desilva, Roshan Weerackody, Andrew Wragg, Elliot J. Smith, and Christos V. Bourantas. Angiography Alone Versus Angiography Plus Optical Coherence Tomography to Guide Percutaneous Coronary Intervention: Outcomes From the Pan-London PCI Cohort. *JACC: Cardiovascular Interventions*, 11(14):1313–1321, 2018.

[22] Gregg W. Stone, Akiko Maehara, Alexandra J. Lansky, Bernard de Bruyne, Ecaterina Cristea, Gary S. Mintz, Roxana Mehran, John McPherson, Naim Farhat, Steven P. Marso, Helen Parise, Barry Templin, Roseann White, Zhen Zhang, and Patrick W. Serruys. A Prospective Natural-History Study of Coronary Atherosclerosis. *New England Journal of Medicine*, 364(3):226–235, 2011.

[23] Jin M. Cheng, Rohit M. Oemrawsingh, Hector M. Garcia-Garcia, Eric Boersma, Robert Jan van Geuns, Patrick W. Serruys, Isabella Kardys, and K. Martijn Akkerhuis. PCSK9 in relation to coronary plaque inflammation: Results of the ATHEROREMO-IVUS study. *Atherosclerosis*, 248:117–122, 2016.

[24] Krista Jansen, Antonius F. W. van der Steen, Heleen M. M. van Beusekom, J. Wolter Oosterhuis, and Gijs van Soest. Intravascular photoacoustic imaging of human coronary atherosclerosis. *Optics Letters*, 36(5):597–599, 2011.

[25] Sophinese Iskander-Rizk, Min Wu, Geert Springeling, Heleen M.M. van Beusekom, Frits Mastik, Maaike te Lintel Hekkert, Robert H.S.H. Beurskens, Ayla Hoogendoorn, Eline M.J. Hartman, Antonius F.W. van der Steen, Jolanda J. Wentzel, and Gijs van Soest. In vivo intravascular photoacoustic imaging of plaque lipid in coronary atherosclerosis. *EuroIntervention*, 15(5):452–456, 2019.

[26] David Erlinge, Akiko Maehara, Ori Ben-Yehuda, Hans Erik Bøtker, Michael Maeng, Lars Kjøller-Hansen, Thomas Engstrøm, Mitsuaki Matsumura, Aaron Crowley, Ovidiu Dressler, Gary S. Mintz, Ole Fröbert, Jonas Persson, Rune Wiseth, Alf Inge Larsen, Lisette Okkels Jensen, Jan Erik Nordrehaug, Øyvind Bleie, Elmir Omerovic, Claes Held, Stefan K. James, Ziad A. Ali, James E. Muller, Gregg W. Stone, Ole Ahlehoff, Azad Amin, Oskar Angerås, Praveen Appikonda, Saranya Balachandran, Ståle Barvik, Kristoffer Bendix, Maria Bertilsson, Ulrika Boden, Nigussie Bogale, Vernon Bonarjee, Fredrik Calais, Jörg Carlsson, Steen Carstensen, Christina Christersson, Evald Høj Christiansen, Maria Corral, Ole De Backer, Usama Dhaha, Christian Dworeck, Kai Eggers, Charlotta Elfström, Julia Ellert, Erlend Eriksen, Christian Fallesen, Margareta Forsman, Helena Fransson, Mohsen Gaballa, Marek Gacki, Matthias Götberg, Lars Hagström, Theresa Hallberg, Kristina Hambraeus, Inger Haraldsson, Jan Harnek, Ole Havndrup, Knut Hegbom, Matthias Heigert, Steffen Helqvist, Jon Herstad, Ziad Hijazi, Lene Holm-

vang, Dan Ioanes, Amjid Iqbal, Allan Iversen, Jaclyn Jacobson, Lars Jakobsen, Ivana Jankovic, Ulf Jensen, Karin Jensevik, Nina Johnston, Torfi Fjalar Jonasson, Erik Jørgensen, Francis Joshi, Ulf Kajermo, Frida Kåver, Henning Kelbæk, Thomas Kellerth, Mitra Kish, Wolfgang Koenig, Sasha Koul, Bo Lagerqvist, Bertil Larsson, Jens Flensted Lassen, Olav Leiren, Zhe Li, Christer Lidell, Rikard Linder, Michael Lindstaedt, Gunilla Lindström, Shen Liu, Kjetil Halvorsen Løland, Jacob Lønborg, László Márton, Habib Mir-Akbari, Shameema Mohamed, Jacob Odenstedt, Christer Ogne, Jonas Oldgren, Göran Olivecrona, Nikolas Östlund-Papadogeorgos, Michael Ottesen, Erik Packer, Åsa Michelgård Palmquist, Quratulain Paracha, Frans Pedersen, Petur Petursson, Truls Råmunddal, Svein Rotevatn, Raquel Sanchez, Giovanna Sarno, Kari I. Saunamäki, Fredrik Scherstén, Patrick W. Serruys, Iwar Sjögren, Rikke Sørensen, Iva Srdanovic, Zuka Subhani, Eva Svensson, Anne Thuesen, Jan Tijssen, Hans Henrik Tilsted, Tim Tödt, Thor Trovik, Bjørn Inge Våga, Christoph Varenhorst, Karsten Veien, Emma Vestman, Sebastian Völz, Lars Wallentin, Joanna Wykrzykowska, Leszek Zagozdzon, Manuela Zamfir, Crister Zedigh, Hang Zhong, and Zhipeng Zhou. Identification of vulnerable plaques and patients by intracoronary near-infrared spectroscopy and ultrasound (PROSPECT II): a prospective natural history study. *The Lancet*, 397(10278):985–995, 2021.

[27] Sunwon Kim, Min Woo Lee, Tae Shik Kim, Joon Woo Song, Hyeong Soo Nam, Han Saem Cho, Sun Joo Jang, Jiheun Ryu, Dong Joo Oh, Dae Gab Gweon, Seong Hwan Park, Kyeongsoon Park, Wang Yuhl Oh, Hongki Yoo, and Jin Won Kim. Intracoronary dual-modal optical coherence tomography-near-infrared fluorescence structural-molecular imaging with a clinical dose of indocyanine green for the assessment of high-risk plaques and stent-associated inflammation in a beating coronary artery. *European Heart Journal*, 37(37):2833–2844, 2016.

[28] Sanneke P.M. De Boer, Yael Baran, Hector M. Garcia-Garcia, Itamar Eskin, Mattie J. Lenzen, Marcus E. Kleber, Evelyn Regar, Peter J. De Jaegere,

Jurgen M. Ligthart, Robert Jan Van Geuns, Terho Lehtimäki, Reijo Laaksonen, Eric Boersma, Winfried März, Eran Halperin, Patrick W. Serruys, and Wolfgang Koenig. The European Collaborative Project on Inflammation and Vascular Wall Remodeling in Atherosclerosis - Intravascular Ultrasound (ATHEROREMO-IVUS) study. *EuroIntervention*, 14(2):194–203, 2018.

[29] Kenichiro Otsuka, Martin Villiger, Antonios Karanasos, Laurens J.C. van Zandvoort, Pallavi Doradla, Jian Ren, Norman Lippok, Joost Daemen, Roberto Diletti, Robert Jan van Geuns, Felix Zijlstra, Gijs van Soest, Jouke Dijkstra, Seemantini K. Nadkarni, Evelyn Regar, and Brett E. Bouma. Intravascular Polarimetry in Patients With Coronary Artery Disease. *JACC: Cardiovascular Imaging*, 13(3):790–801, 2020.

[30] Rohit M. Oemrawsingh, Jin M. Cheng, Héctor M. García-García, Robert Jan Van Geuns, Sanneke P.M. De Boer, Cihan Simsek, Isabella Kardys, Mattie J. Lenzen, Ron T. Van Domburg, Evelyn Regar, Patrick W. Serruys, K. Martijn Akkerhuis, and Eric Boersma. Near-infrared spectroscopy predicts cardiovascular outcome in patients with coronary artery disease. *Journal of the American College of Cardiology*, 64(23):2510–2518, 2014.

[31] Franz Josef Neumann, Miguel Sousa-Uva, Anders Ahlsson, Fernando Alfonso, Adrian P. Banning, Umberto Benedetto, Robert A. Byrne, Jean Philippe Collet, Volkmar Falk, Stuart J. Head, Peter Jüni, Adnan Kastrati, Akos Koller, Steen D. Kristensen, Josef Niebauer, Dimitrios J. Richter, Petar M. Seferovic, Dirk Sibbing, Giulio G. Stefanini, Stephan Windecker, Rashmi Yadav, and Michael O. Zembala. 2018 ESC/EACTS Guidelines on myocardial revascularization. *European Heart Journal*, 40(2):87–165, 2019.

[32] Glenn N. Levine, Eric R. Bates, James C. Blankenship, Steven R. Bailey, John A. Bittl, Bojan Cercek, Charles E. Chambers, Stephen G. Ellis, Robert A. Guyton, Steven M. Hollenberg, Umesh N. Khot, Richard A. Lange, Laura Mauri, Roxana Mehran, Issam D. Moussa, Debabrata Mukherjee, Brahmajee K. Nallamothu, Henry H. Ting, Alice K. Jacobs, Jeffrey L.

Anderson, Nancy Albert, Mark A. Creager, Steven M. Ettinger, Jonathan L. Halperin, Judith S. Hochman, Frederick G. Kushner, E. Magnus Ohman, William Stevenson, and Clyde W. Yancy. 2011 ACCF/AHA/SCAI guideline for percutaneous coronary intervention. *Journal of the American College of Cardiology*, 58(24):574–651, 2011.

[33] Paul Beard. *Biomedical photoacoustic imaging*. 2011.

[34] Sacha Noimark, Richard J. Colchester, Radhika K. Poduval, Efthymios Maneas, Erwin J. Alles, Tianrui Zhao, Edward Z. Zhang, Michael Ashworth, Elena Tsolaki, Adrian H. Chester, Najma Latif, Sergio Bertazzo, Anna L. David, Sebastien Ourselin, Paul C. Beard, Ivan P. Parkin, Ioannis Papakonstantinou, and Adrien E. Desjardins. Polydimethylsiloxane Composites for Optical Ultrasound Generation and Multimodality Imaging. *Advanced Functional Materials*, 28(9):1–16, 2018.

[35] Richard J. Colchester, Charles A. Mosse, Davinder S. Bhachu, Joseph C. Bear, Claire J. Carmalt, Ivan P. Parkin, Bradley E. Treeby, Ioannis Papakonstantinou, and Adrien E. Desjardins. Laser-generated ultrasound with optical fibres using functionalised carbon nanotube composite coatings. *Applied Physics Letters*, 104:173502, 2014.

[36] Richard J. Colchester, Callum Little, George Dwyer, Sacha Noimark, Erwin J. Alles, Edward Z. Zhang, Christopher D. Loder, Ivan P. Parkin, Ioannis Papakonstantinou, Paul C. Beard, Malcolm C. Finlay, Roby D. Rakhit, and Adrien E. Desjardins. All-Optical Rotational Ultrasound Imaging. *Scientific Reports*, 9(1):1–8, 2019.

[37] E. Aytac-Kipergil, E. J. Alles, H. C. Pauw, J. Karia, S. Noimark, and A. E. Desjardins. Versatile and scalable fabrication method for laser-generated focused ultrasound transducers. *Optics Letters*, 44(24):6005–6008, 2019.

[38] M. O'Donnell, Y. Hou, J. S. Kim, S. Ashkenazi, S. W. Huang, and L. J. Guo. Optoacoustic generation of high frequency sound for 3-D ultrasonic imaging in medicine. *European Physical Journal: Special Topics*, 153:53–58, 2008.

[39] Bao Yu Hsieh, Jinwook Kim, Jiadeng Zhu, Sibo Li, Xiangwu Zhang, and Xiaoning Jiang. A laser ultrasound transducer using carbon nanofibers-polydimethylsiloxane composite thin film. *Applied Physics Letters*, 106(2):021902, 2015.

[40] Sacha Noimark, Richard J. Colchester, Ben J. Blackburn, Edward Z. Zhang, Erwin J. Alles, Sebastien Ourselin, Paul C. Beard, Ioannis Papakonstantinou, Ivan P. Parkin, and Adrien E. Desjardins. Carbon-Nanotube–PDMS Composite Coatings on Optical Fibers for All-Optical Ultrasound Imaging. *Advanced Functional Materials*, 26(46):8390–8396, 2016.

[41] Erwin J. Alles, Jeongmin Heo, Sacha Noimark, Richard J. Colchester, Ivan P. Parkin, Hyoung Won Baac, and Adrien E. Desjardins. Acoustical characterisation of carbon nanotube-loaded polydimethylsiloxane used for optical ultrasound generation. In *IEEE International Ultrasonics Symposium, IUS*, pages 1–4, 2017.

[42] Radhika K. Poduval, Sacha Noimark, Richard J. Colchester, Thomas J. Macdonald, Ivan P. Parkin, Adrien E. Desjardins, and Ioannis Papakonstantinou. Optical fiber ultrasound transmitter with electrospun carbon nanotube-polymer composite. *Applied Physics Letters*, 110(22):223701, 2017.

[43] E. Biagi, S. Cerbai, L. Masotti, L. Belsito, A. Roncaglia, G. Masetti, and N. Speciale. MOMS technology for fully fiber optic ultrasonic probes: A proposal for virtual biopsy. In *Proceedings of IEEE Sensors*, pages 1156–1160, 2010.

[44] James A. Guggenheim, Jing Li, Thomas J. Allen, Richard J. Colchester, Sacha Noimark, Olumide Ogunlade, Ivan P. Parkin, Ioannis Papakonstantinou, Adrien E. Desjardins, Edward Z. Zhang, and Paul C. Beard. Ultrasen-

sitive plano-concave optical microresonators for ultrasound sensing. *Nature Photonics*, 11:714–719, 2017.

[45] Malcolm C. Finlay, Charles A. Mosse, Richard J. Colchester, Sacha Noimark, Edward Z. Zhang, Sebastien Ourselin, Paul C. Beard, Richard J. Schillin, Ivan P. Parkin, Ioannis Papakonstantinou, and Adrien E. Desjardins. Through-needle all-optical ultrasound imaging in vivo: A preclinical swine study. *Light: Science and Applications*, 6(12):17103–17107, 2017.

[46] Sunish J. Mathews, Callum Little, Christopher D. Loder, Roby D. Rakhit, Wenfeng Xia, Edward Z. Zhang, Paul C. Beard, Malcolm C. Finlay, and Adrien E. Desjardins. All-optical dual photoacoustic and optical coherence tomography intravascular probe. *Photoacoustics*, 11:65–70, 2018.

[47] Guangyao Li, Zhendong Guo, and Sung-Liang Chen. Miniature all-optical probe for large synthetic aperture photoacoustic-ultrasound imaging. *Optics Express*, 25(21):25023–25035, 2017.

[48] Erwin J. Alles, Richard J. Colchester, Sacha Noimark, Edward Z. Zhang, Paul C. Beard, Malcolm C. Finlay, and Adrien E. Desjardins. Radio-frequency ablation monitoring through real-time, video-rate all-optical ultrasound imaging. In *SPIE Proceedings Diagnostic and Therapeutic Applications of Light*, page 108550, 2019.

[49] Peter H Tomlins, Graham N Smith, Peter D Woolliams, Janarthanan Rasakanthan, and Kate Sugden. Femtosecond laser micro-inscription of optical coherence tomography resolution test artifacts. *Biomedical Optics Express*, 2(5):1319, 2011.

[50] Anant Agrawal, Chao-Wei Chen, Jigesh Baxi, Yu Chen, and T. Joshua Pfefer. Multilayer thin-film phantoms for axial contrast transfer function measurement in optical coherence tomography. *Biomedical Optics Express*, 4(7):1166, 2013.

[51] Anant Agrawal, T Joshua Pfefer, Naureen Gilani, and Rebekah a Drezek. Three-dimensional characterization of optical coherence tomography point spread functions with a nanoparticle-embedded phantom. *Optics letters*, 35(13):2269–2271, 2010.

[52] Anthony Fouad, T. Joshua Pfefer, Chao-Wei Chen, Wei Gong, Anant Agrawal, Peter H. Tomlins, Peter D. Woolliams, Rebekah A. Drezek, and Yu Chen. Variations in optical coherence tomography resolution and uniformity: a multi-system performance comparison. *Biomedical Optics Express*, 5(7):2066, 2014.

[53] Angelo Accardo, Marie Charline Blatché, Rémi Courson, Isabelle Loubinoux, Christophe Thibault, Laurent Malaquin, and Christophe Vieu. Multiphoton Direct Laser Writing and 3D Imaging of Polymeric Freestanding Architectures for Cell Colonization. *Small*, 13(27):1700621, 2017.

[54] Shuhui Wu, Jesper Serbin, and Min Gu. Two-photon polymerisation for three-dimensional micro-fabrication. *Journal of Photochemistry and Photobiology A: Chemistry*, 9(5):384–390, 2006.

[55] Maria Göppert-Mayer. Über Elementarakte mit zwei Quantensprüngen. *Annalen der Physik*, 51:605, 1931.

[56] Gregor Weisgrab, Olivier Guillaume, Zhengchao Guo, Patrick Heimel, Paul Slezak, André Poot, Dirk Grijpma, and Aleksandr Ovsianikov. 3D printing of large-scale and highly porous biodegradable tissue engineering scaffolds from poly(trimethylene-carbonate) using two-photon-polymerization. *Biofabrication*, 12(4):045036, 2020.

[57] Charles-Étienne Bisaillon, Marc L. Dufour, and Guy Lamouche. Artery phantoms for intravascular optical coherence tomography: healthy arteries. *Biomedical Optics Express*, 2(9):2599–2613, 2011.

[58] Brett E Bouma, Martin Villiger, Kenichiro Otsuka, and Wang-Yuhl OH. Intravascular optical coherence tomography [Invited]. *Biomedical Optics Express*, 8(5):2660–2686, 2017.

[59] Guy Lamouche, Brendan F. Kennedy, Kelsey M. Kennedy, Charles-Etienne Bisaillon, Andrea Curatolo, Gord Campbell, Valérie Pazos, and David D. Sampson. Review of tissue simulating phantoms with controllable optical, mechanical and structural properties for use in optical coherence tomography. *Biomedical Optics Express*, 3(6):1381–1398, 2012.

[60] Yan Li, Joseph Jing, Emon Heidari, Jiang Zhu, Yueqiao Qu, and Zhongping Chen. Intravascular Optical Coherence Tomography for Characterization of Atherosclerosis with a 1.7 Micron Swept-Source Laser. *Scientific Reports*, 7(1):2–7, 2017.

[61] Theodore Moffitt, Yin-Chu Chen, and Scott A. Prahl. Preparation and characterization of polyurethane optical phantoms. *Journal of Biomedical Optics*, 11(4):041103, 2006.

[62] Brendan F. Kennedy, Susanne Loitsch, Robert A. McLaughlin, Loretta Scolaro, Paul Rigby, and David D. Sampson. Fibrin phantom for use in optical coherence tomography. *Journal of Biomedical Optics*, 15(3):030507, 2010.

[63] Charles-Étienne Bisaillon, Marc L. Dufour, and Guy Lamouche. Artery phantoms for intravascular optical coherence tomography: healthy arteries. *Biomedical Optics Express*, 2(9):2599–2613, 2011.

[64] Charles Etienne Bisaillon, Guy Lamouche, Romain Maciejko, Marc Dufour, and Jean Pierre Monchalin. Deformable and durable phantoms with controlled density of scatterers. *Physics in Medicine and Biology*, 53(13):237–247, 2008.

[65] Brendan F. Kennedy, Timothy R. Hillman, Robert A. McLaughlin, Bryden C. Quirk, and David D. Sampson. In vivo dynamic optical coherence elastography using a ring actuator. *Optics Express*, 17(24):21762–21772, 2009.

[66] Andrea Curatolo, Brendan F. Kennedy, and David D. Sampson. Structured three-dimensional optical phantom for optical coherence tomography. *Optics Express*, 19(20):19480–19485, 2011.

[67] Charles-Étienne Bisaillon and Guy Lamouche. Artery phantoms for intravascular optical coherence tomography: diseased arteries. *Journal of Biomedical Optics*, 18(9):096010, 2013.

[68] Phuong Diep, Sanjana Pannem, Jordan Sweer, Justine Lo, Michael Snyder, Gabriella Stueber, Yanyu Zhao, Syeda Tabassum, Raeef Istfan, Junjie Wu, Shyamsunder Erramilli, and Darren Roblyer. Three-dimensional printed optical phantoms with customized absorption and scattering properties. *Biomedical Optics Express*, 6(11):4212–4220, 2015.

[69] Minjie Wang, Shuwei Shen, Jie Yang, Erbao Dong, and Ronald Xu. 3D printing method for freeform fabrication of optical phantoms simulating heterogeneous biological tissue. In *SPIE Procceedings Design and Performance Validation of Phantoms Used in Conjunction with Optical Measurement of Tissue*, page 894509, 2014.

[70] J. T. Dodge, B. G. Brown, E. L. Bolson, and H. T. Dodge. Lumen diameter of normal human coronary arteries: Influence of age, sex, anatomic variation, and left ventricular hypertrophy or dilation. *Circulation*, 86(1):232–246, 1992.

[71] Hiromasa Otake, Yoichiro Sugizaki, Takayoshi Toba, Yuichiro Nagano, Yoshiro Tsukiyama, Ken ichi Yanaka, Hiroyuki Yamamoto, Akira Nagasawa, Hiroyuki Onishi, Ryo Takeshige, Shinsuke Nakano, Yoichiro Matsuoka, Kosuke Tanimura, Hiroyuki Kawamori, Toshiro Shinke, and Ken ichi Hirata. Efficacy of alirocumab for reducing plaque vulnerability: Study protocol for ALTAIR, a randomized controlled trial in Japanese patients with coronary artery disease receiving rosuvastatin. *Journal of Cardiology*, 73(3):228–232, mar 2019.

[72] Daniel B. Fullager, Glenn D. Boreman, and Tino Hofmann. Infrared dielectric response of nanoscribe IP-dip and IP-L monomers after polymerization from 250 cm to 6000 cm. *Optical Materials Express*, 7(3):888, 2017.

[73] Timo Gissibl, Simon Thiele, Alois Herkommer, and Harald Giessen. Submicrometre accurate free-form optics by three-dimensional printing on single-mode fibres. *Nature Communications*, 7:11763, 2016.

[74] Jhonattan C. Ramirez, Juliana N. Schianti, Maria G. Almeida, Aristides Pavani, Roberto R. Panepucci, Hugo E. Hernandez-Figueroa, and Lucas H. Gabrielli. Low-loss modified SU-8 waveguides by direct laser writing at 405 nm. *Optical Materials Express*, 7(7):2651, 2017.

[75] Daniel M. de Bruin, Rolf H. Bremmer, Vitali M. Kodach, Roy de Kinkelder, Jan van Marle, Ton G. van Leeuwen, and Dirk J. Faber. Optical phantoms of varying geometry based on thin building blocks with controlled optical properties. *Journal of Biomedical Optics*, 15(2):025001, 2010.

[76] Richard Caulfield, Feihuang Fang, and Manish K. Tiwari. Drops, Jets and High-Resolution 3D Printing: Fundamentals and Applications. In *Droplet and Spray Tansport: Paradigms and Applications*, pages 123–162. 2018.

[77] Frank D. Gunstone. *Vegetable Oils in Food Technology: Composition, Properties and Uses, Second Edition*. 2011.

[78] Seán O'Halloran, Abhay Pandit, Andreas Heise, and Andrew Kellett. Two-Photon Polymerization: Fundamentals, Materials, and Chemical Modification Strategies. *Advanced Science*, 10(7):2204072, 2023.

[79] Roshni Solanki, Rebecca Gosling, Vignesh Rammohan, Giulia Pederzani, Pankaj Garg, James Heppenstall, D. Rodney Hose, Patricia V. Lawford, Andrew J. Narracott, John Fenner, Julian P. Gunn, and Paul D. Morris. The importance of three dimensional coronary artery reconstruction accuracy when computing virtual fractional flow reserve from invasive angiography. *Scientific Reports*, 4(11):19694, 2021.

[80] James Muller and Ryan Madder. OCT-NIRS Imaging for Detection of Coronary Plaque Structure and Vulnerability. *Frontiers in Cardiovascular Medicine*, 7, 2020.

[81] Ryan D. Madder, Mustafa Husaini, Alan T. Davis, Stacie Vanoosterhout, Mohsin Khan, David Wohns, Richard F. Mcnamara, Kevin Wolschleger, John Gribar, J. Stewart Collins, Mark Jacoby, Jeffrey M. Decker, Michael Hendricks, Stephen T. Sum, Sean Madden, James H. Ware, and James E. Muller. Large lipid-rich coronary plaques detected by near-infrared spectroscopy at non-stented sites in the target artery identify patients likely to experience future major adverse cardiovascular events. *European Heart Journal Cardiovascular Imaging*, 17(4):393–399, 2016.

[82] Kiyoshi Hibi, Kazuo Kimura, and Satoshi Umemura. Clinical utility and significance of intravascular ultrasound and optical coherence tomography in guiding percutaneous coronary interventions. *Circulation Journal*, 79(1):24–33, 2014.

[83] Evan Shlofmitz, Fernando A. Sosa, Ziad A. Ali, Ron Waksman, Allen Jeremias, and Richard Shlofmitz. OCT-Guided Treatment of Calcified Coronary Artery Disease: Breaking the Barrier to Stent Expansion. *Current Cardiovascular Imaging Reports*, 12(32), 2019.

[84] Timo Gissibl, Sebastian Wagner, Jachym Sykora, Michael Schmid, and Harald Giessen. Refractive index measurements of photo-resists for three-dimensional direct laser writing. *Optical Materials Express*, 7(7):2293, 2017.

[85] Giacomo Calzetti, Klemens Fondi, Ahmed M. Bata, Nikolaus Luft, Piotr A. Wozniak, Katarzyna J. Witkowska, Matthias Bolz, Alina Popa-Cherecheanu, René M. Werkmeister, Doreen Schmidl, Gerhard Garhöfer, and Leopold Schmetterer. Assessment of choroidal blood flow using laser speckle flowgraphy. *British Journal of Ophthalmology*, 102(12):1679–1683, 2018.

[86] Alec M. De Grand, Stephen J. Lomnes, Deborah S. Lee, Matthew Pietrzykowski, Shunsuke Ohnishi, Timothy G. Morgan, Andrew Gogbashian, Rita G. Laurence, and John V. Frangioni. Tissue-like phantoms for near-infrared fluorescence imaging system assessment and the training of surgeons. *Journal of Biomedical Optics*, 11(1):014007, 2006.

[87] Lingling Zhao, Vivian K. Lee, Seung Schik Yoo, Guohao Dai, and Xavier Intes. The integration of 3-D cell printing and mesoscopic fluorescence molecular tomography of vascular constructs within thick hydrogel scaffolds. *Biomaterials*, 332(21):5325–5332, 2012.

[88] Conor K. McGarry, Lesley J. Grattan, Aoife M. Ivory, Francesca Leek, Gary P. Liney, Yang Liu, Piero Miloro, Robba Rai, Andrew P. Robinson, Albert J. Shih, Bajram Zeqiri, and Catharine H. Clark. Tissue mimicking materials for imaging and therapy phantoms: A review. *Physics in Medicine and Biology*, 65:44, 2020.

[89] Anne L. Abbott, Christopher F. Bladin, Christopher R. Levi, and Brian R. Chambers. What should we do with asymptomatic carotid stenosis? *International Journal of Stroke*, 2(1):27–39, 2007.

[90] John J. Ricotta, Ali Aburahma, Enrico Ascher, Mark Eskandari, Peter Faries, and Brajesh K. Lal. Updated Society for Vascular Surgery guidelines for management of extracranial carotid disease: Executive summary. *Journal of Vascular Surgery*, 54(3):832–836, 2011.

[91] Ali F. Aburahma, Mohit Srivastava, Patrick A. Stone, Albeir Y. Mousa, Akhilesh Jain, L. Scott Dean, Tammi Keiffer, and Mary Emmett. Critical appraisal of the Carotid Duplex Consensus criteria in the diagnosis of carotid artery stenosis. *Journal of Vascular Surgery*, 53(1):53–60, 2011.

[92] Paul J. Nederkoorn, Yolanda Van Der Graaf, and M. G Myriam Hunink. Duplex ultrasound and magnetic resonance angiography compared with digi-

tal subtraction angiography in carotid artery stenosis: A systematic review. *Stroke*, 34(5):1324–1332, 2003.

[93] Mark J W Koelemay, Paul J. Nederkoorn, Johannes B. Reitsma, and Charles B. Majoie. Systematic review of computed tomographic angiography for assessment of carotid artery disease. *Stroke*, 35(10):2306–2312, 2004.

[94] J. Jacomelli, L. Summers, A. Stevenson, T. Lees, and J. J. Earnshaw. Impact of the first 5 years of a national abdominal aortic aneurysm screening programme. *The British journal of surgery*, 103(9):1125–1131, 2016.

[95] Anders Wanhainen, Fabio Verzini, Isabelle Van Herzeele, Eric Allaire, Matthew Bown, Tina Cohnert, Florian Dick, Joost van Herwaarden, Christos Karkos, Mark Koelemay, Tilo Kölbel, Ian Loftus, Kevin Mani, Germano Melissano, Janet Powell, Zoltán Szeberin, ESVS Guidelines Committee, Gert J. de Borst, Nabil Chakfe, Sebastian Debus, Rob Hinchliffe, Stavros Kakkos, Igor Koncar, Philippe Kolh, Jes S. Lindholt, Melina de Vega, Frank Vermassen, Document reviewers, Martin Björck, Stephen Cheng, Ronald Dalman, Lazar Davidovic, Konstantinos Donas, Jonothan Earnshaw, Hans Henning Eckstein, Jonathan Golledge, Stephan Haulon, Tara Mastracci, Ross Naylor, Jean Baptiste Ricco, and Hence Verhagen. European Society for Vascular Surgery (ESVS) 2019 Clinical Practice Guidelines on the Management of Abdominal Aorto-iliac Artery Aneurysms. *European Journal of Vascular and Endovascular Surgery*, 57(1):8–93, 2019.

[96] Fran Parkinson, Stuart Ferguson, Peter Lewis, Ian M. Williams, and Christopher P. Twine. Rupture rates of untreated large abdominal aortic aneurysms in patients unfit for elective repair. *Journal of Vascular Surgery*, 61(6):1606–1612, 2015.

[97] Jes S. Lindholt and Rikke Søgaard. Population screening and intervention for vascular disease in Danish men (VIVA): a randomised controlled trial. *The Lancet*, 390(10109):2218–2220, 2017.

[98] K. Hoshina, M. Kato, T. Miyahara, A. Mikuriya, N. Ohkubo, and T. Miyata. A retrospective study of intravascular ultrasound use in patients undergoing endovascular aneurysm repair: Its usefulness and a description of the procedure. *European Journal of Vascular and Endovascular Surgery*, 40(5):559–563, 2010.

[99] Thomas Leger, Vania Tacher, Marek Majewski, Joseph Touma, Pascal Desgranges, and Hicham Kobeiter. Image Fusion Guidance for In Situ Laser Fenestration of Aortic Stent graft for Endovascular Repair of Complex Aortic Aneurysm: Feasibility, Efficacy and Overall Functional Success. *Cardio-Vascular and Interventional Radiology*, 42(10):1371–1379, 2019.

[100] Tamie L. Poepping, Hristo N. Nikolov, Meghan L. Thorne, and David W. Holdsworth. A thin-walled carotid vessel phantom for Doppler ultrasound flow studies. *Ultrasound in Medicine Biology*, 30(8):1067–1078, aug 2004.

[101] Y F Law, K W Johnston, H F Routh, and R S C Cobbold. On the design and evaluation of a steady flow model for doppler ultrasound studies. *Ultrasound in Med. BioL*, 15(5):505–516, 1989.

[102] D W Rickey, P A Picot, D A Christopher, and A Fenster. A wall-less phantom for doppler ultrasound studies. *Science*, 5629:1163–1176, 1995.

[103] Xiaowei Zhou, David A Kenwright, Shiying Wang, John A Hossack, and Peter R Hoskins. Fabrication of Two Flow Phantoms for Doppler Ultrasound Imaging. *IEEE Transactions on Ultrasonics, Ferroelectrics and Frequency Control*, 64(1):53–65, 2017.

[104] Tamie L Poepping, Hristo N Nikolov, Richard N Rankin, Mark Lee, David W Holdsworth, and The P John. An in vitro system for doppler ultrasound flow

studies in the stenosed carotid artery bifurcation. *Ultrasound in Med Biol*, 28(4):495–506, 2002.

[105] Hareem Nisar, John Moore, Roberta Piazza, Efthymios Maneas, Elvis C.S. Chen, and Terry M. Peters. A simple, realistic walled phantom for intravascular and intracardiac applications. *International Journal of Computer Assisted Radiology and Surgery*, 15(9):1513–1523, 2020.

[106] Daniil I. Nikitichev, Anamaria Barburas, Kirstie McPherson, Jean Martial Mari, Simeon J. West, and Adrien E. Desjardins. Construction of 3-dimensional printed ultrasound phantoms with wall-less vessels. *Journal of Ultrasound in Medicine*, 35(6):1333–1339, 2016.

[107] Robert F. Smith, Brian K. Rutt, and David W. Holdsworth. Anthropomorphic carotid bifurcation phantom for MRI applications. *Journal of Magnetic Resonance Imaging*, 10(4):533–544, oct 1999.

[108] S Meagher, T L Poepping, K V Ramnarine, R A Black, and P R Hoskins. Anatomical flow phantoms of the nonplanar carotid bifurcation, part II Experimental validation with doppler ultrasound. *Ultrasound in Med Biol*, 33(2):303–310, 2007.

[109] D.M. Watts, C.J. Sutcliffe, R.H. Morgan, S. Meagher, J. Wardlaw, M. Connell, M.E. Bastin, I. Marshall, K.V. Ramnarine, P.R. Hoskins, and R.A. Black. Anatomical flow phantoms of the nonplanar carotid bifurcation, Part I: Computer-aided design and fabrication. *Ultrasound in Medicine Biology*, 33(2):296–302, feb 2007.

[110] Chung Kit Ho, Adrian J Y Chee, Graduate Student Member, Billy Y S Yiu, Anderson C O Tsang, Kwok Wing Chow, Alfred C H Yu, and Senior Member. Wall-Less Flow Phantoms With Tortuous Vascular Geometries : Design Principles and a Patient-Specific Model Fabrication Example. *IEEE Transactions on Ultrasonics, Ferroelectrics, and Frequency Control*, 64(1):25–38, 2017.

[111] Louise Allard, Gilles Soulez, Boris Chayer, Zhao Qin, David Roy, and Guy Cloutier. A multimodality vascular imaging phantom of an abdominal aortic aneurysm with a visible thrombus. *Medical Physics*, 40(6):063701, 2013.

[112] Giacomo Annio, Gaia Franzetti, Mirko Bonfanti, Antonio Gallarello, Andrea Palombi, Elena De Momi, Shervanthi Homer-Vanniasinkam, Helge A. Wurdemann, Victor Tsang, Vanessa Diáz-Zuccarini, Ryo Torii, Stavroula Balabani, and Gaetano Burriesci. Low-Cost Fabrication of Polyvinyl Alcohol-Based Personalized Vascular Phantoms for In Vitro Hemodynamic Studies: Three Applications. *Journal of Engineering and Science in Medical Diagnostics and Therapy*, 3(3):034501, 2020.

[113] Eleanor C. Mackle, Efthymios Maneas, Callum Little, Elizabeth Carr, Wenfeng Xia, Daniil Nikitichev, Roby Rakhit, Malcolm Finlay, and Adrien Desjardins. Wall-less vascular poly(vinyl) alcohol gel ultrasound imaging phantoms using 3D printed vessels. In *SPIE Procceedings Design and Quality for Biomedical Optics*, page 108700, 2019.

[114] Peter R. Hoskins. Simulation and Validation of Arterial Ultrasound Imaging and Blood Flow. *Ultrasound in Medicine and Biology*, 34(5):693–717, 2008.

[115] Peter M. Brown, David T. Zelt, Boris Sobolev, John W. Hallett, and Yaron Sternbach. The risk of rupture in untreated aneurysms: The impact of size, gender, and expansion rate. *Journal of Vascular Surgery*, 37(2):280–284, 2003.

[116] Young Hoon Kim. Ultrasound phantoms to protect patients from novices. *Korean Journal of Pain*, 29(2):73–77, 2016.

[117] Ernest L. Madsen, Maritza A. Hobson, Hairong Shi, Tomy Varghese, and Gary R. Frank. Tissue-mimicking agar/gelatin materials for use in heterogeneous elastography phantoms. *Physics in Medicine and Biology*, 50(23):5597–5618, 2005.

[118] Wenfeng Xia, Daniele Piras, Michelle Heijblom, Wiendelt Steenbergen, Ton G. van Leeuwen, and Srirang Manohar. Poly(vinyl alcohol) gels as photoacoustic breast phantoms revisited. *Journal of Biomedical Optics*, 16(7):075002, 2011.

[119] Deirdre M. King, Carmel M. Moran, John D. McNamara, Andrew J. Fagan, and Jacinta E. Browne. Development of a Vessel-Mimicking Material for use in Anatomically Realistic Doppler Flow Phantoms. *Ultrasound in Medicine and Biology*, 37(5):813–826, 2011.

[120] Efthymios Maneas, Wenfeng Xia, Daniil I. Nikitichev, Batol Daher, Maniragav Manimaran, Rui Yen J. Wong, Chia Wei Chang, Benyamin Rahmani, Claudio Capelli, Silvia Schievano, Gaetano Burriesci, Sebastien Ourselin, Anna L. David, Malcolm C. Finlay, Simeon J. West, Tom Vercauteren, and Adrien E. Desjardins. Anatomically realistic ultrasound phantoms using gel wax with 3D printed moulds. *Physics in Medicine and Biology*, 63(1):015033, 2018.

[121] Efthymios Maneas, Wenfeng Xia, Olumide Ogunlade, Martina Fonseca, Daniil I. Nikitichev, Anna L. David, Simeon J. West, Sebastien Ourselin, Jeremy C. Hebden, Tom Vercauteren, and Adrien E. Desjardins. Gel wax-based tissue-mimicking phantoms for multispectral photoacoustic imaging. *Biomedical Optics Express*, 9(3):1151–1163, 2018.

[122] Elliot L. Chaikof, Ronald L. Dalman, Mark K. Eskandari, Benjamin M. Jackson, W. Anthony Lee, M. Ashraf Mansour, Tara M. Mastracci, Matthew Mell, M. Hassan Murad, Louis L. Nguyen, Gustavo S. Oderich, Madhukar S. Patel, Marc L. Schermerhorn, and Benjamin W. Starnes. The Society for Vascular Surgery practice guidelines on the care of patients with an abdominal aortic aneurysm. *Journal of Vascular Surgery*, 67(1):2–77, 2018.

[123] Benjamin Dean and Erlick Pereira. Surgeons and training time. *British Medical Journal*, 343:6724, 2011.

[124] I. O. Torres and N. De Luccia. A simulator for training in endovascular aneurysm repair: The use of three dimensional printers. *European Journal of Vascular and Endovascular Surgery*, 54(2):247–253, 2017.

[125] Vincenzo Vento, Laura Cercenelli, Chiara Mascoli, Enrico Gallitto, Stefano Ancetti, Gianluca Faggioli, Antonio Freyrie, Emanuela Marcelli, Mauro Gargiulo, and Andrea Stella. The Role of Simulation in Boosting the Learning Curve in EVAR Procedures. *Journal of Surgical Education*, 75(2):534–540, 2018.

[126] Jeffrey Bortman, Faraz Mahmood, Marc Schermerhorn, Ruby Lo, Nicholas Swerdlow, Feroze Mahmood, and Robina Matyal. Use of 3-Dimensional Printing to Create Patient-Specific Abdominal Aortic Aneurysm Models for Preoperative Planning. *Journal of Cardiothoracic and Vascular Anesthesia*, 33(5):1442–1446, 2019.

[127] Jasamine Coles-Black and Jason Chuen. 3D Printed AAA Phantoms for Presurgical Evar Simulation- A Single Center Experience. *European Journal of Vascular and Endovascular Surgery*, 91(9):1673–1681., 2019.

[128] A. Saratzis, T. Calderbank, D. Sidloff, M. J. Bown, and R. S. Davies. Role of Simulation in Endovascular Aneurysm Repair (EVAR) Training: A Preliminary Study. *European Journal of Vascular and Endovascular Surgery*, 53(2):193–198, 2017.

[129] Jussi M. Kärkkäinen, Giuliano Sandri, Emanuel R. Tenorio, Amy Alexander, Karen Bjellum, Jane Matsumoto, Jonathan Morris, Bernardo C. Mendes, Randall R. DeMartino, and Gustavo S. Oderich. Simulation of Endovascular Aortic Repair Using 3D Printed Abdominal Aortic Aneurysm Model and Fluid Pump. *CardioVascular and Interventional Radiology*, 42(11):1627–1634, 2019.

[130] Karen M. Meess, Richard L. Izzo, Maciej L. Dryjski, Richard E. Curl, Linda M. Harris, Michael Springer, Adnan H. Siddiqui, Stephen Rudin, and

Ciprian N. Ionita. 3D printed abdominal aortic aneurysm phantom for image guided surgical planning with a patient specific fenestrated endovascular graft system. In *Medical Imaging 2017: Imaging Informatics for Healthcare, Research, and Applications*, page 10138, 2017.

[131] A. M. Sailer, M. W. De Haan, A. G. Peppelenbosch, M. J. Jacobs, J. E. Wildberger, and G. W.H. Schurink. CTA with fluoroscopy image fusion guidance in endovascular complex aortic aneurysm repair. *European Journal of Vascular and Endovascular Surgery*, 47(4):349–356, 2014.

[132] Peter Kan, Maxim Mokin, Adib A. Abla, Jorge L. Eller, Travis M. Dumont, Elad I. Levy, and Adnan H. Siddiqui. Utility of intravascular ultrasound in intracranial and extracranial neurointerventions: experience at University at Buffalo Neurosurgery-Millard Fillmore Gates Circle Hospital. *Neurosurgical focus*, 32(1):6, 2012.

[133] Giulio Illuminati, Maria Antonietta Pacilè, Gianluca Ceccanei, Massimo Ruggeri, Giuseppe La Torre, and Jean Baptiste Ricco. Peroperative Intravascular Ultrasound for Endovascular Aneurysm Repair versus Peroperative Angiography: A Pilot Study in Fit Patients with Favorable Anatomy. In *Annals of Vascular Surgery*, 2020.

[134] Alfredo Conti, Antonio Pontoriero, Giuseppe Iatì, Daniele Marino, Domenico La Torre, Sergio Vinci, Antonino Germanò, Stefano Pergolizzi, and Francesco Tomasello. 3D-Printing of Arteriovenous Malformations for Radiosurgical Treatment: Pushing Anatomy Understanding to Real Boundaries. *Cureus*, 8(4):594, 2016.

[135] Callum D. Little, Richard J. Colchester, Sacha Noimark, Gavin Manmathan, Malcolm C. Finlay, Adrien E. Desjardins, and Roby D. Rakhit. Optically Generated Ultrasound for Intracoronary Imaging. *Frontiers in Cardiovascular Medicine*, 7:525530, 2020.

[136] Richard J. Colchester, Erwin J. Alles, George Dwyer, Efthymios Maneas, Danail Stoyanov, and Adrien E. Desjardins. Large area all-optical ultrasound imaging using robotic control. *Opto-Acoustic Methods and Applications in Biophotonics Proceedings*, 110771, 2019.

[137] Callum Little, Richard J. Colchester, Gavin Manmathan, Roby D. Rakhit, and Adrien E. Desjardins. All-optical ultrasound: A new polatform for intracoronary imaging. *Journal of the American College of Cardiology*, 75:1348, 2020.

[138] Ye Tian, Nan Wu, Xiaotian Zou, Haitham Felemban, Chengyu Cao, and Xingwei Wang. Fiber-optic ultrasound generator using periodic gold nanopores fabricated by a focused ion beam. *Optical Engineering*, 52(6):065005, 2013.

[139] Hyoung Won Baac, Jong G. Ok, Adam Maxwell, Kyu Tae Lee, Yu Chih Chen, A. John Hart, Zhen Xu, Euisik Yoon, and L. Jay Guo. Carbon-nanotube optoacoustic lens for focused ultrasound generation and high-precision targeted therapy. *Scientific Reports*, 2:989, 2012.

[140] Charles A. Mosse, Richard J. Colchester, Davinder S. Bhachu, Edward Z. Zhang, Ioannis Papakonstantinou, and Adrien E. Desjardins. Fiber optic ultrasound transducers with carbon/PDMS composite coatings. In *Proceedings of SPIE Photons Plus Ultrasound: Imaging and Sensing*, page 89430, 2014.

[141] Takashi Buma, Monica Spisar, and Matthew O'Donnell. A high-frequency, 2-D array element using thermoelastic expansion in PDMS. *IEEE Transactions on Ultrasonics, Ferroelectrics, and Frequency Control*, 50(9):1161–1176, 2003.

[142] Richard J. Colchester, Edward Z. Zhang, Charles A. Mosse, Paul C. Beard, Ioannis Papakonstantinou, and Adrien E. Desjardins. Broadband miniature optical ultrasound probe for high resolution vascular tissue imaging. *Biomedical Optics Express*, 6(4):1502–1511, 2015.

[143] Teruyoshi Kume, Hiroyuki Okura, Takahiro Kawamoto, Ryotaro Yamada, Yoshinori Miyamoto, Akihiro Hayashida, Nozomi Watanabe, Yoji Neishi, Yoshito Sadahira, Takashi Akasaka, and Kiyoshi Yoshida. Assessment of the coronary calcification by optical coherence tomography. *EuroIntervention*, 6(6):768–772, 2011.

[144] Krishnaraj S. Rathod, Stephen M. Hamshere, Daniel A. Jones, and Anthony Mathur. Intravascular Ultrasound Versus Optical Coherence Tomography for Coronary Artery Imaging - Apples and Oranges? *Interventional Cardiology Review*, 10(1):8–15, 2015.

[145] Marcos Garcia-Guimaraes, Paula Antuña, Francisco De la Cuerda, Ramón Maruri-Sanchez, Javier Cuesta, Teresa Bastante, Fernando Rivero, and Fernando Alfonso. High-Definition IVUS Versus OCT to Assess Coronary Artery Disease and Results of Stent Implantation. *JACC: Cardiovascular Imaging*, 13(2):519–521, 2020.

[146] Srirang Manohar, Reń G.H. Willemink, Ferdi Van Der Heijden, Cornelis H. Slump, and Ton G. Van Leeuwen. Concomitant speed-of-sound tomography in photoacoustic imaging. *Applied Physics Letters*, 91:131911, 2007.

[147] Jithin Jose, Rene G. H. Willemink, Steffen Resink, Daniele Piras, J. C. G van Hespen, Cornelis H. Slump, Wiendelt Steenbergen, Ton G. van Leeuwen, and Srirang Manohar. Passive element enriched photoacoustic computed tomography (PER PACT) for simultaneous imaging of acoustic propagation properties and light absorption. *Optics Express*, 19(3):2093–2104, 2011.

[148] X. Luís Deán-Ben, Vasilis Ntziachristos, and Daniel Razansky. Artefact reduction in optoacoustic tomographic imaging by estimating the distribution of acoustic scatterers. *Journal of Biomedical Optics*, 17(11):110504, 2012.

[149] Tianrui Zhao, Lei Su, and Wenfeng Xia. Optical ultrasound generation and detection for intravascular imaging: A review. *Journal of Healthcare Engineering*, 30(2018):3182483, 2018.

[150] Erwin J. Alles, Sacha Noimark, Efthymios Maneas, Edward Z. Zhang, Ivan P. Parkin, Paul C. Beard, and Adrien E. Desjardins. Video-rate all-optical ultrasound imaging. *Biomedical Optics Express*, 9(8):3481–3494, 2018.

[151] Andres Schanzer and Gustavo S. Oderich. Management of Abdominal Aortic Aneurysms. *New England Journal of Medicine*, 385(18):1690–1698, 2021.

[152] Uchechukwu K.A. Sampson, Paul E. Norman, F. Gerald R. Fowkes, Victor Aboyans, Yanna Song, Frank E. Harrell, Mohammad H. Forouzanfar, Mohsen Naghavi, Julie O. Denenberg, Mary M. McDermott, Michael H. Criqui, George A. Mensah, Majid Ezzati, and Christopher Murray. Estimation of global and regional incidence and prevalence of abdominal aortic aneurysms 1990 to 2010. *Global Heart*, 9(1):159–170, 2014.

[153] Sourabh Aggarwal, Arman Qamar, Vishal Sharma, and Alka Sharma. Abdominal aortic aneurysm: A comprehensive review. *Experimental and Clinical Cardiology*, 16(1):11–15, 2011.

[154] Abdominal aortic aneurysm: diagnosis and management [NG156], 2020.

[155] Monique Prinssen, Eric L.G. Verhoeven, Jaap Buth, Philippe W.M. Cuypers, Marc R.H.M. van Sambeek, Ron Balm, Erik Buskens, Diederick E. Grobbee, and Jan D. Blankensteijn. A Randomized Trial Comparing Conventional and Endovascular Repair of Abdominal Aortic Aneurysms. *New England Journal of Medicine*, 351(16):1607–1618, 2004.

[156] G P Greenhalgh, R M. Brown, L C. Kwong. Comparison of endovascular aneurysm repair with open repair in patients with abdominal aortic aneurysm (EVAR trial 1), 30-day operative mortality results: Randomised controlled trial. *Lancet*, 364(9437):843–848, 2004.

[157] Vincent Jongkind, Kak K. Yeung, George J.M. Akkersdijk, David Heidsieck, Johannes B. Reitsma, Geert Jan Tangelder, and Willem Wisselink. Juxtarenal aortic aneurysm repair. *Journal of Vascular Surgery*, 52(3):760–767, 2010.

[158] Prateek K. Gupta, Reshma Brahmbhatt, Kelly Kempe, Shaun M. Stickley, and Michael J. Rohrer. Thirty-day outcomes after fenestrated endovascular repair are superior to open repair of abdominal aortic aneurysms involving visceral vessels. *Journal of Vascular Surgery*, 66(6):1653–1658, 2017.

[159] Catharina Helena Jacoba Berghmans, Thomas Lübke, and Jan Sigge Brunkwall. A Cost Calculation of EVAR and FEVAR Procedures at an European Academic Hospital. *Annals of Vascular Surgery*, 2019.

[160] L. A. Eadie, G. Soulez, M. W. King, and L. W. Tse. Graft durability and fatigue after in situ fenestration of endovascular stent grafts using radiofrequency puncture and balloon dilatation. *European Journal of Vascular and Endovascular Surgery*, 47(5):501–508, 2014.

[161] Richard G. McWilliams, Micheal Murphy, David Hartley, Michael Lawrence-Brown, and Peter L. Harris. In Situ Stent-Graft Fenestration to Preserve the Left Subclavian Artery. *Journal of Endovascular Therapy*, 11(2):170–174, 2004.

[162] Tao Shang, Lu Tian, Dong lin Li, Zi heng Wu, and Hong kun Zhang. Favourable Outcomes of Endovascular Total Aortic Arch Repair Via Needle Based In Situ Fenestration at a Mean Follow-Up of 5.4 Months. *European Journal of Vascular and Endovascular Surgery*, 55(4):369–376, 2018.

[163] Yilang Xiang, Chenyang Qiu, Yangyan He, Donglin Li, Tao Shang, Ziheng Wu, and Hongkun Zhang. A Single Center Experience of In Situ Needle Fenestration of Supra-aortic Branches During Thoracic Endovascular Aortic Repair. *Annals of Vascular Surgery*, 61:107–115, 2019.

[164] Leonard W.H. Tse, Bao T. Bui, Sophie Lerouge, Igor Salazkin, Eric Therasse, Andrew Benko, Hélène Héon, Vincent L. Oliva, and Gilles Soulez. In vivo antegrade fenestration of abdominal aortic stent-grafts. *Journal of Endovascular Therapy*, 14(2):158–167, 2007.

[165] Kyle W. Eudailey, Gregory Von Mering, Paxton Johanson, James English, Clifton T. Lewis, and Mustafa I. Ahmed. Total Endovascular Arch Repair Using Needle Fenestration and Extracorporeal Membrane Oxygenation. *Annals of Thoracic Surgery*, 109(2):127–129, 2020.

[166] Sean A. Crawford, Ryan M. Sanford, Thomas L. Forbes, Cristina H. Amon, and Matthew G. Doyle. Clinical outcomes and material properties of in situ fenestration of endovascular stent grafts. *Journal of Vascular Surgery*, 64(1):244–250, 2016.

[167] Celia V. Riga, Colin D. Bicknell, Melvinder Basra, Mohamad Hamady, and Nicholas J.W. Cheshire. In vitro fenestration of aortic stent-grafts: Implications of puncture methods for in situ fenestration durability. *Journal of Endovascular Therapy*, 20(4):536–543, 2013.

[168] Furuzan Numan, Harun Arbatli, Walter Bruszewski, and Mustafa Cikirikcioglu. Total endovascular aortic arch reconstruction via fenestration in situ with cerebral circulatory support: An acute experimental study. *Interactive Cardiovascular and Thoracic Surgery*, 7(4):535–538, 2008.

[169] Leonard W. Tse, Thomas F. Lindsay, Graham Roche-Nagle, George D. Oreopoulos, Maral Ouzounian, and Kong Teng Tan. Radiofrequency in situ fenestration for aortic arch vessels during thoracic endovascular repair. *Journal of Endovascular Therapy*, 22(1):116–121, 2015.

[170] Thomas Le Houérou, Dominique Fabre, Carlos G. Alonso, Philippe Brenot, Ryiad Bourkaib, Claude Angel, Myriam Amsallem, and Stephan Haulon. In Situ Antegrade Laser Fenestrations During Endovascular Aortic Repair. *European Journal of Vascular and Endovascular Surgery*, 56(3):356–362, 2018.

[171] Julia L. Sandell and Timothy C. Zhu. A review of in-vivo optical properties of human tissues and its impact on PDT. *Journal of Biophotonics*, 4(11):773–787, 2011.

[172] Sara Condino, Roberta Piazza, Filippo Micheletti, Francesca Rossi, Roberto Pini, Raffaella Berchiolli, Aldo Alberti, Vincenzo Ferrari, and Mauro Ferrari. Electromagnetic guided in-situ laser fenestration of endovascular stent-graft: Endovascular tools sensorization strategy and preliminary laser testing. In *Medical Imaging and Augmented Reality*, page 9805, 2016.

[173] Roberta Piazza, Filippo Micheletti, Sara Condino, Giada Magni, Raffaella N. Berchiolli, Paolo De Simone, Vincenzo Ferrari, Mauro Ferrari, Roberto Pini, and Francesca Rossi. In situ diode laser fenestration: An ex-vivo evaluation of irradiation effects on human aortic tissue. *Journal of Biophotonics*, 12(9), 2019.

[174] Benjamin J. Pearce and William D. Jordan. Using IVUS during EVAR and TEVAR: Improving Patient Outcomes. *Seminars in Vascular Surgery*, 22(3):172–180, 2009.

[175] Stefano Gennai, Nicola Leone, Giuseppe Saitta, Mattia Migliari, Antonio Lauricella, Luca Farchioni, and Roberto Silingardi. Intravascular Ultrasound in Branched and Fenestrated Endovascular Aneurysm Repair: Initial Experience in a Single-Center Cohort Study. *Journal of Endovascular Therapy*, 28(6):828–836, 2021.

[176] Marco V. Usai, Alexander Oberhuber, and Giuseppe Asciutto. Assessment of Bridging Stent Grafts in Branched Endovascular Aortic Repair (EVAR) Procedures Using Intravascular Ultrasound (IVUS). *EJVES Vascular Forum*, 47, 2020.

[177] Erwin J. Alles, Sacha Noimark, Edward Zhang, Paul C. Beard, and Adrien E. Desjardins. Pencil beam all-optical ultrasound imaging. *Biomedical Optics Express*, 7(9):3693–3704, 2016.

[178] Geert Luyckx, Eli Voet, Nicolas Lammens, and Joris Degrieck. Strain measurements of composite laminates with embedded fibre bragg gratings: Criticism and opportunities for research. *Sensors*, 11(1):384–408, 2011.

[179] Yun Jiang Rao, Zeng Ling Ran, and Yuan Gong. *Fiber-optic fabry-perot sensors: An introduction*. 2017.

[180] Joanna Coote, Sandy Mosse, Sacha Noimark, Erwin Alles, Callum Little, Chris D. Loder, Roby D. Rakhit, Malcolm C. Finlay, and Adrien E. Desjardins. Fibre-optic pressure and temperature measurements using phase-resolved low-coherence interferometry. In *Optical Fibers and Sensors for Medical Diagnostics and Treatment Applications*, page 104880, 2018.

[181] Joseph Edwards, Hossam Abdou, Neerav Patel, Marta J. Madurska, Kelly Poe, Janet E. Bonin, Michael J. Richmond, Todd E. Rasmussen, and Jonathan J. Morrison. The functional vascular anatomy of the swine for research. *Vascular*, 30(2):392–402, 2022.

[182] Raimund Erbel and Holger Eggebrecht. Aortic dimensions and the risk of dissection. *Heart*, 97:137–142, 2006.

[183] Muhammad Faraz, Muhammad Awais Abbasi, Pilgyu Sang, Donghee Son, and Hyoung Won Baac. Stretchable and robust candle-soot nanoparticle-polydimethylsiloxane composite films for laser-ultrasound transmitters. *Micromachines*, 11(17):631, 2020.

[184] Kara Peters. Polymer optical fiber sensors - A review. *Smart Materials and Structures*, 20:013002, 2011.

[185] Ginu Rajan and Krzysztof Kris Iniewski. *Optical fiber sensors: Advanced techniques and applications*. 2017.

[186] Jing Lin, Naval Udgiri, Robert Guidoin, Jean Panneton, Xiaoning Guan, Maxime Guillemette, Lu Wang, Jia Du, Dajie Zhu, Mark Nutley, and Ze Zhang. In Vitro Laser Fenestration of Aortic Stent-Grafts: A Qualitative Analysis Under Scanning Electron Microscope. *Artificial Organs*, 40(11):241–252, 2016.

[187] Francesco Fulvio Faletra, Giovanni Pedrazzini, Elena Pasotti, Iveta Petrova, Agne Drasutiene, Maria Cristina Dequarti, Stefano Muzzarelli, and Tiziano Moccetti. Role of real-time three dimensional transoesophageal echocardiography as guidance imaging modality during catheter based edge-to-edge mitral valve repair. *Heart*, 99(16):1205–1215, 2013.

[188] Jonathan Yap, Jason H. Rogers, Edris Aman, Thomas W.R. Smith, and Gagan D. Singh. MitraClip Implantation Guided by Volumetric Intracardiac Echocardiography: Technique and Feasibility in Patients Intolerant to Transesophageal Echocardiography. *Cardiovascular Revascularization Medicine*, 28:85–88, 2021.

[189] Sunish J. Mathews, Dzhoshkun I. Shakir, Charles A. Mosse, Wenfeng Xia, Edward Z. Zhang, Paul C. Beard, Simeon J. West, Anna L. David, Sebastien Ourselin, Tom Vercauteren, and Adrien Desjardins. Ultrasonic Needle Tracking with Dynamic Electronic Focusing. *Ultrasound in Medicine and Biology*, 48(3):520–529, 2022.

[190] O'Neill R Waton S, Johal A, Birmpili P, Li W, Cromwell D, Boyle J, Pherwani A. National Vascular 2020 Annual Report. Technical Report 1, 2020.